# AN ABSTRACT OF THE THESIS OF

Shane R. Hawke for the degree of Master of Science in Mechanical Engineering

presented on December 12, 2006.

Title: Effects of a Thin, Flexible Nozzle on Droplet Formation and Impingement

Abstract approved:

_____

James A. Liburdy

The droplet formation process in the vicinity of the nozzle exit and the behavior of a spreading droplet during impingement on a smooth glass surface were studied. Two nozzle geometries were tested. The first case was a stiff stainless steel nozzle plate 0.787 mm thick. The second case was a flexible stainless steel nozzle plate 0.102 mm thick. In each case, two different waveforms were used to drive the piezoelectric element in the droplet generator. This resulted in different meniscus behavior at the nozzle exit in each case. Leading and trailing edge velocities and the position of the leading edge relative to the nozzle were measured through use of double-frame images taken with a high-speed camera to describe the formation process at the nozzle. This data was displayed in both dimensional and non-dimensional form using capillary parameters. At the impingement surface, the high speed camera was used to record the spread rate and contact angle of the droplets. This research concluded that the flexible nozzle had a significant impact on droplet formation. Exit velocities were more than double those of the stiff nozzle, and break-off times were shorter for the flexible nozzle. One drawback of the flexible nozzle

was that satellite droplets were produced along with the main droplet, which did not happen with a stiff nozzle. Behavior at the impingement surface was also noted to be different in each case. However, this is not directly related to the different nozzles themselves, but rather the fact that the nozzles resulted in different droplet velocities. The spread rate of the droplets was observed to increase as the impingement velocity was increased. The dynamic contact angles were also measured and compared to existing models found in the literature. Although there were discrepancies, it is likely that these are due to the difference in Weber numbers between this experiment and the models.

©Copyright by Shane R. Hawke
December 12, 2006
All Rights Reserved

# Effects of a Thin, Flexible Nozzle on Droplet Formation and Impingement

by
Shane R. Hawke

A THESIS

submitted to

Oregon State University

in partial fulfillment of
the requirement for the
degree of

Master of Science

Presented December 12, 2006
Commencement June 2007

Master of Science thesis of Shane R. Hawke presented on December 12, 2006.

APPROVED:

_____

Major Professor, representing Mechanical Engineering

_____

Head of the Department of Mechanical Engineering

_____

Dean of the Graduate School

I understand that my thesis will become part of the permanent collection of Oregon State University libraries. My signature below authorizes release of my thesis to any reader upon request.

_____

Shane R. Hawke, Author

# ACKNOWLEDGEMENTS

The author would like to acknowledge his advisor, Dr. James Liburdy, for his guidance and support throughout the duration of this research project. The author would also like to thank Dr. Deborah Pence, Dr. Vinod Narayanan, and Dr. Brian Woods for serving on his graduate committee. Finally, the author would like to thank Jian Shen for her assistance with the experimental portion of this project, and Saangrut Sangplung for his work on the numerical simulations.

# TABLE OF CONTENTS

TABLE OF CONTENTS (Continued)

# LIST OF FIGURES

# LIST OF FIGURES (Continued)

# LIST OF FIGURES (Continued)

# LIST OF TABLES

# LIST OF APPENDICES

# LIST OF APPENDIX FIGURES

# LIST OF APPENDIX TABLES

# NOMENCLATURE

| | | | |
|---|---|---|---|
| b | brass disk displacement | $t_b$ | break-off time |
| $C_f$, $C_i$ | pixel-to-meter conversion coefficients | $t_c$ | capillary time |
| Ca | capillary number, $\frac{\mu U}{\sigma}$ | u | uncertainty value |
| d | distance from nozzle | U | droplet spread rate |
| D | variable waveform time delay | v | droplet velocity |
| $D_{av}$ | average drop diameter | $v_c$ | capillary velocity |
| $D_c$ | characteristic length | V | volume |
| $d_{nozzle}$ | nozzle diameter | $V_{av}$ | average drop volume |
| $D_o$ | impingement diameter | $V_e$ | maximum exit velocity |
| $D_r$ | plate rigidity | $V_o$ | impingement velocity |
| E | bulk modulus | $V_{pp}$ | peak-to-peak voltage |
| h | plate thickness | w | deflection of a flat plate |
| Oh | Ohnesorge number, $\frac{\mu}{\sqrt{\rho\sigma D}}$ | W | deflection at plate center |
| P | fluid chamber pressure | We | Weber number, $\frac{\rho U^2 D}{\sigma}$ |
| P1,P2 | pixel locations | *Greek Symbols* | |
| r | radial coordinate | $\theta_c$ | dynamic contact angle |
| R | plate radius | $\theta_o$ | static contact angle |
| $R^2$ | chi square value | μ | viscosity |
| Re | Reynolds number, $\frac{\rho UD}{\mu}$ | ν | Poisson ratio |
| t | time | σ | surface tension |

# EFFECTS OF A THIN, FLEXIBLE NOZZLE ON DROPLET FORMATION AND IMPINGEMENT

## 1. INTRODUCTION

The focus of this research project is to determine how different operating conditions affect the droplet formation process and the subsequent impingement process. This section establishes why this knowledge is important and then details the objectives that this project needs to achieve.

### *1.1 Background*

Droplet formation is used in a wide range of engineering applications. In the inkjet printing process, piezoelectric deformations or thermally driven bubbles are used to produce pressure changes that eject small ink droplets out of an array of nozzles onto a piece of paper. A similar process is used in three-dimensional printing applications, such as a rapid prototyper, where small droplets of wax or a photopolymer can be deposited in layers to create 3-dimensional parts. Droplet formation also plays an important role in spray cooling, where a spray of droplets is directed onto a hot surface to remove heat. These droplet sprays also play an important role in combustion, where fuel droplets are sprayed into a combustion chamber. Finally, microdroplets are being used in medical applications to dispense extremely small volumes of liquid (on the order of nanoliters) quickly and precisely.

All of these applications have similar requirements. It is important that the droplets land predictably at their intended destination. This is especially significant when considering inkjet printing and three-dimensional printing, both of which require

precise placement of droplets for quality results. The behavior of the droplet once it impacts on a surface must also be considered. Depending on the droplet velocity at the point of impact, different behaviors such as splashing or fingering can be observed. The spread rate of the drop will also be affected by the velocity at the point of impact, which can be an important consideration in spray cooling environments.

In addition to droplet behavior at the point of impact, droplet behavior at the point of origin must also be considered. For example, the formation of satellite droplets, small droplets that break-off from the main droplet, can have a significant impact in certain applications. The presence of these satellite droplets depends on fluid properties, nozzle geometry, and the droplet velocity. If conditions exist such that satellite droplets are present, then the result can be a blurry image printed on a piece of paper as the satellite droplets fall to either side of the main droplet, or it can cause an inaccurate amount of fluid to be dispensed from a micropipette.

To control this droplet behavior, the user has the option of varying the fluid properties, droplet generator geometry, and operating conditions. Therefore, it is important to know what effect these variables have on droplet behavior both at the nozzle and at an impingement surface.

## *1.2 Objectives*

The goal of this research is to experimentally investigate the behavior of droplets during the droplet formation process, from the time the droplet leaves the nozzle to when it impacts on a smooth flat surface. In addition to experimentally determining how different parameters affect the droplet formation process, the results

of this experiment will also be used to validate a numerical model currently being developed. To accomplish this goal, there are several objectives that must be met.

The first of these objectives is to create a droplet generator that is able to produce droplets on demand. This droplet generator should also be easily adjustable in order to change parameters of interest, such as the flexibility of the nozzle plate, the size of the nozzle opening, or the volume of the fluid chamber.

The second objective is to study the droplet formation process in the vicinity of the nozzle opening. A high-speed camera capturing two images 0.5 ms apart is used to study this. Two different nozzle plates are used during this phase of the project – a stiff plate and a thinner, more flexible plate. The differences in droplet formation between the two cases are compared using the velocity and position data for the leading and trailing edges of the droplets captured by the camera.

The final objective is to study the behavior of droplets as they impact on a smooth glass surface. A high-speed camera is used to observe the impingement process and calculate the spread rate of the droplets at various stages during this process. Additionally, the dynamic contact angle is calculated at various points. These results are then compared to the existing dynamic contact angle models available in the literature.

# 2. LITERATURE REVIEW

Droplets are used in a wide variety of applications, from inkjet printing to spray cooling. There are two methods of producing droplets – either by the breakup of a liquid jet, or through the use of a droplet-on-demand droplet generator. Regardless of the application, there are two specific periods in the life of the droplet that are particularly important to understand. These two periods are the time when the droplet forms, and the time during which the droplet impacts the surface, whether it is a piece of paper or a heated component. Understanding the behavior at both points in the droplet process is necessary to predict the physical characteristics of the droplet and to achieve the desired affect once the droplet reaches its target.

## *2.1 Droplet Formation*

Understanding the behavior of a droplet as it is created is important for several reasons. First, it can provide insight into how a droplet generating device should be designed. The geometry of the fluid chamber, properties of the fluid, the geometry and physical properties of the nozzle, and the method with which pressure pulses are created will all have effects on the droplet behavior as it is ejected. It is also important to understand how the droplet velocity at the nozzle exit will affect the path and behavior of the droplet. For example, if the velocity reaches a critical point, then satellite droplets will break off from the main droplet. Understanding how these variables affect the behavior of the droplet, and how they can be manipulated to suit the purposes of the application of interest, has been the subject of extensive study.

### *2.1.1 Primary Droplet Formation*

The primary droplet is the largest drop that is ejected from the nozzle or that is produced by the breakup of a liquid jet. In most cases, it is the only drop to be produced. But under certain conditions smaller satellite droplets also form, and it becomes necessary to distinguish between the two types. It is important to be able to accurately predict the shape, velocity, and path of the primary droplet as it is produced in order to deliver a specific volume of fluid to a desired location. This behavior has been the subject of numerous experimental and numerical studies.

In Lee's analytical study [1] on drop formation in a liquid jet, he performs a one-dimensional analysis using the continuity equation and a momentum balance. Through this analysis, Lee was able to predict the optimal conditions for droplet formation, as well as predict the breakup time for the droplets, given the initial conditions of the system. The analysis involved two parameters that affected droplet behavior – a wave length parameter H, and a surface tension-disturbance parameter Q. Lee would later expand this study to focus specifically on satellite droplet behavior and the ideal conditions for preventing their formation. [2]

In order to look at a droplet-on-demand type system as opposed to a liquid jet, Zhang [3] performed a numerical analysis using the volume of fluid approach. Specifically, he looked at the behavior of a single drop breaking off from the end of a capillary tube. The numerical model was able to predict the shape of both the droplet and the liquid thread. These results were then verified with experimental observations of 2-ethyl-1-hexanol droplets ejected into water – a liquid-liquid system. Effects due

to the Reynolds number, gravitational Bond number, viscosity ratios, and other parameters were then analyzed using this numerical model.

In order to examine how different time scales affect drop formation, Wilkes and Basaran [4] created a finite element model (FEM) of a droplet suspended at the end of an oscillating rod. Different forcing amplitudes, forcing frequencies, and fluid properties were examined while using the FEM code to predict the response of the droplet. It was found that the behavior of the droplet as it breaks off from the oscillating rod is dependent on several different time scales interacting with each other.

In an experimental study involving time scales conducted by Meacham *et al.* [5], an ultrasonic droplet generator was used to observe droplet formation in both the droplet-on-demand and liquid jetting cases. A scaling analysis was then performed, which resulted in relating the transition from jetting to droplets-on-demand to several different time scales, as well as a critical Weber number and Strouhal number.

Another experimental study was carried out by Shield *et al.* [6] in order to validate the results from a numerical model of a droplet-on-demand ink-jet nozzle. The nozzle consisted of a glass tube with a piezoelectric element attached to the sides. Both water and ethylene glycol were used as working fluids. It was found that a single primary drop was formed at the fundamental and first harmonic pulse lengths, while an intermediate pulse length resulted in the formation of several smaller droplets. Satellites would be formed in the case of overdriving. It was also found that both water and ethylene glycol behaved similarly, even though the two fluids have different viscosities.

### *2.1.2 Satellite Droplet Formation*

Satellite droplets are typically small in size compared to the primary droplet. They are formed when the liquid thread breaks and the primary droplet is created. Under certain conditions, which are dependent on fluid properties and the droplet velocity, the breaking of the thin liquid thread is not a clean break. The thread breaks up into several smaller droplets instead of retracting back into the fluid reservoir or the rest of the liquid jet. These satellite droplets typically veer off the path of the primary drop and collide with the target surface in areas other than the intended destination. For certain applications, such as inkjet printing and rapid prototyping, this can have a negative impact on the quality of the final product. Therefore, it is necessary to understand the conditions under which these satellite droplets occur.

In a follow-up article to his study on drop formation in liquid jets, Lee and Pimbley [2] examined satellite droplet formation under the same conditions. A second order nonlinear analysis of the behavior was done using a spatial instability, rather than a temporal instability. The results of this analysis gave an accurate description of the satellite behavior in general, but the inclusion of higher order terms would be necessary to achieve quantitative results. The corresponding experimental work resulted in a "satellite condition map", which relates the behavior of satellite droplets to the parameter $\lambda/d$, which is the distance between successive droplets divided by the diameter of a droplet. It was found that a distance between droplets of 5 to 6.5 droplet diameters was optimal for preventing satellite droplet formation in a liquid jet.

Mutoh [7] looked further into the different kinds of satellite behavior observed by Pimbley and Lee, such as forward-merging and rear-merging satellites. This study

observed charged droplets. By measuring the phase curve of the liquid jet (a plot of the current of the liquid jet $I_j(\theta)$ vs. the phase $\theta$) with a phase search pulse, Mutoh was able to relate these phase curves to the behavior of the liquid threads that are formed as a liquid jet breaks up into droplets. The behavior of the satellite droplets can then be predicted based on these phase curve measurements.

In a study looking at droplet ejection from a tapered glass capillary tube due to the longitudinal vibration of a piezoelectric actuator, Lee and Lal [8] looked at the effects of the tip velocity on the formation of satellite droplets. The tip velocity is defined as the leading edge velocity at the capillary tube exit, and depends on the actuation voltage supplied to the piezoelectric element. It was found that on a plot of actuation voltage vs. tip velocity, there was only a small band where droplets could form without producing satellites. If the actuation voltage was increased past this range, the resulting increase in fluid ejected from the nozzle resulted in an average-sized droplet and a satellite, not in one larger droplet. A critical velocity was also observed beyond which multiple satellite droplets were produced. But if the tip velocity was controlled, then it was possible to eliminate the presence of satellites.

In a numerical study carried out by Ambravaneswaran, Wilkes and Basaran [9], a comparison was made between 1-D and 2-D drop formation models and their ability to predict satellite droplet formation. The 1-D model used a slender jet approximation to simplify the 2-D model. The results of the study indicate that the 1-D model is in agreement with the 2-D model when the Weber number (We), the ratio of inertial to surface tension forces, is small and when the Ohnesorge number (Oh), the ratio of viscous to surface tension forces, is small to moderate. When either of

these two parameters increase, then the 1-D results begin to veer away from the 2-D predictions. For cases with low We and Oh numbers, it was found that the 1-D model resulted in computational times one to two orders of magnitude smaller than the 2-D model. The 1-D model was then used to predict the formation of satellite droplets. The results indicate that for a given Ohnesorge number, which depends on the fluid properties and nozzle geometry, there is a critical Weber number that describes satellite droplets. Weber number values above this critical number will result in no satellites, while values below the critical value will always produced satellite droplets.

### *2.1.3 Effects of a Flexible Nozzle*

The physical properties of the nozzle on a droplet-on-demand droplet generator will have an effect on the formation of a droplet. The Young's modulus of the nozzle material will determine how easily a material will deform when subjected to a pressure pulse. The physical geometry of the nozzle, thickness, surface area, and clamping condition will also determine how much a particular nozzle deflects during the droplet formation process. Even the operating frequency of the droplet generator will have an effect on nozzle deflection. How this deflection of a flexible nozzle impacts the shape and path of a droplet during the formation process must be understood in order to ensure accurate placement of droplets.

Percin and Khuri-Yakub [10] have designed a device that produces droplets solely due to the vibration of a flexible membrane that rests on a nozzle plate. As the plate moves, the pressure in the fluid reservoir increases. This pressure can increase up to 15 atm above atmospheric. When the pressure is increased for a sufficient

period of time, then droplets can overcome surface tension and are ejected from the nozzle. This vibrating nozzle set-up was able to produce droplets repeatedly and uniformly, as experimental results in the study demonstrated.

Percin *et al.* [11] also examined a different kind of droplet generator that uses a flexible nozzle plate. The difference with this second set-up is that the piezoelectric element forms the bottom of the fluid chamber opposite the nozzle plate – the piezoelectric does not directly cause the nozzle plate to flex. The goal of this droplet generator is to dispense picoliters and femtoliters of fluid. Experimental trials proved that this design could produce droplets from a 4 micron diameter orifice at a frequency of 3.45 MHz. This droplet generator design could be scaled down to fit as many as 20,000 nozzle orifices in one square centimeter.

Yang and Liburdy [12] developed a numerical model to compare droplet formation using a stiff nozzle to several different flexible nozzle cases (with varying Young's modulus). It was found that a vibrating nozzle resulted in greater droplet velocities than the stiff nozzle case. However, the effects on droplet size and break-off time were much less noticeable. The numerical simulations also indicate that a flexible nozzle will cause an increased number of satellite droplets to form, while the satellite velocity will be affected by the nozzle vibrations.

## *2.2 Droplet Impingement*

The second point in the droplet process that is of interest to many applications is when the droplet collides with a surface. There are many different conditions that a droplet can encounter at an impingement surface. The surface can be smooth or

rough, and either heated, cooled, or at the same temperature as the drop. Sometimes there may already be standing liquid drops on the surface. And if the frequency at which droplets are being generated is high enough, it is possible that a droplet could impact a surface while the droplet before it is still spreading – this is known as successive droplet impingement. All of these different scenarios have been the focus of previous studies.

### *2.2.1 Impingement of a Single Droplet on a Flat Surface*

The simplest droplet impingement scenario is a single droplet colliding with a horizontal surface. This surface could be a piece of paper going through a printer, a heated metal surface that is being spray cooled, or a layer of material in a rapid prototyping machine. But regardless of the surface, there are certain parameters that are important to investigate. The spread rate of the droplet can have a significant effect on heat transfer rates in cooling applications. The impact velocity of the droplet, combined with fluid properties, can determine whether or not splashing or fingering effects occur. Several studies have been conducted to investigate this behavior.

Bechtel *et al.* [13] created a numerical model to investigate the behavior of droplets in ink-jet printing applications. This model used a Lagrangian approach with a truncated sphere model of the droplet hitting a flat surface. The behavior of the droplet was dependent on three different parameters – the Weber number, the ratio of surface tensions, and a viscosity parameter. The numerical results from this model agreed with the experimental results available at the time.

More recently, Park *et al.* [14] developed a numerical model to look at droplet spreading after impingement. Unlike most models that assume a cylindrical disk as the shape for the spreading droplet, this model assumes a spherical cap. This model was specifically designed for low impact velocities (less than 1 m/s), and was found to provide better predictions at these low velocities than cylindrical disk models when compared to experimental data. However, even at high impact velocities (greater than 1 m/s), the numerical results were within 10% of what was observed experimentally.

Fedorchenko and Wang [15] have created a mathematical model for analyzing droplet spreading behavior after impinging on a flat surface. They found that the maximum drop spread is influenced by the advancing contact angle of the droplet, as well as determining a parameter for which viscous effects can be neglected. The results of the mathematical model showed good agreement with experimental data.

Kamnis and Gu [16] created a numerical model that has been used to study the impingement of molten metal droplets, specifically molten tin droplets onto a stainless steel substrate. This is a two-dimensional model that takes solidification, heat transfer, and the case of air entrapment during impingement, all into account. The simulations were compared to experimental data of a 2.1 mm diameter tin droplet at 510K impinging on a steel surface at 4 m/s, and showed good agreement.

In addition to these numerical analyses, there have been many different experimental studies on droplet impingement. Sikalo, *et al.* [17] conducted a study of a single droplet impinging on a flat surface. The fluid was varied between water, isopropanol, and glycerin, while four different impinging surfaces were also used.

This allowed for a range of viscosities, surface tensions, and impinging surface roughnesses to be examined. It was discovered that the maximum spread of a droplet increased with increasing Weber and Reynolds numbers. It was also found that although the contact angle had an effect on the droplet spread at low Reynolds numbers, this effect diminished as the droplet impact velocity was increased. Splash conditions were also related to a critical Weber number, which was found to decrease as surface tension decreases.

Moita and Moreira [18] conducted a study focusing on how surface roughness affects droplet impingement. Typically, the behavior of droplets can be described by non-dimensional numbers such as Reynolds and Weber numbers. However, in this study it was concluded that a rough surface would cause a shift to smaller non-dimensional parameters that would describe the same behavior as impingement on a smooth surface. The standard ranges of non-dimensional parameters cannot be used when surface roughness is significantly increased.

Sivakumar *et al*. [19] performed another study on how surface roughness affects droplet spreading behavior after impingement. In this study, impingement on a smooth steel surface was compared to impingement on a textured substrate. It was found that on the textured substrate, two different kinds of spreading occurred simultaneously. Jet spreading occurred within the grooves of the substrate, while lamella spreading occurred above the textured grooves. For high Weber numbers, jet spreading dominates while lamella spreading dominates for low Weber numbers. It was also observed that while splashing can occur on textured substrates, the splashing

exhibits different characteristics from the fingering behavior that is observed when a droplet impinges on a smooth surface.

Fingering is a phenomenon that sometimes occurs in droplet impingement. Fingers are a series of waves on the edge of the spreading drop that form as the droplet spreads out after impact, and can sometimes be the precursor to splashing effects. Mehdizadeh *et al.* [20] completed an experimental study to analyze this fingering effect. The droplet size, velocity, and impinging surface roughness were varied during this study. It was found that fingering increased as both velocity and droplet size increased. If the velocity became high enough, the ends of the fingers would actually break off, forming small satellite droplets. It was also found that by increasing the surface roughness, fingering effects could be lessened.

Thoroddsen & Sakakibara [21] performed a study focusing on the shape of the fingers during droplet spreading. The study first looked at the spread rate of the droplets, then moved on to focus on the behavior of the fingers, such as when one finger would split into two smaller fingers, or when several finger would merge together. The results indicate that surface tension is the driving force behind the behavior of the fingers. It was also discovered that capillary waves had a strong effect on the phase velocity of the fingers.

Another type of behavior that can be observed during droplet impingement is splatter. When splatter occurs, small volumes of fluid break off from the primary drop after impact and land at other points on the impinging surface. This is rarely desirable, and in the case of ink-jet printing splatter can severely reduce print quality. Zable [22] examined this behavior as it applies to ink-jet printing. In the study, the drop size,

drop velocity, spacing between drop impacts, and time between drop impacts was varied. The impingement surface was a piece of paper, to mimic ink-jet printing conditions. It was observed that the spacing between drop impacts was the most important factor in the occurrence of splatter, followed by droplet size and impact velocity. Based on the experimental observations, a design relationship was formulated that would predict whether a reasonable amount of splatter, as determined by design requirements, will occur for a given set of conditions.

Amada *et al.* [23] performed a similar study, only this study was concerned with the splat profile of molten metal droplets. The experiment analyzed how different impinging velocities, Weber numbers, and Reynolds numbers affected the splat profile for a wide range of molten metals. An unevenness ratio (defined as the contour length of the spreading droplet divided by the circumference of a standard circle with an equivalent area) was introduced to describe the splat profile, which increased with impinging velocity. A relationship was also obtained experimentally between the unevenness ratio and the Weber and Reynolds numbers. These relationships were bilinear lines, with the corner being the critical point at which splashing begins to occur. This point varied depending on the type of metal being used, but critical Reynolds numbers ranged from $1.85 \times 10^4$ to $3.97 \times 10^4$, while critical Weber numbers ranged from 219 to 764.

### *2.2.2 Single Droplet Colliding with a Static Droplet*

In this scenario, a droplet ejected from a droplet generator collides directly with a hemispherical droplet that is at rest on a flat surface. This is typically an

intermediate step between studying droplet impingement on a flat surface and the impingement of two droplets in succession.

Fujimoto *et al.* [24] did both an experimental and numerical study of this scenario. The premise was that a droplet has hit a flat surface and after a sufficient period of time, achieves steady-state. After this long period of time, a second drop impinges on top of the first drop. Both drops had equal volumes of fluid. Experimentally, droplet collisions were recorded over a range of impact velocities. Both direct impacts and off-center impacts were studied. These same scenarios were then investigated numerically, with good agreement between the two sets of results.

### *2.2.3 Impingement of Successive Droplets on a Flat Surface*

When a droplet generator is operating at high frequencies, the droplets can be ejected in rapid succession so that one droplet impacts a surface before the previously ejected droplet has finished spreading. The interaction between the two droplets can result in some complicated flow behavior, which has been the subject of several experimental studies.

Fujimoto *et al.* published a series of two papers, [25] and [26], on the successive impingement of droplets onto a substrate. The first was a numerical study [25] using the volume-of-fluid approach to track the free surfaces. The results of the study were both free surface shapes and flow fields for a range of conditions, including different impact velocities of the trailing droplet, and whether the successive impacts were in phase (while the first droplet is still spreading), or out of phase (while the first droplet is receding inwards). The model predicted that the maximum spread

of the droplet increased as the trailing droplet velocity was increased. The spread also was larger for in phase impingements instead of out of phase impingements. These numerical results agreed with the experimental data, which was the subject of the second paper.

The experimental study conducted by Fujimoto *et al.* [26] looked at the successive impingement of two droplets both on a flat surface at room temperature, and on a heated flat surface (both 300 $^{o}$C and 500 $^{o}$C). At room temperature, the results matched up with what was predicted in the numerical simulation, with a clear liquid crown being observed as a result of the successive impacts. When looking at the heated surface impingements, it was found that this liquid crown was distorted, or in some cases disappeared altogether. This change in behavior is due to the boiling that takes place as the drop approaches a hot surface.

# 3. THEORY

Theoretical equations are an important component of any research project. Even if no numerical modeling is involved, equations can aid in understanding the basic physics of the problem at hand, and can help identify the parameters that will have the greatest influence over the observed results.

For this research, which is comparing a stiff nozzle to a flexible nozzle, it is important to look at the plate deflection equation. This equation predicts how much a plate of specified properties will deflect for a given pressure. This scenario is illustrated in Figure 3.1.

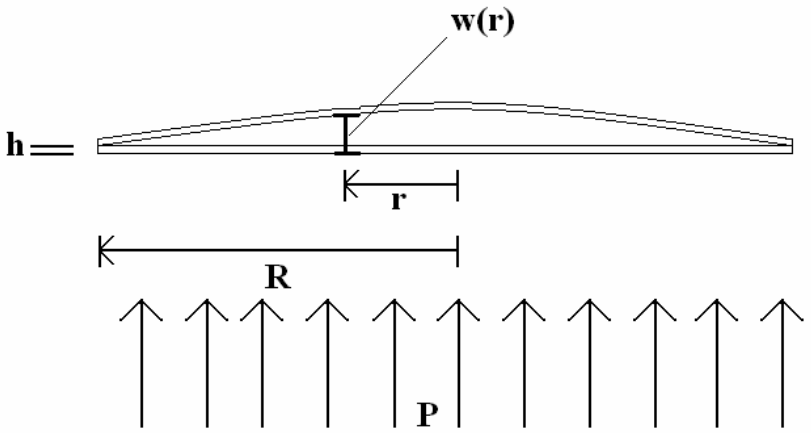


Figure 3.1
Plate deflection diagram

The plate deflection equation is given as Eq. (1) [27].

$$w(r) = \frac{1}{64}\frac{P}{D_r}R^4\left(1-\left(\frac{r}{R}\right)^2\right)^2 \qquad (1)$$

This equation is valid for small plate deflections, where the deflection is small in comparison to the plate thickness. In this equation, w(r) is the deflection upwards from the rest position at a distance r from the center. P is the pressure inside the fluid chamber, R is the radius of the nozzle plate, and $D_r$ is the plate rigidity. Plate rigidity is a function of the nozzle material properties, and is defined as

$$D_r = \frac{Eh^3}{12\left(1-\upsilon^2\right)} \tag{2}$$

where E is the Young's modulus, h is the thickness of the nozzle plate, and $\upsilon$ is the Poisson ratio.

When comparing a stiff nozzle to a flexible nozzle in this project, it is not necessary to know the plate deflection at every single point along the plate surface. The shape of the deflected plate is not of interest, only how much one plate deflects in comparison to another. This comparison can be made if the deflection is calculated for the same location in each of the two nozzle cases. If this point is selected to be the very center of the plate, then the radius at the deflection point is r = 0. Therefore, the equation reduces to

$$W = \frac{1}{64}\frac{P}{D_r}R^4 \tag{3}$$

where W is now the deflection at the center of the nozzle plate. Substituting the plate rigidity equation into the plate deflection gives the following result.

$$W = \frac{3}{16}\frac{PR^4\left(1-\upsilon^2\right)}{Eh^3} \tag{4}$$

This makes it easy to see the most important factors in determining plate deflection. The nozzle plate dimensions, radius and thickness, are raised to the fourth and third

powers, respectively. On the other hand, the Young's modulus E is only raised to the first power. Clearly, the dimensions of the nozzle plate play a much bigger role in determining plate deflection than the material properties.

In the case of this research project, the method of changing plate deflection was to change the thickness h of the nozzle plate. Given the design of the droplet generator, it would not have been feasible to change the radius R. To predict an actual plate deflection, it is necessary to know the pressure P inside the fluid reservoir. The current set-up does not measure this pressure. An attempt can be made to estimate this pressure by using the equation for the bulk modulus of a material,

$$E = \frac{\frac{dp}{dV}}{\frac{V}{}} \approx \frac{\frac{\Delta P}{\Delta V}}{V} \tag{5}$$

where ΔP would be the pressure to be inserted into the plate deflection equation. Rearranging this equation to solve for ΔP results in

$$\Delta P = E \frac{\Delta V}{V} \tag{6}$$

E, the bulk modulus of water, is a known quantity. The total volume of the fluid chamber in the droplet generator is also know, as well as the change in volume ΔV that occurs when the brass disk is pulsed forward, since the brass disk displacement has been characterized.

Unfortunately, there are too many unknowns in the test set-up to make an accurate pressure prediction. Fluid will be pushed out through the nozzle exit as well as back through the refill port, which will decrease the overall pressure inside the fluid chamber. Also, the geometry inside the fluid chamber is complex when there is a

nylon insert in place to reduce the overall volume of the fluid chamber. This means that in order to get a pressure estimate that would be useful for the plate deflection equation, it would either have to be measured directly or predicted using a numerical model. An estimate of this pressure is given in the next section once the droplet generator geometry is defined, but the confidence in the results is low due to the previously stated reasons.

Therefore, for this particular experiment, what the plate deflection equation reduces down to, in essence, is

$$W \sim \frac{1}{h^3} \tag{7}$$

The two nozzle plates used in this experiment had thicknesses of 0.102 mm (flexible) and 0.787 mm (stiff). So Eq. (7) predicts that the flexible nozzle plate should deflect 465 times as much as the stiff plate under similar operating conditions. The precise amount of deflection will need to be determined once the numerical model that is currently being developed is working and validated.

# 4. EXPERIMENTAL FACILITIES

The experimental set-up for this study consists of a droplet generator that can produce droplets of variable sizes and at different velocities. The design of this droplet generator is described in detail. The remainder of this section is devoted to describing the rest of the equipment used in this study, such as the mount for the droplet generator and impinging surface, as well as the imaging system used to take pictures of the droplets.

## *4.1 Droplet Generator Design*

The droplet generator used for this study was designed so that various aspects of the geometry could be altered with a minimal amount of time and effort. The body of the device is a steel cylinder which forms a small fluid reservoir that can be continuously refilled from a larger reservoir of fluid via plastic tubing that connects to a small refill port in the side of the droplet generator. A brass disk with a piezoelectric element bonded to the outside forms the bottom wall of the reservoir, while a steel nozzle plate is on top to complete the enclosure. Both the volume of the reservoir inside the droplet generator and the nozzle diameter can be varied, as will be explained later. Although several modifications have been made, the basic concept for this device was found in a journal article by Yang, *et al.* [28]. The technical drawings for the droplet generator used in this study were drawn in Solidworks, and are provided in Appendix A.

The body of the droplet generator is made from ANSI 304 steel. It is a hollow cylinder with an inner diameter of 15.875 mm, as seen in Figure 4.1. A refill port was drilled through the side of the body and allows fluid to flow from a large beaker to refill the reservoir as droplets are ejected, which allows the generator to produce droplets for extended periods of time if necessary. There is a needle valve located just outside the refill port that can be partially closed, which serves to increase the flow resistance through the refill port, ensuring that the fluid displaced by the brass disk is forced out through the nozzle and not back up into the refill reservoir.

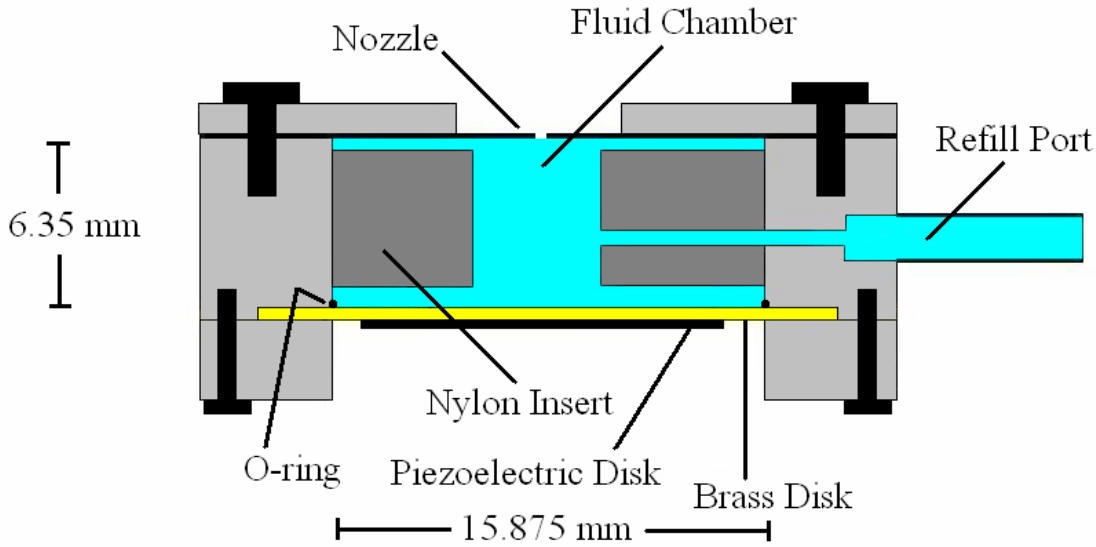


Figure 4.1
Droplet generator diagram

The volume of the fluid chamber can be changed by securing a nylon insert inside the chamber. This cylindrical insert significantly decreases the volume of the fluid reservoir, although room must be left at both the top and bottom of the chamber so that the brass disk and flexible nozzle can deflect without interference. Three different inserts were created for this study, with inner chamber diameters of 6.35 mm,

3.175 mm, and 1 mm. The result of decreasing the reservoir volume is an increased pressure pulse, given a constant brass disk displacement between the two scenarios. With a nylon insert in the reservoir, droplets can be produced at much higher frequencies (6 Hz instead of 1 Hz) than if the standard 15.875 mm diameter chamber was used since it takes less time to refill the fluid chamber.

The bottom of the fluid reservoir is formed by the brass disk, with an O-ring between this disk and the steel body to ensure a tight seal, seen in Figure 4.1. The disk used for this droplet generator is the APC352428A unimorph disk bender produced by American Piezo Ceramics, Inc. It consists of a brass disk with a piezoelectric element bonded to one side, as shown in Figure 4.2.

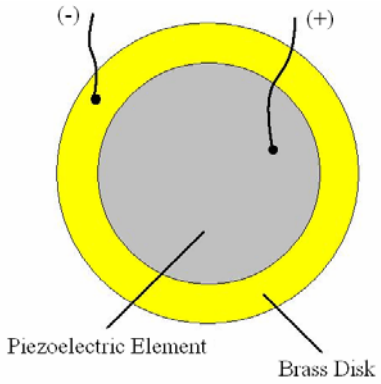


Figure 4.2
Piezoelectric element bonded to brass disk

Wires were soldered to the disk, one wire to the brass disk and the other to the piezoelectric element, which allowed the piezoelectric element to then be driven by a function generator. This brass disk was held in place between the steel body of the reservoir and a bottom cap that was bolted into the main body.

The final component of the droplet generator is the nozzle plate. The nozzle plates were constructed out of 0.787 mm and 0.102 mm thick ANSI 304 stainless steel (elastic modulus of 193 GPa). Three different plates were constructed with different nozzle diameters, listed in Table 4.1.

Table 4.1
Nozzle Dimensions

| *Plate Designation* | *Nozzle Diameter (mm)* |
|---|---|
| A | 1.25 |
| B | 1.00 |
| C | 0.40 |

The nozzle plate was held in place between the main body of the generator and a top cap that was bolted to this main body, as seen in Figure 4.1. Switching nozzle plates was a simple matter of unbolting the top cap and making the switch. This top cap also determines the flexibility of the nozzle plate. For the purposes of this experiment, the 6.35 mm diameter hole in the top cap remained constant.

With the droplet generator dimensions and materials specified, it is now possible to complete the analysis started in Section 3 to predict the deflection of the nozzle plate. With the droplet generator dimensions used in this study, the reservoir volume is $2.48 \times 10^{-7}$ $m^3$. When the brass disk is at maximum displacement, it creates a volume change of approximately $1.75 \times 10^{-9}$ $m^3$. Therefore, with water having a bulk modulus of 2.15 GPa, Eq. 6 predicts $\Delta P$ to be $1.513 \times 10^{7}$ Pa. This value can then be substituted into Eq. 4 as P. Using the geometries specified in this section, and

with the steel properties E = 193 GPa and ν = 0.29, the equation predicts that the center of the stiff nozzle plate will deflect 0.11 mm. For the flexible nozzle case, it predicts that the center of the nozzle plate will deflect 51 mm. Clearly these results are unrealistic. The massive over-prediction occurs because Eq. 6 assumes a sealed fluid chamber. In reality, most of the pressure force is used to push fluid out through the nozzle opening or back through the refill port, not to deflect the nozzle plate. In addition, the nylon insert that reduces the fluid chamber volume is likely influencing the pressure wave as it travels through the fluid chamber prior to interacting with the nozzle plate. So while this calculation did not result in valid deflection predictions, it does emphasize how the flow resistance at the nozzle opening and refill ports, along with the design of the fluid chamber geometry, can influence the pressure inside the fluid chamber, and therefore the deflection of a thin nozzle plate. Fortunately, this experiment can still proceed without knowing the exact deflection of the flexible plate. The analysis in Section 3 showed that the 0.102 mm thick plate will deflect much more than the stiff case, so general "flexible vs. stiff" comparisons can be made. The exact amount of deflection can be determined later using a numerical model.

## *4.2 Experimental Set-Up*

The experimental set-up for this research is pictured in Figure 4.3.

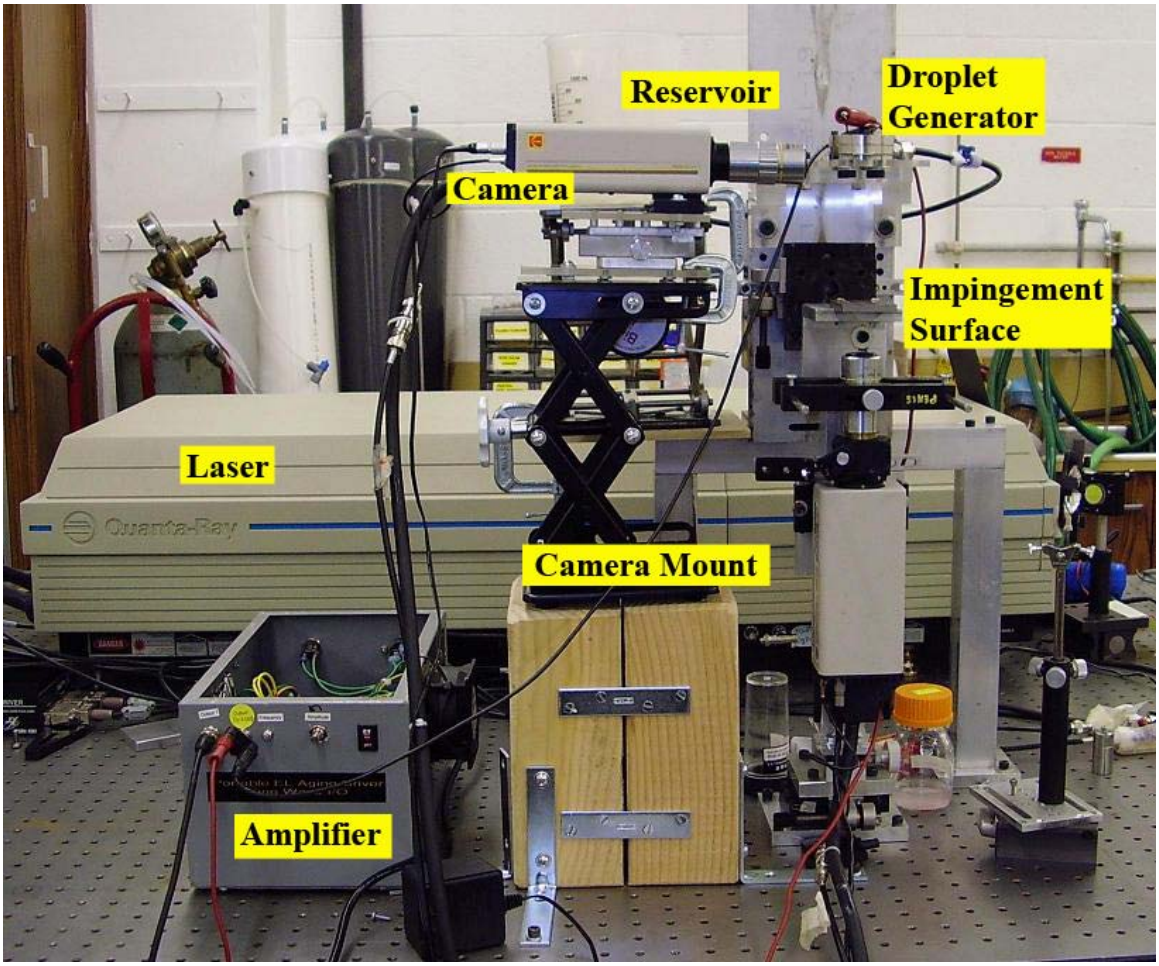


Figure 4.3
Experimental set-up

The droplet generator described in the previous section is mounted on a stand on the right-hand side of the photograph. It is mounted directly to a translation stage that allows for fine adjustments to be made in the vertical, or z-, direction. The droplet generator is supplied fluid by a reservoir that is mounted on a scissor jack, seen in the photograph behind the camera. Directly below the droplet generator is a metal stand

that serves to support the glass slides that are used when looking at droplet impingement. This impingement surface is mounted to another translation stage so that it can be adjusted independent of the droplet generator.

The behavior of the droplet generator is controlled by a collection of waveforms programmed into a Sony Tektronix AWG2021 Arbitrary Waveform Generator (not pictured). This waveform generator runs through the Portable EL Aging Driver Sine Wave I/O amplifier seen in Figure 4.3, and then to the piezoelectric element in the droplet generator.

The fluid that is supplying the droplet generator is distilled water which contains a Rhodamine 6G Chloride fluorescent dye at a molar concentration of $1x10^{-5}$. This rhodamine dye emits light at a band of wavelength of 551 nm when illuminated by the 532 nm light from the laser used during this project, a Quanta-Ray PIV-400 double pulsed Nd:YAG laser made by Spectra-Physics. [29] This laser emits light with a maximum pulse energy of 400 mJ. The maximum operating frequency is 15.4 Hz (set at 15 Hz for this research), while the duration of each laser pulse is 8 ns. These pulses were set 0.5 ms apart. During operation, the laser light beam is reflected using a series of mirrors to the points of interest. For impingement images, the light beam was directed through the glass impingement surface to illuminate the droplets from the bottom. For images at the nozzle exit, the light beam came from the bottom and from the front. Both of these light beam baths are illustrated in Figure 4.4.

The camera that was used throughout this experiment is a Kodak MegaPlus ES 1.0 8-bit camera. The camera is capable of taking double frame images at a rate of 15 Hz. The time between the double frames can be varied, and ranges from 1 μs to

32,000 μs. Attached to this camera is a Mitutoyo 10x magnifying lens, which results in a field of view of 4 mm by 4 mm. A Melles Griot 600/40 nm bandpass filter is placed over this lens so that the 532 nm light from the Spectra laser is filtered out. Therefore the camera only captures the 551 nm light from the fluoresced droplets.

A camera mount was constructed to allow adjustments in all three orthogonal directions. A scissor jack allows for adjustments in the z-direction, while a translation stage moves the camera in the y-direction (into and away from the droplet generator) and a movable plastic mount allows for movement in the x-direction (to the left and right of the droplet generator). It should be noted that although a second camera is shown in Figure 4.3, which allows for pictures of the droplet from underneath as it impacts the glass surface, it will not be used for this particular research project.

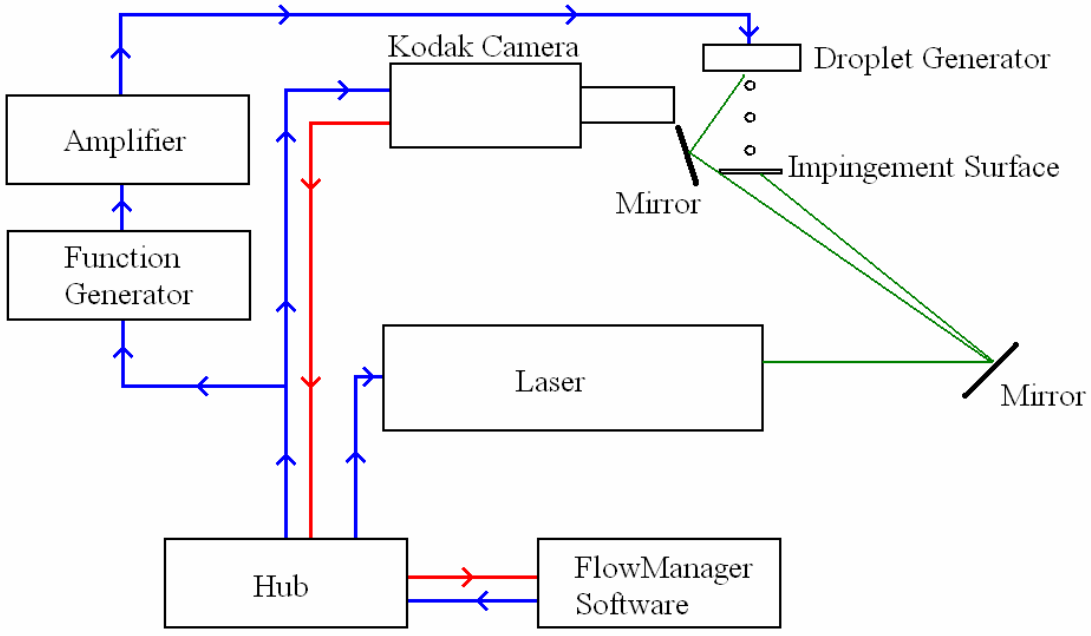


Figure 4.4
Experimental set-up schematic

Figure 4.4 shows a schematic of the experimental set-up. The FlowManager software (v. 4.50.17), published by Dantec Dynamics, is how the user inputs the desired delay between the two frames of the double image, and how many sets of double frame images are to be taken. When the program is started, FlowManager communicates with the FlowMap System Hub, which then outputs two separate signals – one signal to the laser and another to the camera. These signals are already synchronized when coming out of the hub. With this set-up, one laser pulse occurs in each of the two frames of a double image, resulting in clear, frozen images of droplets.

In order to synchronize the droplet generator to the camera, a BNC splitter was used so that the camera and the function generator are controlled by the same trigger signal. The waveform programmed into the function generator could be modified to change the timing of the pictures. Switching from pictures of a droplet emerging from the nozzle, to pictures of the droplet after break-off, simply required a change in the waveform being used to control the piezoelectric element.

Once the camera has taken pictures of the droplet, the images are sent through the hub to the FlowManager software, where the images are stored on the computer.

# 5. DATA ANALYSIS AND TEST PLAN

This section outlines how all the necessary information required for this project was measured. Then a test plan is outlined that specifies the operating conditions for the experiments.

## *5.1 Data Collection & Analysis*

There were several measurements that needed to be made during this research. These included the displacement of the brass disk during operation, droplet velocity at the nozzle, the volume of a droplet, and the spread rate and contact angle of a drop after impingement. This section details how the necessary information was collected and analyzed in each case. The uncertainty analyses for these calculations can be found in Appendix B.

### *5.1.1 Displacement of Brass Disk*

The first measurement that was taken was the displacement of the brass disk during normal operation as it pulses back and forth. There are two very important reasons for taking this measurement. The first is that in order to accurately model the droplet generator numerically, it is necessary to know how to describe the behavior of the moving plate that causes droplets to be ejected. Secondly, future experiments using this same device could possibly control the velocity of the droplet based on how much the brass disk is allowed to displace.

To take these measurements, an AccuRange 600 laser displacement sensor, made by Acuity Research, Inc. was used. The sensor works by beaming a laser onto a surface, and then using a camera to view the reflected light and calculate a distance based on the principles of triangulation. This distance is then displayed on a digital readout in inches. The laser was beamed onto the bottom of the piezoelectric element bonded to the brass disk while the droplet generator was operating. The position of the piezoelectric element was recorded over a range of applied voltages. Figure 5.1 displays the displacements measured, plotted against the voltage being supplied to the piezoelectric element. This voltage is measured after passing through the amplifier – it is not the output directly out of the function generator.

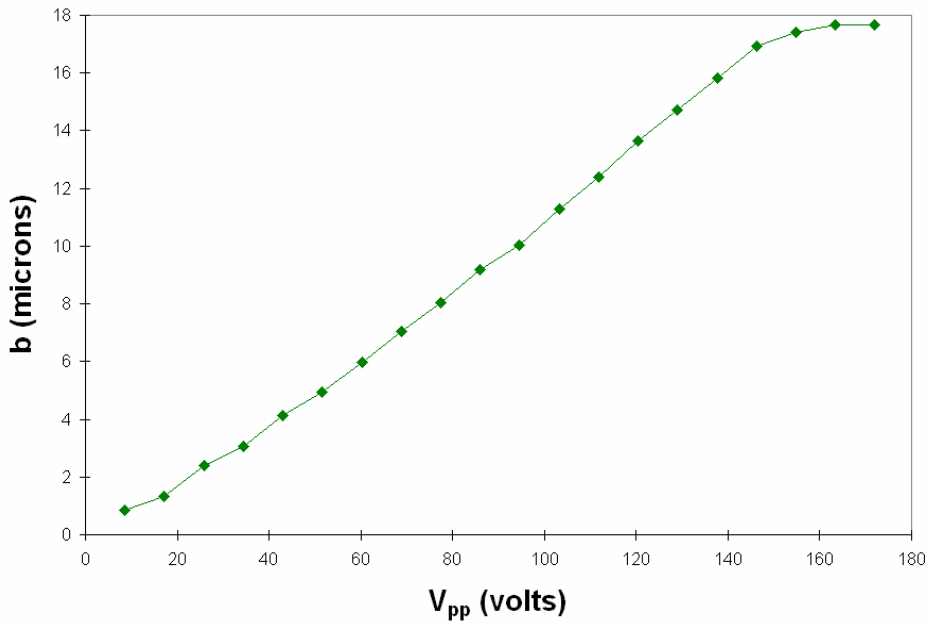


Figure 5.1
Characterization of brass disk displacement versus applied voltage

The last data point in Figure 5.1 represents the maximum displacement of the disk. Any voltage exceeding 170 volts results in the same disk displacement. This

maximum displacement was measured to be 17.65 microns, with an uncertainty of +/- 0.05 microns. A linear regression was done on the data until maximum displacement, which resulted in the following equation:

$$b = 0.118V - 0.79 \quad , \text{V} < 160\text{V} \tag{8}$$

where b is the displacement of the disk and V is the applied peak-to-peak voltage. This linear fit has a $R^2$ value of 0.9927. Although it is possible to generate droplets when the brass disk is operating at less than its maximum displacement, the maximum displacement was used to generate the droplets studied throughout this research.

### *5.1.2 Data Collection Timeline*

To clarify what exactly is happening during the data collection process, Figure 5.2 shows a timeline of everything that occurred during image capture. There are actually three different timelines – one for the laser, one for the camera, and one for the droplet generator.

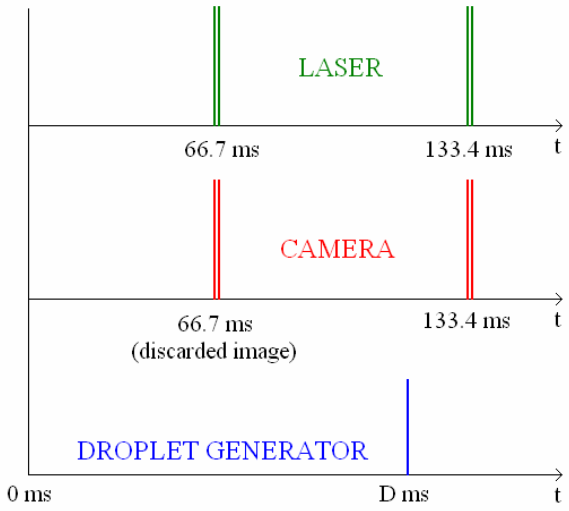


Figure 5.2
Data collection timeline

The camera-laser relationship is straightforward. The camera operates at 15 Hz, so the first two sets of double frames are taken at the specified times. The laser is synchronized with the camera through the hub, so that one laser pulse is fired during each camera exposure. The droplet generator is fired after specified delay of D ms as discussed in the previous section. D was set at 100 ms to see the beginning of the droplet formation (meaning it takes 33 ms after the brass disk pulses inward for the drop to begin to emerge from the nozzle). With this set-up, the droplet was observed on the second set of double frames. It would also be possible to shift D back 66.7 ms to observe the droplet in the first group of frames, but then it is only possible to shift D back 33 ms before hitting zero. Therefore, it was decided to start D at 100 ms in order to make it easier to look at the droplet past 33 ms. Therefore, the first set of double framed images is ignored.

### *5.1.3 Waveforms*

It was previously mentioned that when looking at droplet behavior near the nozzle, two different waveforms were used. The first of these waveforms was a square wave with a period of 1 second, shown in Figure 5.3. The square wave starts out at a negative voltage, then jumps to a positive voltage after a specified delay. In this experimental set-up, a negative voltage causes the brass disk to pull outwards, which causes fluid from the refill port to be drawn into the fluid chamber. When the voltage becomes positive, the brass disk pulses inward, creating a pressure wave that forces fluid out through the nozzle. When a square wave was used to drive the piezoelectric element, the positive voltage was maintained for 500 ms, so that the

brass disk was held stationary for the entire time the droplet emerges, and eventually breaks off, from the nozzle. Since the brass disk does not return back to its original position until long after droplet break-off, it can be considered a step-function from the point of view of the droplet. The voltage only goes negative to refill the fluid chamber for the next trial. This square wave is labeled "waveform A" in Figure 5.3.

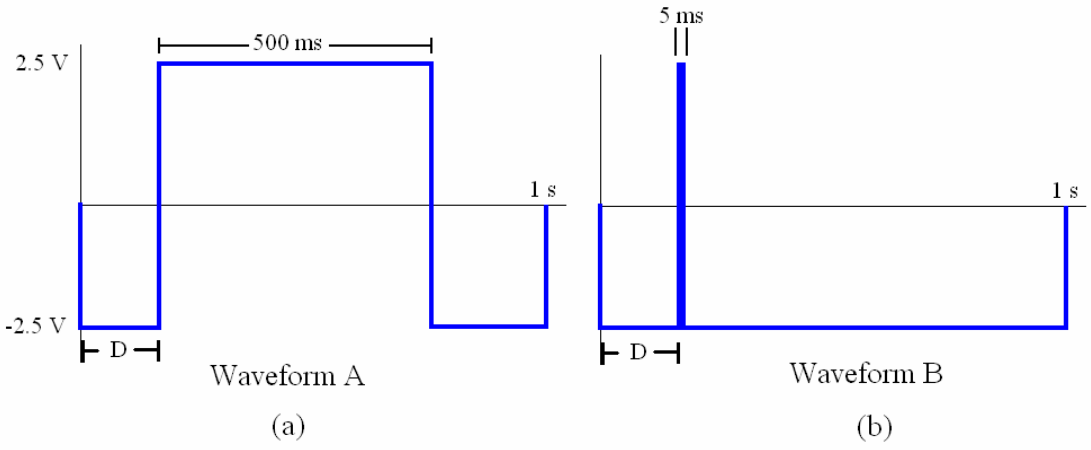


Figure 5.3
Waveform illustrations with variable time delay D
(a) long square wave, "waveform A" (b) short square wave, "waveform B"

The second waveform that was used to drive the piezoelectric element is a 5 ms square wave pulse, "waveform B". In this case, the voltage again starts out as negative, but 5 ms after the voltage jumps to positive, it then drops back down to negative. A droplet generally takes 44 ms from the time the brass disk pulses inward to actually break off from the nozzle. Therefore, this short pulse occurred before break-off and affects the behavior of the droplet formation.

The variable D in Figure 5.3 is the delay in time from when the waveform begins to when the voltage becomes positive. This delay is what determined the

timing of the images that the camera captured. For example, setting D equal to 100 ms resulted in images where the droplet had just barely begun to emerge from the nozzle. Shifting this delay to 90 ms resulted in a double framed image of the droplet just before break-off. This is because the droplet generator now fires 10 ms earlier relative to when the camera captures an image, so the camera observes the droplet at a later stage of its formation. Over a hundred of these waveforms were programmed into the function generator with different values of D. They are all labeled as xxxA or xxxB, where xxx is the D value such as 090 for a 90 ms delay. On the plots displaying results of this research, the data sets are labeled "waveform A" or "waveform B" to distinguish between these two waveforms.

### *5.1.4 Droplet Velocity*

Droplet velocity, both before and after break-off, was calculated by comparing the two images of a double image set. The time difference between the two images was kept constant throughout the project at 0.5 ms. Because the images were of very good quality, with clearly defined edges, it was not necessary to do any type of image processing. Therefore, the data collection process could be done entirely within the FlowManager software.

Figure 5.4 shows one set of images. Panel (a) shows the first frame of a double image set, while the second image is in panel (b).

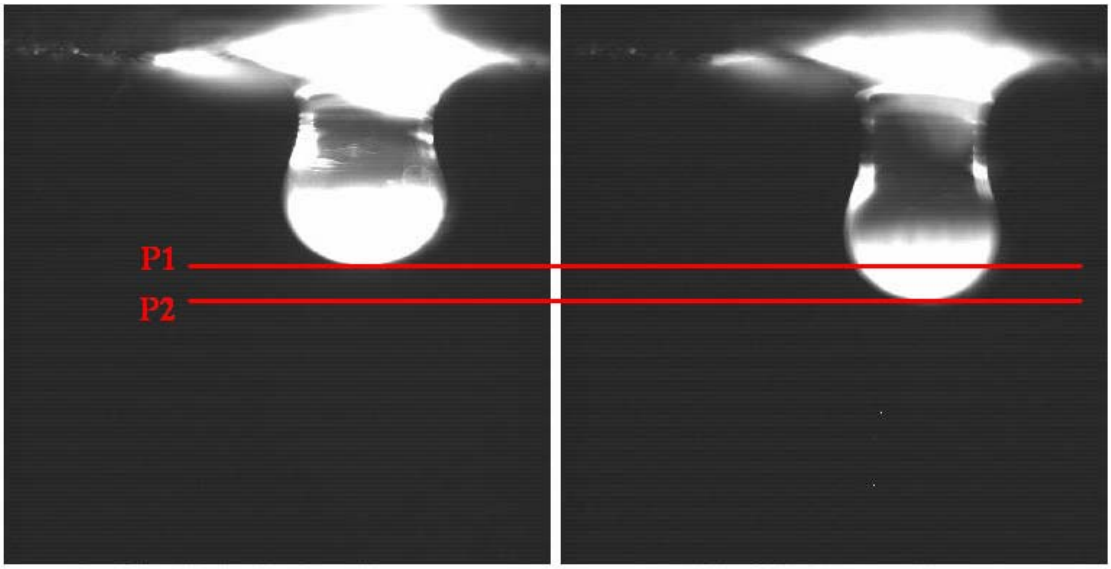


Figure 5.4
Leading edge velocity calculation
(a) first image (b) second image 0.5 ms later

P1 represents the position of the leading edge in frame 1, while P2 represents the leading edge in frame 2. The FlowManager software collects images with a resolution of 1008 x 1016 pixels. By zooming in a region of interest, in this case the leading edge, the FlowManager software will display the pixel location of the leading edge. The process is repeated for the second frame, and the change is position is recorded. Therefore, the velocity of the leading edge can be found using the following equation,

$$v = \frac{P1 - P2}{\Delta t} C_f \qquad (9)$$

where the pixel-to-meter conversion $C_f$ was determined experimentally by capturing an image of an object with a known width.

This same equation was used to calculate the velocity of a droplet immediately before impingement, except that a different conversion factor $C_i$ was used for impingement analysis since the camera was repositioned and refocused to capture impingement images. An example of the images used for this calculation is shown in Figure 5.5.

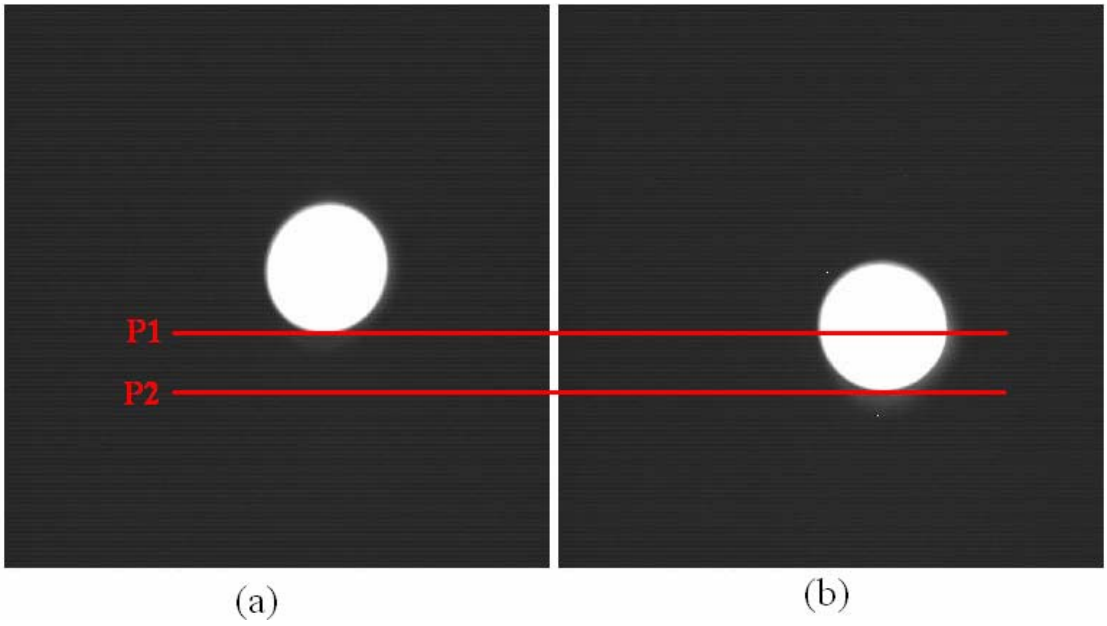


Figure 5.5
Impingement velocity calculation
(a) first image (b) second image 0.5 ms later

By the time a droplet was about to hit the impingement surface, it had achieved a stable, spherical shape. Velocities for the leading edge and trailing edge were the same, so only one velocity calculation was performed. This was not the case when looking at the drop shortly after break-off. Due to instabilities that occur as the liquid thread merges with the main body of the droplet, the leading edge and trailing edge velocities were found to be very different. However, the method for calculating the trailing edge velocity was the same.

### *5.1.5 Spread Rate*

A similar process as the one outlined in the previous section was used to determine the spread rate of the droplet after impingement. The difference is that the change in position is now tracked horizontally instead of vertically, as Figure 5.6 illustrates.

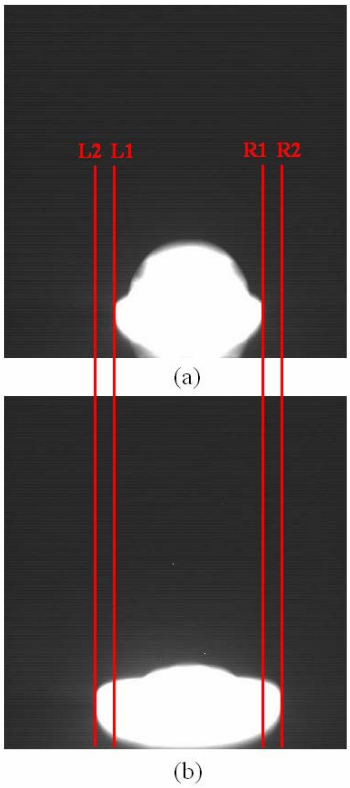


Figure 5.6
Spread rate calculation
(a) first image (b) second image 0.5 ms later

Initially, the spreading velocity for the left and right sides of the drops were calculated independently. This was done by observing the change in position of the leading edge of the spreading drop, and then using the following equation,

$$v_{spread,L} = \frac{L1 - L2}{\Delta t} C_i, \quad v_{spread,R} = \frac{R2 - R1}{\Delta t} C_i \qquad (10)$$

Once the velocity of each side was calculated, the two spread rates were averaged together to yield U, the average spread rate for the droplet at that particular point of impingement.

### *5.1.6 Contact Angle*

The contact angle of a drop is defined as the angle that the liquid/vapor interface makes with the solid surface measured through the liquid. In this case, it is the angle the droplet surface makes with the glass slide. The contact angle is dependent on the behavior of the spreading drop. If the leading edge of the drop is advancing, then the contact angle will typically be greater than 90 degrees. After the droplet has reached its maximum spread and is receding, the contact angle is less than 90 degrees. Figure 5.7(a) illustrates how a static contact angle was calculated. This same method was used to calculate receding contact angles, as seen in Fig. 5.7(c).

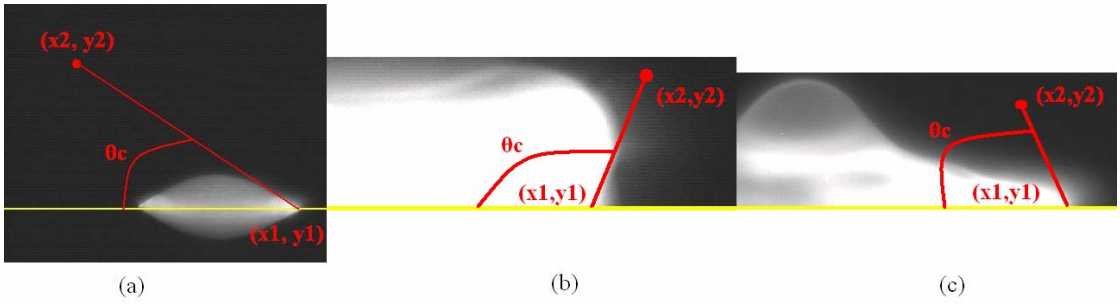


Figure 5.7
Contact angle calculation
(a) static contact angle (b) zoomed-in region of advancing contact angle
(c) zoomed-in region of receding contact angle during the rebound stage

Contact angles were measured from the liquid-solid interface on the right-hand side of the image in all trials. The horizontal line in Figure 5.7 represents the glass surface.

The pixel location of the water-air-glass interface was located and described by the coordinates (x1, y1). Then a straight line was constructed along the droplet surface and a second point was selected on this line. The pixel value of this location was then defined as (x2, y2). Trigonometry was then used to determine the contact angle $\theta_c$, as shown in Eq. (11).

$$\theta_c = 90 - \tan^{-1}\left(\frac{|x2 - x1|}{|y2 - y1|}\right) \tag{11}$$

Advancing contact angles were calculated using the same method. An example is shown in Fig. 5.7(b), where the picture has been cropped at the glass surface (to prevent confusion due to the mirror image). The one difference was that the line along the liquid surface was taken out to the right edge instead of the left, since the advancing contact angles were greater than 90 degrees, so that Eq. (12) was used.

$$\theta_c = 90 + \tan^{-1}\left(\frac{|x2 - x1|}{|y2 - y1|}\right) \tag{12}$$

It should be emphasized that a significant amount of error can be introduced due to the subjective nature of this measurement. It is up to the user to estimate the location of the glass surface by looking at the mirror reflection (as in Figure 5.7(a)). The user is then required to estimate the line along the liquid surface near the vicinity of the liquid-solid interface. The accuracy of this estimate depends on the illumination level of the droplet, its stage in the spreading process (the closer the contact angle is to vertical, the more difficult this estimate becomes), and user judgment. So while the information required for this measurement was taken by the author in the same way every time, this is the one aspect of the experiment where results could vary based on

the judgment of the person analyzing the data. This is important to keep in mind when looking at results, especially since this human factor is not reflected well in the uncertainty analysis carried out in Appendix B.

### *5.1.7 Droplet Volume*

Calculating the volume of a droplet was done by measuring the diameter of a droplet as it approached the impinging surface. This location was chosen for this measurement because at this point, the droplet had stabilized into a spherical form, which was not the case in the vicinity of the nozzle.

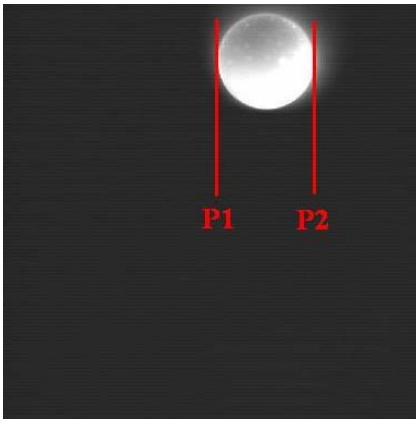


Figure 5.8
Droplet volume calculation

The droplet was assumed to be a perfect sphere, and Eq. (13) was then used to calculate the total volume.

$$V = \frac{4}{3}\pi\left(\frac{(P2 - P1)C_f}{2}\right)^3 \tag{13}$$

### *5.1.8 A Comment on the Plotting of Results*

When constructing time plots after leaving the nozzle, the independent variable on the horizontal axis is time. However, there are two different ways of approaching this. The first method would be to plot velocity and position versus the time after the brass disk has been pulsed inward. The second method would set t = 0 at the instant a droplet begins to emerge from the nozzle. For the purpose of presenting the results as clearly as possible, the second method is used. It may seem like beginning time when the brass disk is pulsed forward would make the most sense, since this is technically the beginning of the droplet formation process. However, there is a delay of 33 ms before liquid begins to emerge from the nozzle that depends on the droplet generator design. As a result, defining the time according to the first method results in graphs that look like Figure 5.9.

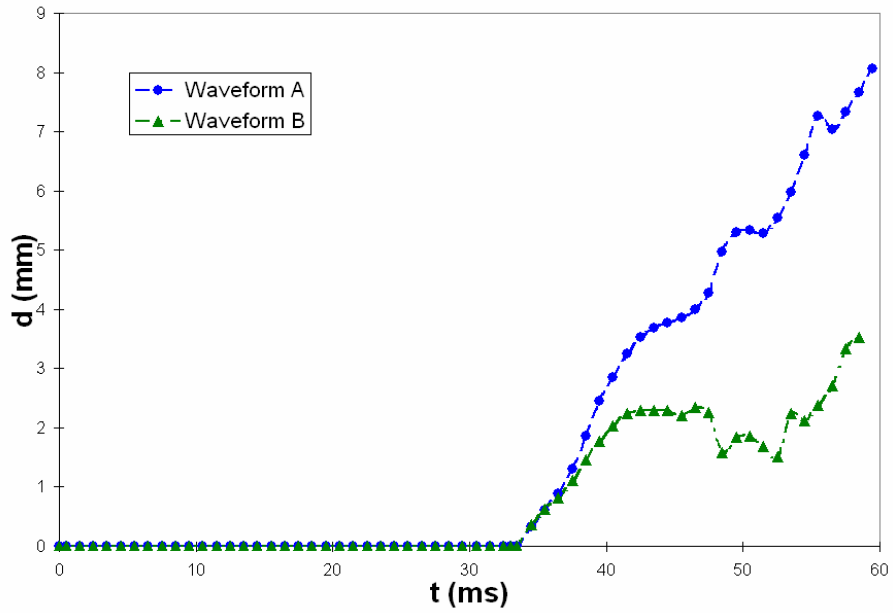


Figure 5.9
Time trace using piezoelectric timing from the beginning of the positive pulse of the waveform

Including the 33 ms delay in plots only serves to compress the region of the plot that is actually of interest, and this delay would likely be different for a different fluid chamber geometry. Therefore, it was decided to eliminate this region from all future plots by shifting all data 33 ms to the left. All plots of formation will have t = 0 be the time at which the droplet just begins to emerge from the nozzle opening.

### *5.1.9 Uncertainties*

In Appendix B, the uncertainties for each of the measurements previously discussed are listed in detail, as well as standard deviation values when appropriate. The equations used to calculate these uncertainties are also provided. This section will provide a brief summary of these results.

All data analysis was based on a pixel-to-meter conversion that was determined experimentally. Two different coefficients were calculated. One for the formation process, and one for the impingement process. Both were similar and overlap each other when the error ranges are considered, but there may be slight differences due to small camera adjustments required to get the clearest picture in each situation. For the formation process this coefficient had an error of 4.6%, where the coefficient was $C_f = 4.31 \times 10^{-6} +/- 2 \times 10^{-7}$ m/pixel. For the impingement process the coefficient was $C_i = 4.44 \times 10^{-6} +/- 1 \times 10^{-7}$ m/pixel, which is an error of 2.3%.

For velocity measurements, the average calculated error had a range between 5.0% and 5.9%, depending on which of the nozzle and waveform cases was being examined. The average error for leading edge position measurements was slightly lower, at 4.5%.

Uncertainties were higher when looking at the impingement process. For the spread rate, the average error was approximate 9% for the stiff nozzle case, and approximately 5.5% for the flexible nozzle case. For the contact angle, the average error was calculated to be .01%. However, this is too low as it does not account for the human error presence that was discussed in Section 5.1.6.

## *5.2 Test Plan*

The goal of this research is to determine the effects of a flexible nozzle versus a stiff nozzle on droplet formation. Although the droplet generator can be modified for a wide range of fluid chamber geometries and nozzle properties, it was decided to simply select the set-up that produced the most reliable droplets, and remain with that set-up throughout the research. Therefore, the 3.175 mm diameter nylon insert was placed in the fluid chamber of the droplet generator for the duration of the project. A nozzle hole of 1 mm was used in all experiments.

In order to make stiff nozzle vs. flexible nozzle comparisons, two different nozzle plates were used. The stiff nozzle plate is constructed of ANSI 304 steel 0.787 mm thick. The flexible nozzle plate is constructed of ANSI 304 steel 0.102 mm thick. Because the deflection of a flat plate is inversely proportional to $h^3$, where h is the plate thickness, the flexibility of the 0.102 mm thick nozzle plate will be approximately 465 times greater than the stiff nozzle.

The two areas of interest during the life of a droplet are the behavior at the nozzle exit, and at the impingement surface. At the nozzle, during the formation of the droplet, both quantitative and qualitative observations were made. Double frame

images were used to obtain the velocity and position of the droplet as it leaves the nozzle. The volume of a droplet after break-off was also obtained at this time. Qualitatively, the behavior of the droplet at the moment the liquid thread breaks was viewed and compared for the different nozzle cases. Two different waveforms were used when examining this behavior, as the behavior of the brass disk can have a dramatic impact on the droplet shape and velocity. In addition, any effects of the liquid thread merging with the main body of the droplet were observed. Five sets of double framed images were taken at each 1 ms time step during the formation process. The velocity and position data were then be averaged together, and an average value was reported.

At the impingement surface, the spread rate of the droplet was determined quantitatively, as well as the contact angle of the droplet at different points during the spreading process. The impingement surface was located 4.22 cm below the nozzle. Droplet velocity at the point of impact was also determined. Because it is not possible to obtain pictures of the drop at a known time after impingement due to the unpredictable timing of droplets near the impingement surface, these spread rate velocities will be related to the diameter of the droplet. All values reported for impingement results are individual data points, no averaging occurred (unless explicitly stated).

# 6. RESULTS

This section addresses each of the two cases that were examined, the stiff nozzle and the flexible nozzle, individually. The quantitative results at both the nozzle exit and the impingement surface are discussed. Any notable qualitative observations are also mentioned. This section concludes with some direct comparisons between the two cases.

## *6.1 Stiff Nozzle Results*

The results for the stiff nozzle have been divided into two different categories. The first is droplet behavior in the vicinity of the nozzle, including droplet velocity and position data. Second is the impingement process, which includes the droplet diameter and velocity before impingement, the spread rate of an impinging droplet, and the contact angle that is observed. Qualitative observations will be discussed when appropriate.

### *6.1.1 Droplet Formation Results*

The first item of interest when looking at the droplet formation process is the droplet velocity during and immediately after the break-off process. The velocities were calculated according to the method described in Section 4.4. Due to the fact that the droplet is not stable when it first breaks off from the nozzle, both the leading edge velocity and the trailing edge velocity were tracked, with the trailing edge velocity set

at zero until after break-off occurs. The droplet velocity was measured for both the square wave (waveform A) and the 5 ms pulse (waveform B).

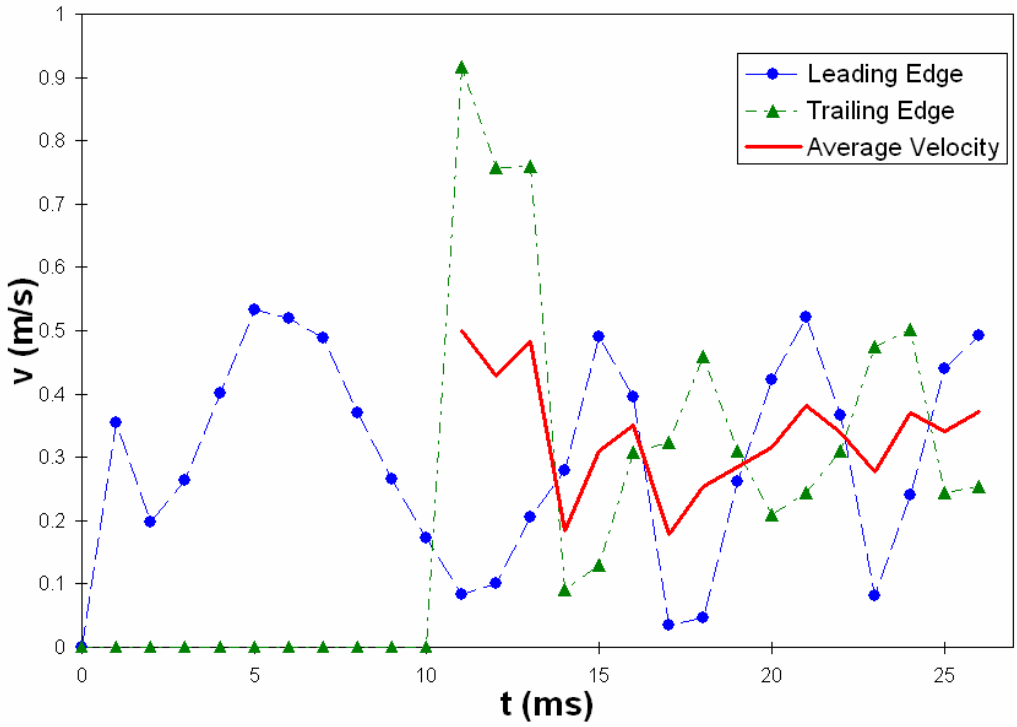


Figure 6.1
Droplet velocity for waveform A, stiff nozzle

Figure 6.1 depicts the leading edge velocity (circular points) and the trailing edge velocity (triangular points) of droplets produced using waveform A. The solid line is the average velocity. As the trailing edge line indicates, the break-off time for these droplets is 11 ms from the time the drop begins to emerge from the nozzle opening, and 44 ms from the time the brass disk is pulsed forward.

The circular points serve as a visual indicator of what exactly is happening to the leading edge of the droplet during the formation process. The velocity of the leading edge initially increases as the drop first emerges from the nozzle. However, as

the droplet nears the break-off point, it nearly comes to a halt as the liquid thread is stretched and pulls back on the drop. Once the liquid thread finally breaks, the liquid thread accelerates forward, reaching a velocity of nearly twice that of the body of the main droplet, before merging with the body, as seen in Figure 6.2.

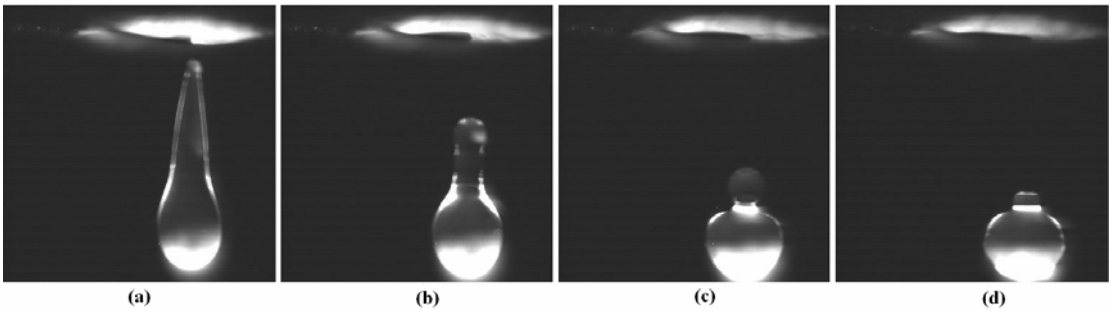


Figure 6.2
Merging liquid thread sequence
(a) drop immediately after break-off (b) trailing liquid drawn towards drop
(c) near the end of the merging process (d) surface disturbances observed

The merging of the liquid thread causes the droplet to become unstable, and it begins to pulse. The shape of the droplet then alternates between being elongated horizontally and vertically. This is indicated by the oscillating leading and trailing edge velocities that are out of phase with each other. This pulsing behavior is shown in Figure 6.3. The period of this behavior is approximately 6 ms.

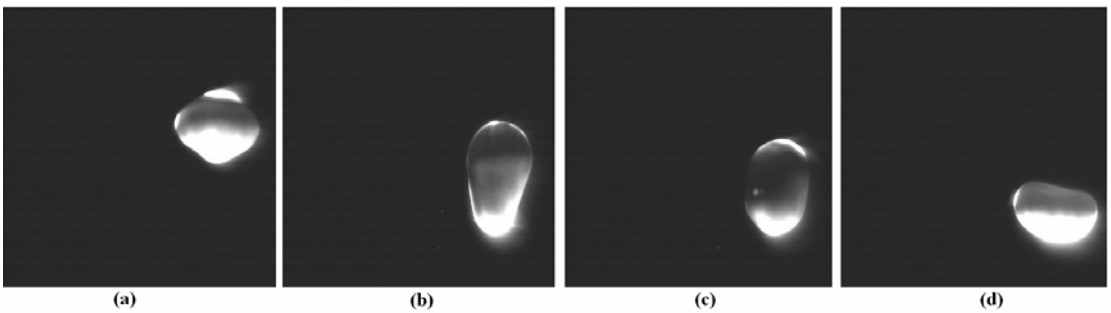


Figure 6.3
Pulsing drop sequence
(a) round shape at t = 14 ms (b) t = 16 ms (c) t = 17 ms (d) t = 19 ms

This series of four images shows droplets created by waveform A. Panel (a) contains a somewhat round drop. However, panels (b) and (c) are images taken 2 ms and 3 ms later, respectively, during the formation process. The droplet now has an elongated shape. 2 ms after panel (c), and 5 ms after panel (a), the droplet has now returned to its flattened shape. This behavior repeats itself, until eventually dampening out so that the droplets become spherical before impingement.

Figure 6.4 shows the droplet velocity data using waveform B, a 5 ms pulse. Because the brass disk pulses forward and then is drawn backward before break-off occurs, the behavior of the droplet is very different.

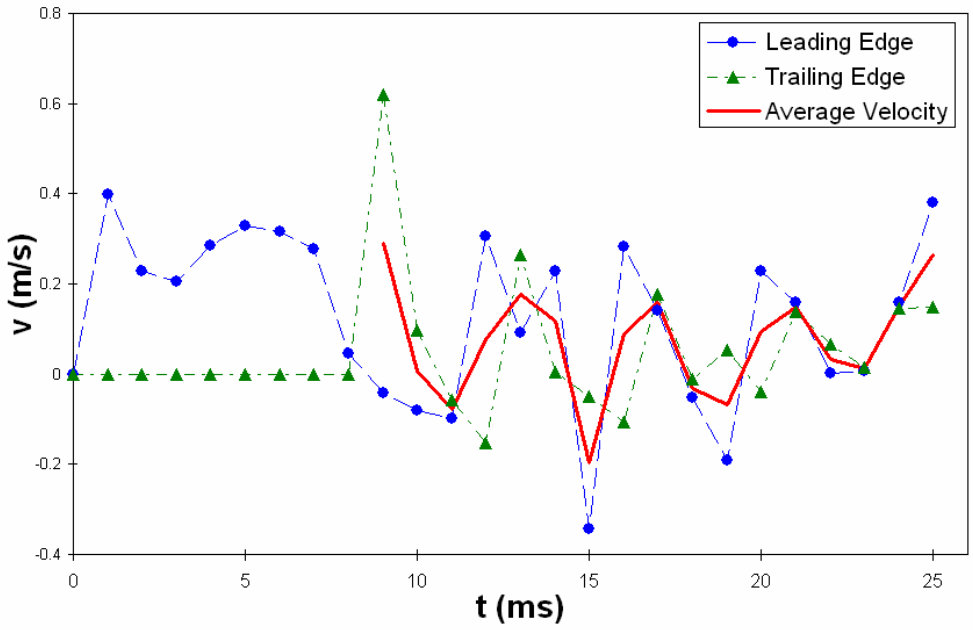


Figure 6.4
Droplet velocity for waveform B, stiff nozzle

There are several major differences when a 5 ms pulse is used. First, the droplet breaks off from the nozzle slightly earlier. Also of note is the fact that the

average velocities are not as large as when waveform A is used. This is because some of the fluid is being drawn back into the nozzle during the break-off process, so the main body of the droplet does not have as much forward momentum.

Another difference when comparing velocities between the two waveforms is that while the leading and trailing edge velocities for droplets produced by waveform A were approximately 180 degree out of phase throughout the entire observed time period, this is not the case with waveform B. These waveform B droplets behave more erratically than those produced by waveform A, and it is therefore difficult to determine the period of the pulsing behavior for waveform B.

However, the most noticeable difference between Figures 6.3 and 6.4 is that when a 5 ms pulse is used, negative velocities of both the leading and trailing edges are observed. This indicates that once the liquid thread breaks, there is enough upward momentum from the retracting meniscus that the droplet actually moves back up towards the nozzle before finally beginning to proceed downwards again, which is illustrated in Figure 6.5.

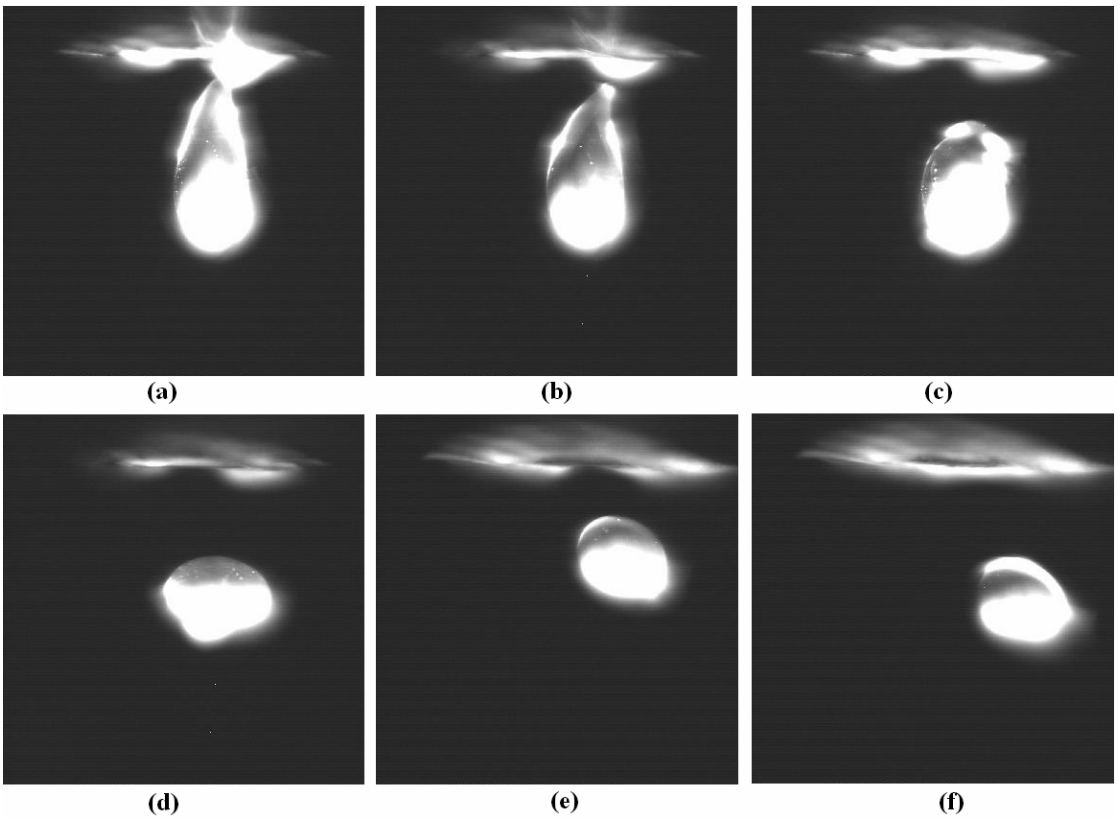


Figure 6.5
Behavior at the nozzle due to waveform B
(a) drop before break-off (b) drop immediately after break-off
(c) liquid thread has merged (d) drop has attained upwards momentum
(e) drop has moved upwards (f) drop begins to move back down

Panels (a) – (c) are images taken 0.5 ms apart during the formation process. Break-off occurs in panel (b). At this point liquid is drawn back into the droplet generator, so that the droplet is actually given some backwards momentum. Panels (d) – (f) are images taken 4 ms apart. The drop in panel (d) is no longer elongated as it was in panel (c), and is slightly higher up in the frame. The position becomes even higher in panel (e), before finally beginning to fall back down in panel (f). Note that the droplet is slowly moving to the right of the frame throughout this process. This is why waveform B could not be used with the stiff nozzle to create drops for

impingement. The horizontal velocity that was imparted during the break-off process made the location and timing of the drops too unreliable.

Figure 6.6 is the position of the leading edge of the droplet plotted against the time after the piezoelectric element has been activated. The pulsing behavior of the droplets can also be recognized in this plot, as the slope of the lines alternate between steep and shallow. It also clearly shows the point at which the droplet begins to travel back towards the nozzle plate when waveform B was used. Note that since the diameter of the droplets being produced was 1 mm, on average, the droplet comes less than 1 mm away from colliding with the nozzle plate before going back down towards the impinging surface. However, an actual collision with the nozzle plate was never observed during this study.

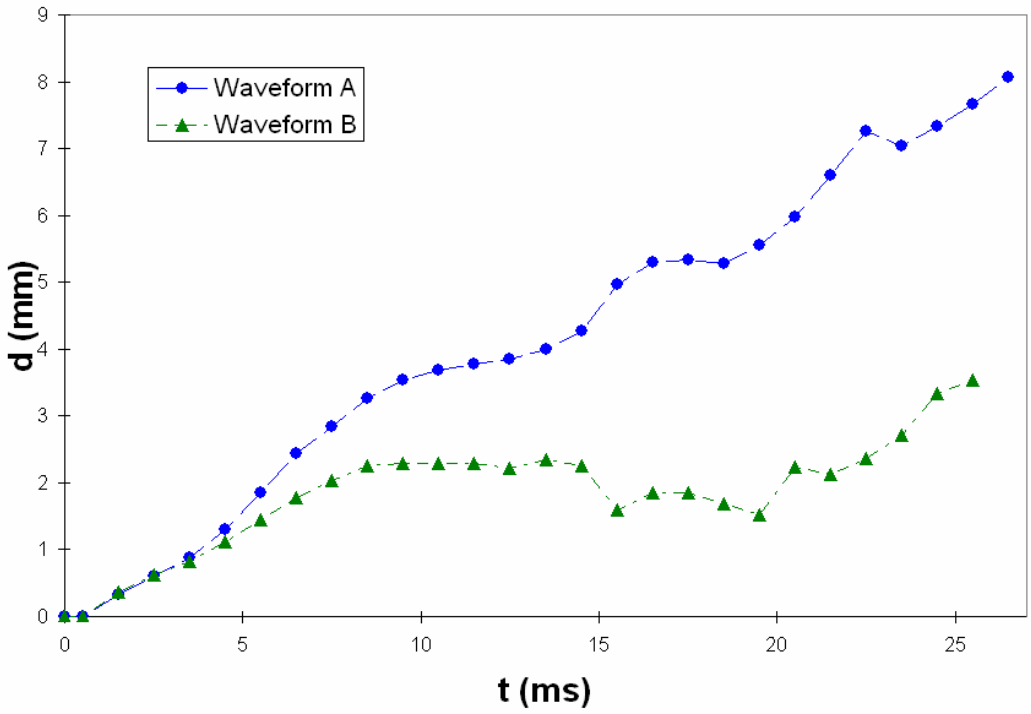


Figure 6.6
Position of the leading edge for each waveform, stiff nozzle

Figure 6.7 compares the velocities of the leading edge of the droplets for each of the two waveforms. Initially the two datasets exhibit similar behavior. However, the lines begin to diverge significantly 4 ms after the droplet begins to emerge from the nozzle opening. From this point forward, not only is the behavior more unpredictable for waveform B, but the maximum observed velocity is smaller as well, which accounts for the large difference in leading edge positions seen in Figure 6.6. These factors, in addition to the fact that the droplet is given some horizontal velocity as it moves back towards the nozzle after break-off, leads to the decision to use waveform A when creating droplets for impingement.

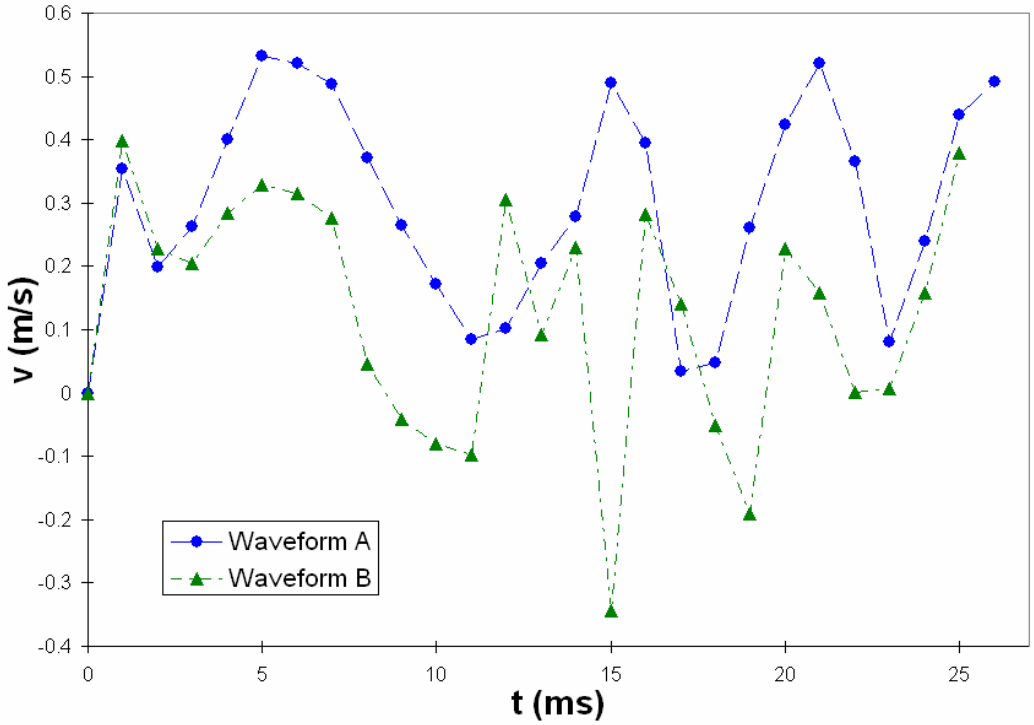


Figure 6.7
Comparison of leading edge velocities for both waveforms, stiff nozzle

To summarize, the effect on the waveform governing the behavior of the piezoelectric element has a tremendous impact on the droplet formation process. The droplet exhibits some pulsing behavior in each case, since this is unavoidable when the liquid thread merges with the main body of the drop. However, the behavior is much more predictable when the brass disk is held in place until after the droplet has broken off from the nozzle. Therefore, waveform A was selected to drive the piezoelectric element when running impingement trials.

### *6.1.2 Droplet Impingement Results*

For this study, the two parameters of interest when examining droplet impingement are the spread rate of the drop U, and the contact angle $\theta_c$. Waveform A was used to produce droplets for impingement. This results in droplets with an average velocity of 0.79 m/s immediately prior to hitting the impingement surface. The average diameter of these droplets was 1.13 mm. When spread rate results are plotted versus the diameter during spreading, they are normalized by these values immediately before impingement, which are referred to as $V_o$ and $D_o$.

Before looking at the actual numerical data, it is useful to first examine the general behavior of a spreading droplet under the experimental conditions of interest. This behavior is displayed in Figure 6.8.

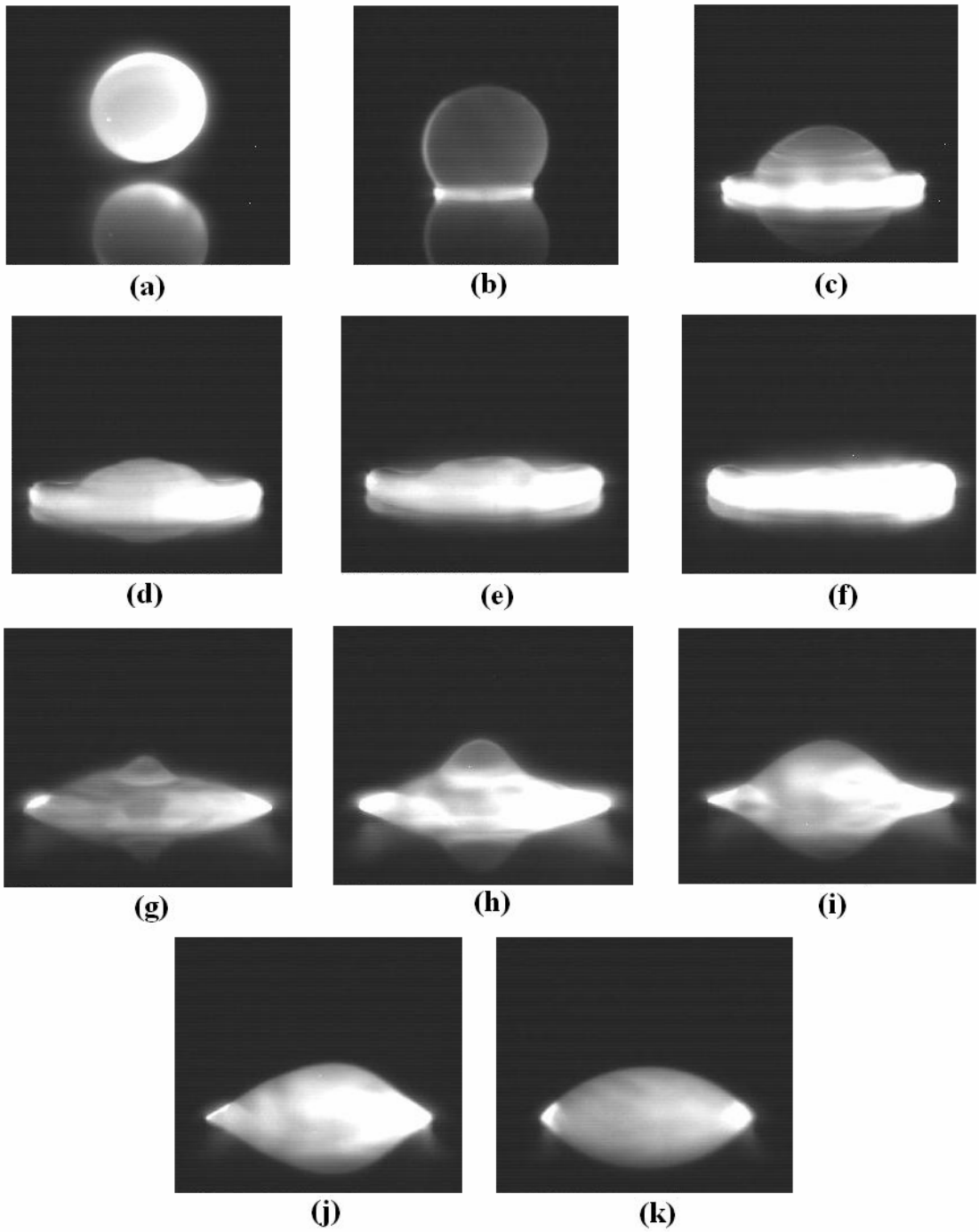


Figure 6.8
Spreading droplet behavior
(a) drop before impingement (b) initial contact (c) half of the drop has spread
(d) drop continues to spread (e) nearing maximum spread (f) maximum spread
(g) drop edges rebound towards the center (h) maximum rebound
(i) drop begins to settle (j) small surface disturbances observed (k) drop at rest

In Figure 6.8, panel (b) shows the droplet immediately after it comes into contact with the impinging surface. It then spreads out as the rest of the droplet body continues towards the surface. Eventually, in panel (f), it attains its maximum spread diameter. At this point, a rebounding effect is observed. In panels (g) and (h), the liquid is drawn back towards the center, and the free surface rises upwards. The free surface begins to settle back down in panel (i), and continues to exhibit small oscillations before finally coming to rest in panel (k).

Figure 6.9 displays the spread rate data for these droplets. The impingement surface was located 4.22 cm below the nozzle exit. This distance is great enough that the droplets have had time to stabilize into spherical shapes, and no longer exhibit the pulsing behavior that was seen in the vicinity of the nozzle exit.

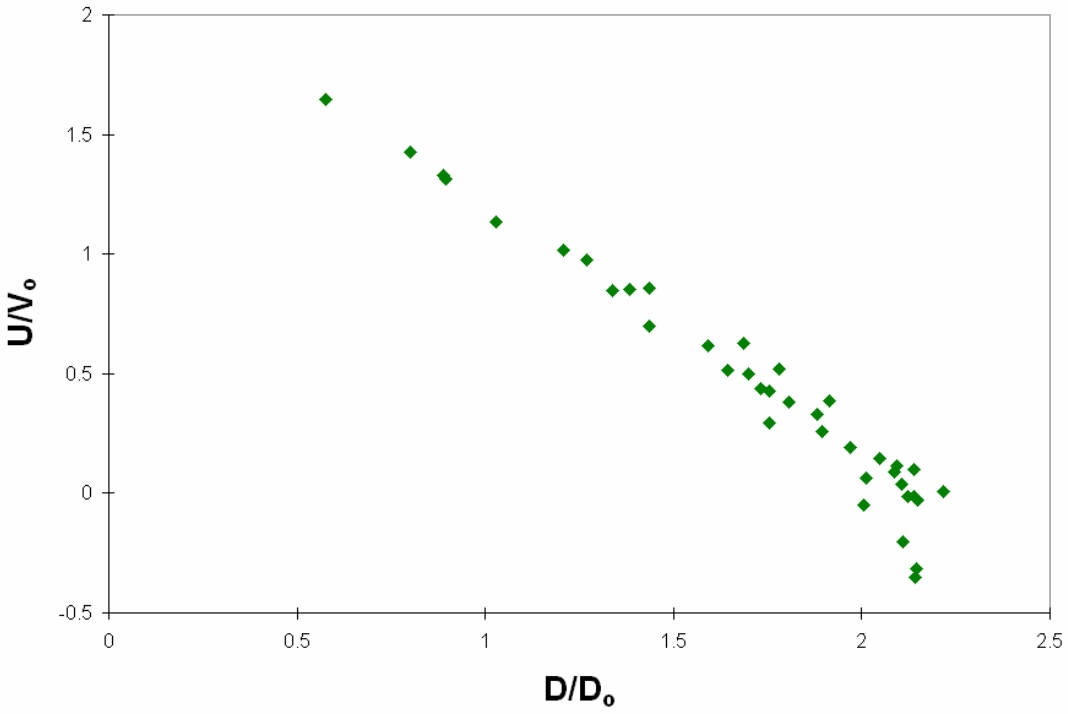


Figure 6.9
Spread rate of an impinging drop, stiff nozzle

When $D/D_o < 1$, the drop has just hit the glass surface, as in panel (b) of Figure 6.8. The spread rate is largest during these first moments after impact. At this point, the droplet can spread up to 1.3 droplet diameters in the 0.5 ms interval. The spread rate then decreases in a linear fashion, spreading 0.3 - 0.05 droplet diameters in a 0.5 ms interval. Eventually, the droplet reaches it's maximum spread distance. After this point, the spreading velocity actually becomes negative, as the rebounding effect occurs and the liquid at the edges of the spread droplet is drawn back towards the center. However, these rebound velocities are fairly small compared to the spreading velocities. Although there is a tremendous amount of movement along the free surface of the drop, the base of the drop that is in contact with the glass surface does not rebound much from its maximum spread.

In order to be able to compare these results to the impingement data for a flexible nozzle, a linear fit was applied to the data when $U/V_o > 0$. The resulting equation that describes the linear behavior of the data has an $R^2$ value of 0.9834 and is given as

$$\frac{U}{V_o} = -1.022\frac{D}{D_o} + 2.24 \tag{14}$$

The contact angle of the droplet was also observed. In this case, the contact angle was measured for select droplet diameters during impingement for both advancing and receding droplets. The results are displayed in Figure 6.10.

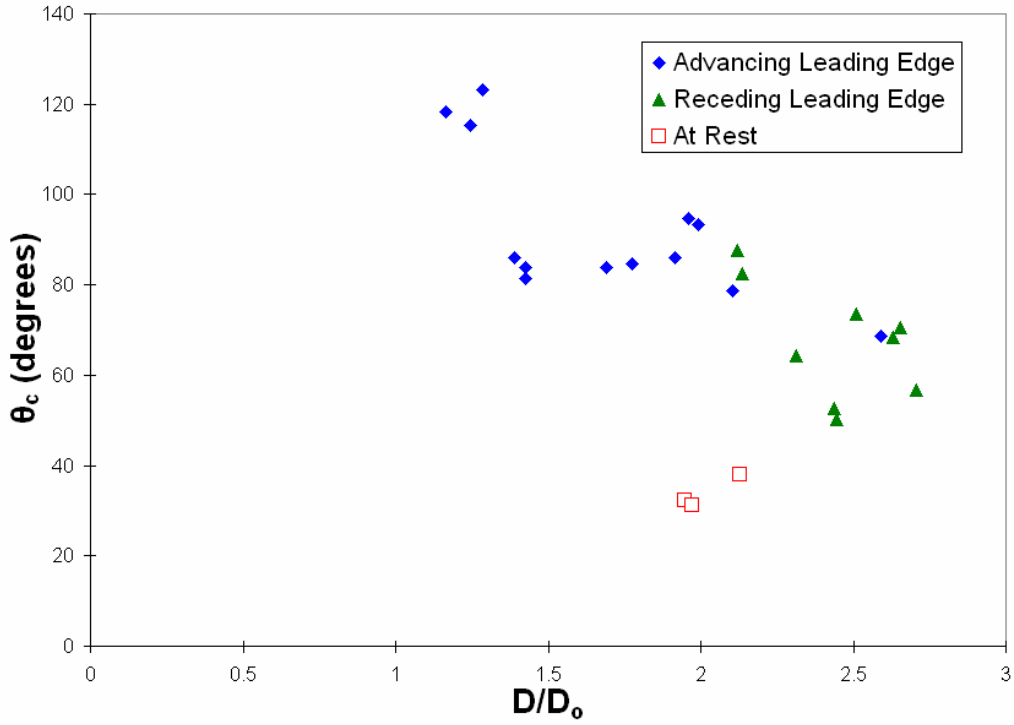


Figure 6.10
Contact angle versus droplet diameter, stiff nozzle

It was shown that the spread rate is largest immediately after contact with the impingement surface occurs. Therefore, the contact angle is the largest at these spreading velocities since viscous forces slow the fluid nearest the surface. The fluid farther away from the surface travels further, increasing the contact angle. As the edges approach their maximum spread diameter, the rebound effect that was illustrated in Figure 6.8 occurs and begins to draw the fluid surface back towards the center, which decreases the contact angle. Soon after this, the drop diameter also begins to retract, before finally reaching it's equilibrium shape indicated by the square data points. These points when the droplet is at rest indicate the static contact angle.

## *6.2 Flexible Nozzle Results*

The flexible nozzle used during this experiment was a 0.102 mm thick stainless steel plate. This changes two important nozzle characteristics. First, the nozzle deflects slightly during the droplet formation process, as described in Section 3. Second, the depth of the nozzle opening is greatly reduced since the nozzle plate is not as thick. This means the surface area that the fluid comes into contact with as it exits the fluid chamber is also reduced, so that more fluid can be ejected when compared to the stiff nozzle case, for a given pressure pulse.

### *6.2.1 Droplet Formation Results*

During the droplet formation process for a flexible nozzle, there were two major departures from the behavior during the stiff nozzle trials. The first of these was the formation of satellite droplets. Satellite droplets were not observed when a stiff nozzle was used. However, they were very common during the flexible nozzle trials. Figure 6.11 shows the droplet formation history using waveform A.

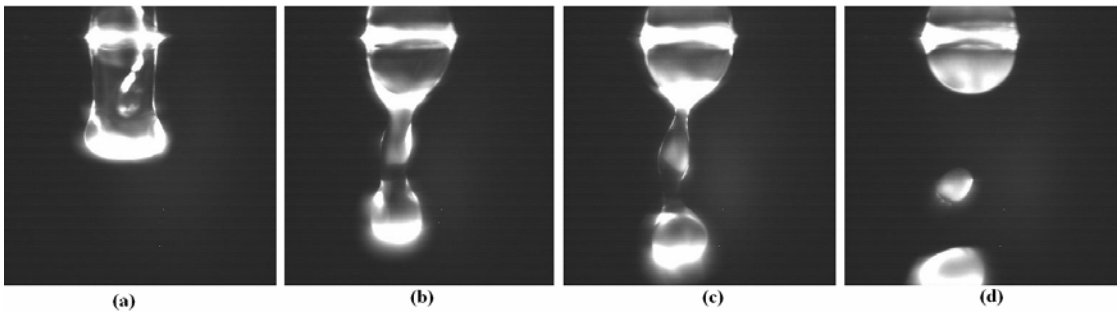


Figure 6.11
Satellite droplets due to waveform A
(a) drop emerges from nozzle (b) liquid thread begins to form
(c) double necking occurs (d) satellite droplet formed after break-off

The satellite drops occur due to the double necking of the liquid thread that is first observed in panel (b). This becomes more pronounced in panel (c). Finally, the liquid thread ends up breaking at both necks at once, and a satellite droplet is formed. Satellite droplets also occurred when using waveform B. However, the satellite droplets were much smaller in these cases, as can be seen in Figure 6.12.

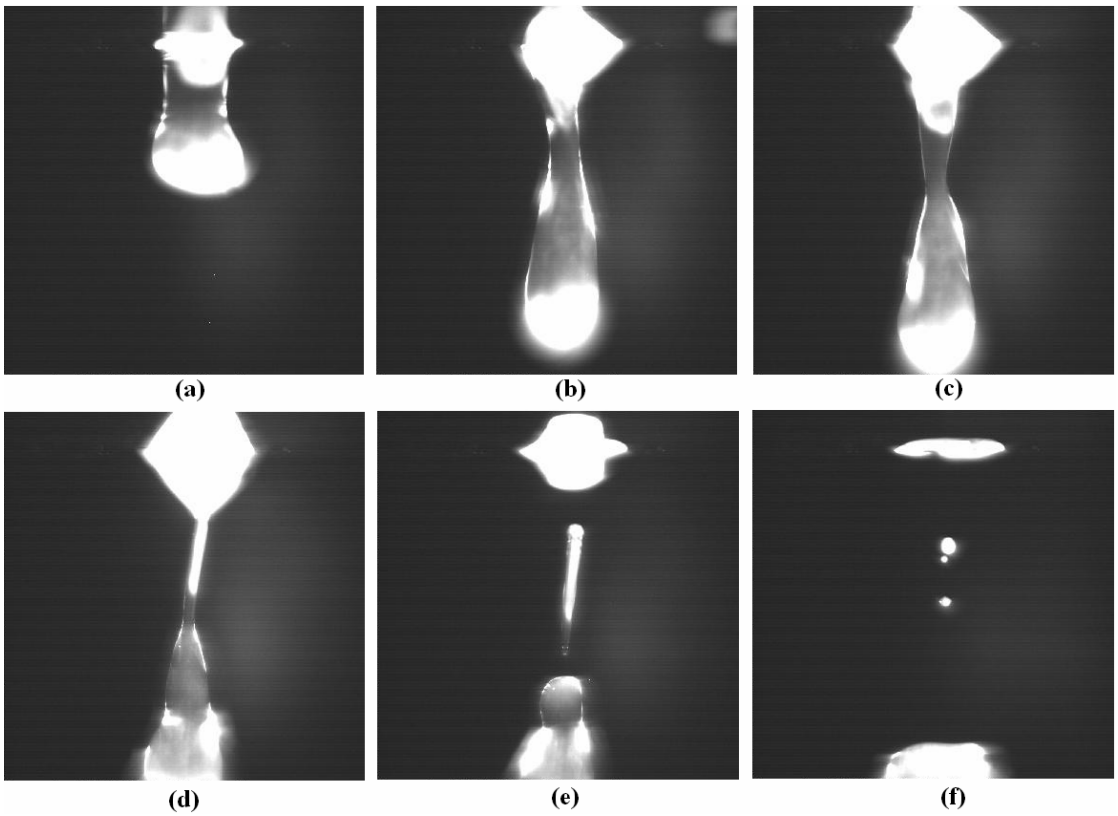


Figure 6.12
Satellite droplets due to waveform B
(a) drop emerges from nozzle (b) liquid thread forms (c) necking occurs
(d) liquid thread before break-off (e) immediately after break-off (f) satellite droplets

With waveform B, the same kind of double necking is observed. However, the end result is different because the meniscus is already beginning to withdraw back into the droplet generator while break-off is beginning to occur. Because the meniscus is pulling upwards towards the nozzle, the liquid thread becomes extremely thin, as in

panel (d). Therefore, when the necks of the thread finally break, the volume of fluid that is separated from the main droplet is much smaller, as seen in panel (f).

This meniscus behavior that has just been discussed is the second major departure from stiff nozzle observations. Specifically, when using waveform A, the meniscus forms a large bead of fluid on the nozzle opening, instead of retracting back into the nozzle. This is shown in Figure 6.13.

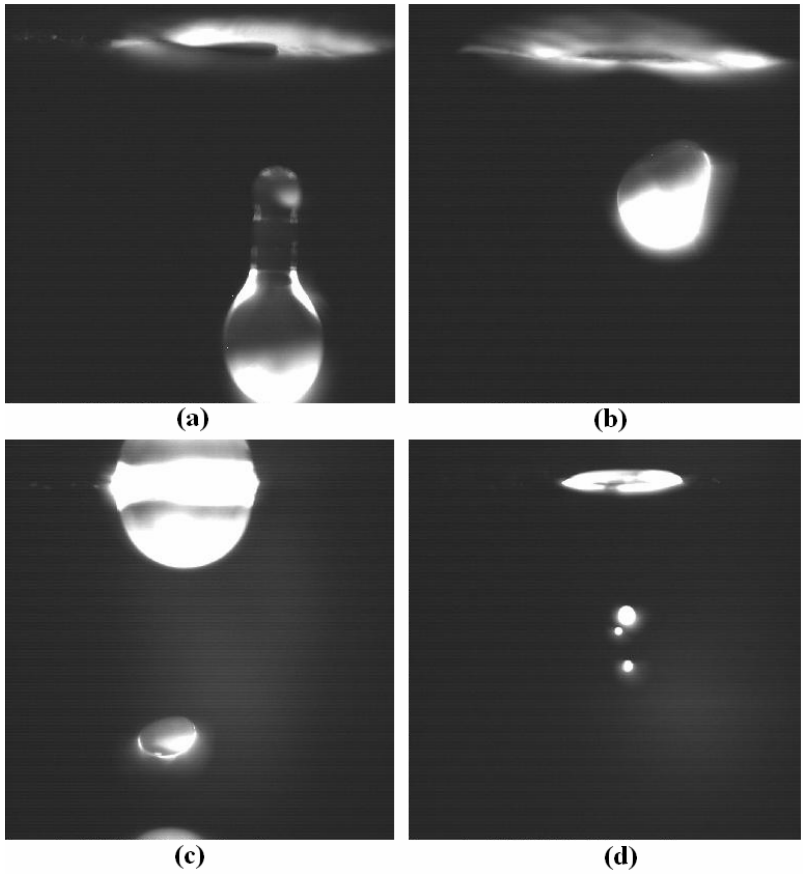


Figure 6.13
Comparison of meniscus behavior after droplet break-off
(a) waveform A, stiff nozzle (b) waveform B, stiff nozzle
(c) waveform A, flexible nozzle (d) waveform B, flexible nozzle

Panel (a) is an image of a droplet after break-off using waveform A with the stiff nozzle. Panel (b) used waveform B with the stiff nozzle. In both cases, the

meniscus has retreated back into the nozzle opening after break-off has occurred. The same can be said for the flexible nozzle when waveform B is used. However, when waveform A is used, the meniscus forms a bead of fluid. This fluid will remain stable at the nozzle surface, until the brass disk is returned back to its original position, at which point the fluid gets sucked back into the droplet generator. This fluid mass is a moving surface during the formation process, and results in a much longer liquid filament prior to break-off. It is this longer liquid thread that appears to be causing the satellite droplets to form during break-off.

Another factor in the formation of satellite droplets in the flexible nozzle case is an increase in the exit velocity of the droplet at the nozzle exit. This is illustrated in Figure 6.14, which shows the velocity versus time when waveform A was used.

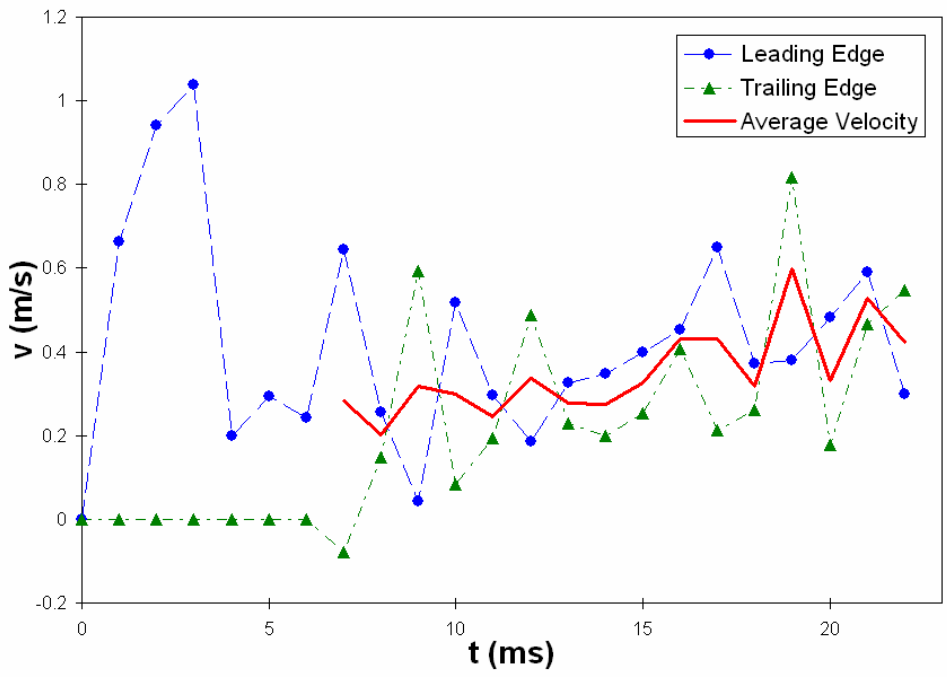


Figure 6.14
Droplet velocity using waveform A, flexible nozzle

When first exiting the nozzle, the droplet velocity was observed to be greater than 1 m/s. Then, as the point of break-off is approached, the liquid thread slows the drop down. Break-off occured 40 ms after the piezoelectric element is activated, or 7 ms after the drop begins to emerge from the nozzle. After break-off, the droplet exhibits the pulsing behavior as a result of the liquid thread merging with the main droplet body, with a period of approximately 3 ms.

Similar behavior is observed when using waveform B. The velocity behavior in this case is shown in Figure 6.15.

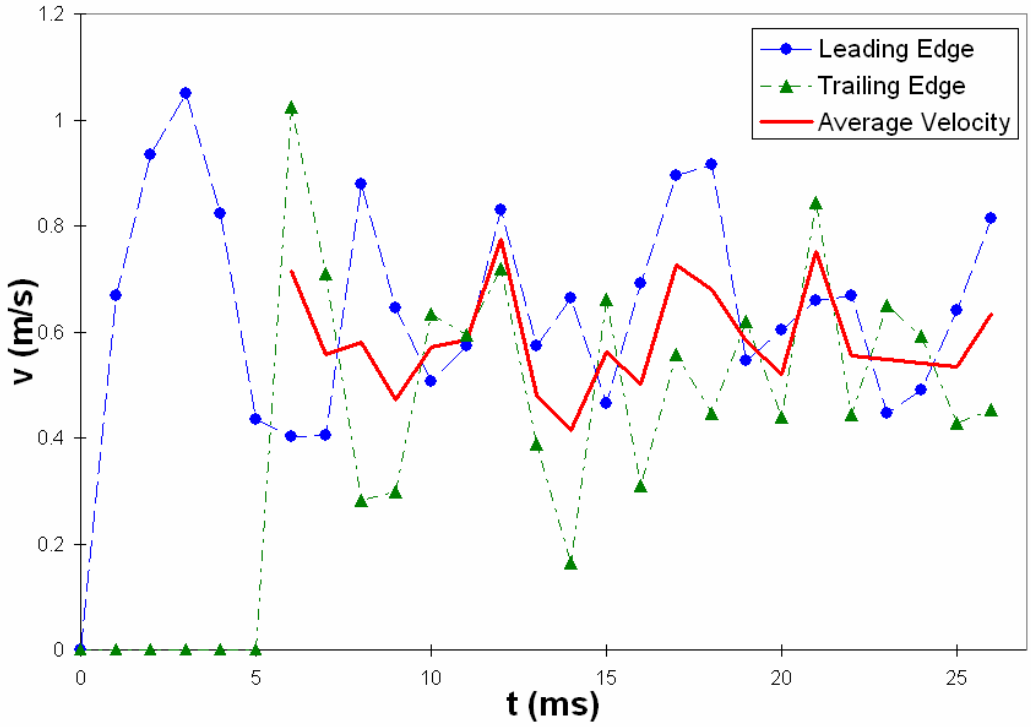


Figure 6.15
Droplet velocity using waveform B, flexible nozzle

Waveform B results are very similar to the waveform A case. The exit velocity exceeds 1 m/s before slowing down prior to break-off. And, the pulsing

behavior is still observed after break-off, although the period of this pulsing is not as easy to detect. However, there are two differences worth noting. First, break-off occurs 1 ms earlier when the pulse is used, so that the drop breaks off 6 ms (+/- 0.25 ms) after it begins to emerge from the nozzle. Second, with the 5 ms pulse waveform, the leading edge velocity routinely reaches 0.8 m/s after break-off, as opposed to 0.6 m/s in the case of the square wave. The average velocities are much greater for waveform B.

The larger velocities observed with waveform B result in the droplets traveling farther than waveform A droplets in the same period of time. This is illustrated in Figure 6.16. But because the droplet velocity behaviors are similar, the shapes of the leading edge position plots are also similar. The pulsing behavior is also reflected in the plot by the slight changes in slope of the lines.

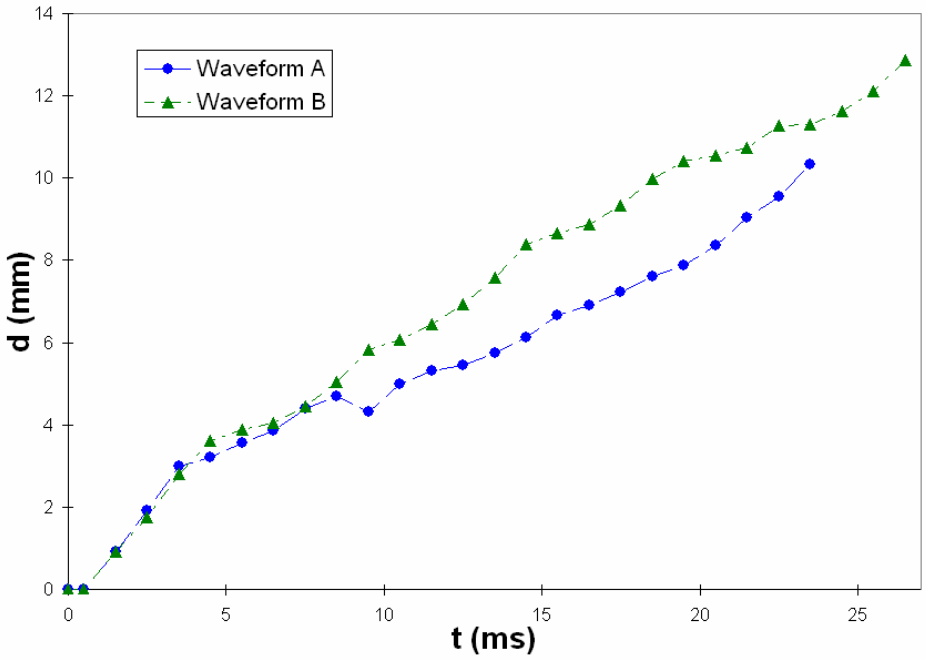


Figure 6.16
Position of the leading edge for both waveforms, flexible nozzle

Figure 6.17 shows the comparison between the leading edge velocities of waveform A and waveform B drops. The exit velocities are nearly identical at the initial formation stage, before finally exhibiting different behavior as the meniscus behavior is altered due to the difference in the brass disk displacement. Overall, the waveform B velocities are larger than the waveform A velocities, confirming the conclusions drawn from the leading edge position plot seen in Figure 6.16.

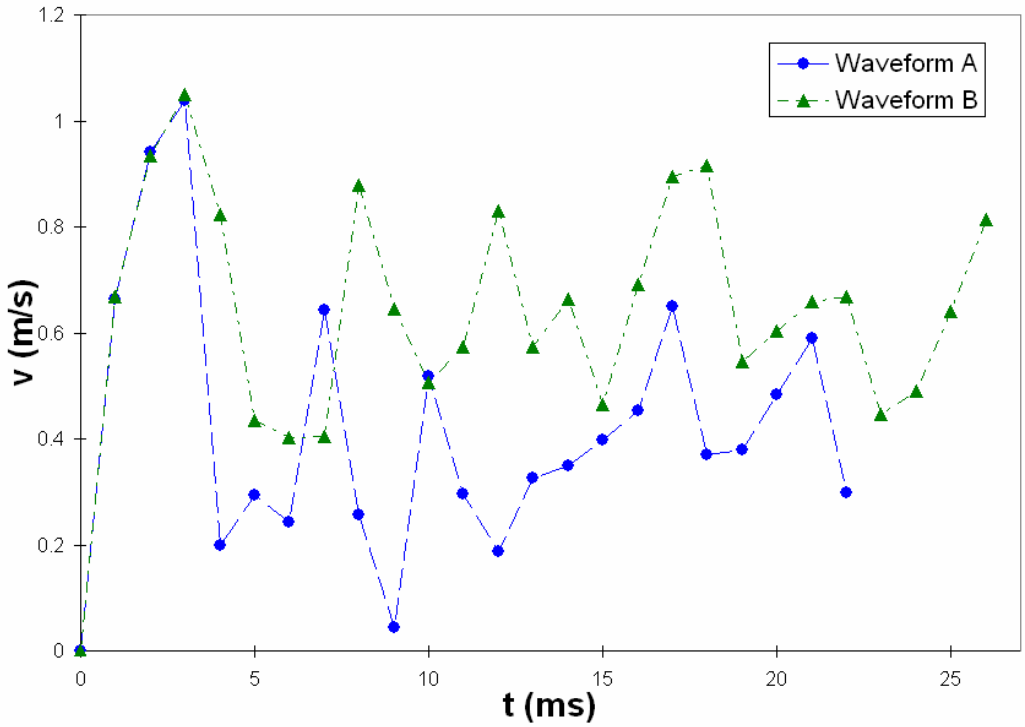


Figure 6.17
Comparison of leading edge velocities versus time for both waveforms, flexible nozzle

Unlike the stiff nozzle, there was no significant difference in the droplet behavior based on the waveform being used when using a flexible nozzle. Although the velocities were slightly different, the general trend was the same in each case.

### *6.2.2 Droplet Impingement Results*

The spread rate U and contact angle $\theta_c$ are once again the focus of this section. To be consistent between the two cases, waveform A was used to produce the droplets and the impingement surface was 4.22 cm below the nozzle exit. However, due to the increased exit velocities of the droplets when a flexible nozzle was used, the conditions immediately before impingement were different. In this case, the droplet velocity $V_o$ was 1.04 m/s, nearly 33% larger than the stiff nozzle case. The average droplet diameter $D_o$ was 1.16 mm, compared to the 1.13 mm during the stiff nozzle trials. Even though these conditions before impingement occur are different, the general spreading behavior of the droplet remains the same. So, Figure 6.8 is still a valid picture of what is happening to the drop during the flexible nozzle trials.

Figure 6.18 shows the normalized spread rate plotted against the normalized spread droplet diameter.

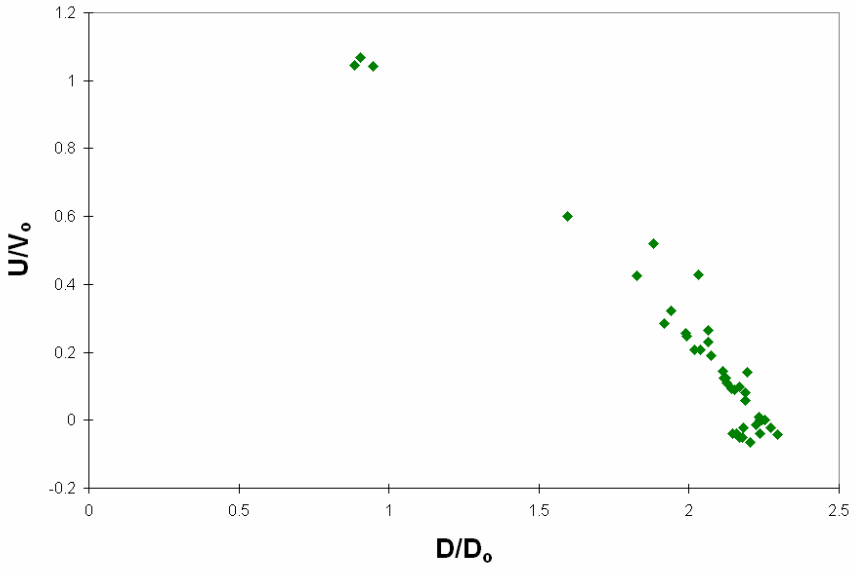


Figure 6.18
Spread rate of an impinging drop, flexible nozzle

Once again, a nearly linear trend is observed. The spread rate continues to decrease as the droplet nears its maximum spread, and then goes slightly negative as the rebound effect takes place. A linear fit was applied to the data for which $U/V_o > 0$, which resulted in the following equation with an $R^2$ value of 0.956.

$$\frac{U}{V_o} = -0.78\frac{D}{D_o} + 1.80 \qquad (15)$$

When looking at the contact angle, the same approach was used as in the stiff nozzle case. A sample of data points were taken to get a sense of the general behavior during impingement. These results are shown in Fig. 6.19.

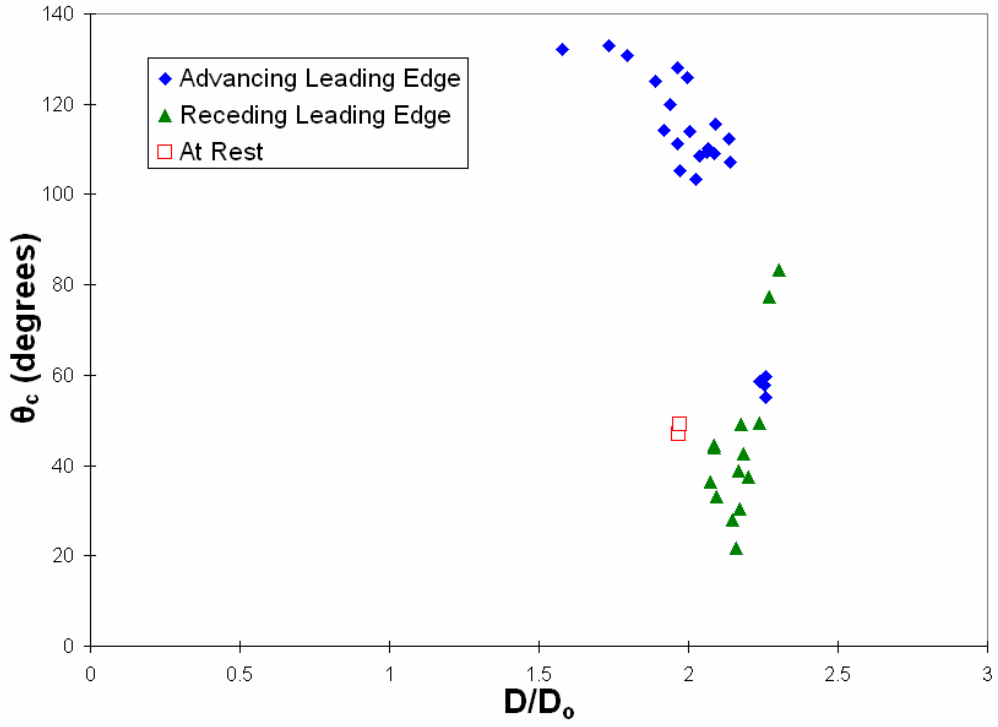


Figure 6.19
Contact angle versus droplet diameter, flexible nozzle

This set of data points is much more vertical than the stiff nozzle case. Large contact angles are more frequent in the flexible nozzle data set, due to the larger droplet velocity immediately before impingement. It appears that the rebound effect is not as effective at drawing back the fluid in contact with the glass surface, as the difference between the maximum $D/D_o$ value and the value when the drop has reached its equilibrium shape is much smaller than the stiff nozzle case.

## *6.3 Stiff Nozzle vs. Flexible Nozzle Comparison*

The section compares the previously discussed droplet formation and impingement data for both the stiff nozzle and flexible nozzle cases. However, since it would be redundant to display the same observed data again, the data in this section is non-dimensionalized. A summary of the important operating characteristics for each case is also provided. And finally, images from each nozzle case are provided to visually compare the different characteristics of the droplet formation process. It should be noted that not every image from the droplet formation process is included in the main body of this report. So for the sake of completeness, a representative image from each time step has been included in Appendix C.

### *6.3.1 Droplet Formation Comparisons*

Table 5.1, lists all of the major quantitative conditions for both nozzle and waveform cases. The general changes in behavior become apparent when looking at this table. The flexible nozzle resulted in higher velocities, both at the nozzle exit and at the impingement surface. The higher exit velocities contributed to shorter break-off

times. In addition, the volume of the droplets were slightly greater in the flexible nozzle cases, even after the formation of satellite droplets, due to the larger amount of fluid being forced through the nozzle opening.

Table 6.1
Droplet Formation Summary

| | **Stiff Waveform A** | **Stiff Waveform B** | **Flexible Waveform A** | **Flexible Waveform B** |
|---|---|---|---|---|
| **Max. Exit Velocity $V_e$ (m/s)** | 0.53 | 0.40 | 1.04 | 1.05 |
| **Impingement Velocity $V_o$ (m/s)** | 0.79 | N/A | 1.04 | N/A |
| **Reynolds Number Re** | 61 | N/A | 83.2 | N/A |
| **Weber Number We** | 9.6 | N/A | 17.1 | N/A |
| **Break-off Time $t_b$ (ms)** | 11 | 9 | 7 | 6 |
| **Average Diameter $D_{av}$ (mm)** | 1.13 | 1.07 | 1.16 | 1.10 |
| **Average Volume $V_{av}$ ($mm^3$)** | 0.76 | 0.63 | 0.82 | 0.70 |
| **Satellite Droplets?** | No | No | Yes | Yes |

Figure 6.20 is a comparison of the four different cases this study looked at and clearly shows how the different nozzles affect the formation process.. The images are each taken at the same time in the droplet formation process at t = 7 ms. Panel (a) is a droplet produced using the square wave and a stiff nozzle. Panel (c) is a droplet

produced using the 5 ms pulse and a stiff nozzle. In both cases at this time step, the droplet is not close to breaking off from the nozzle. The liquid thread has barely begun to neck at this point. Now compare these images to their flexible nozzle counterparts – the square wave droplet in panel (b) and the pulse droplet in panel (d). In these images, the droplets have already broken off from the nozzle, and are nearly out of the frame. These earlier break-off times and larger velocities (since the leading edges are farther away from the nozzle in the flexible nozzle cases) are the results of switching from the stiff nozzle to the flexible nozzle.

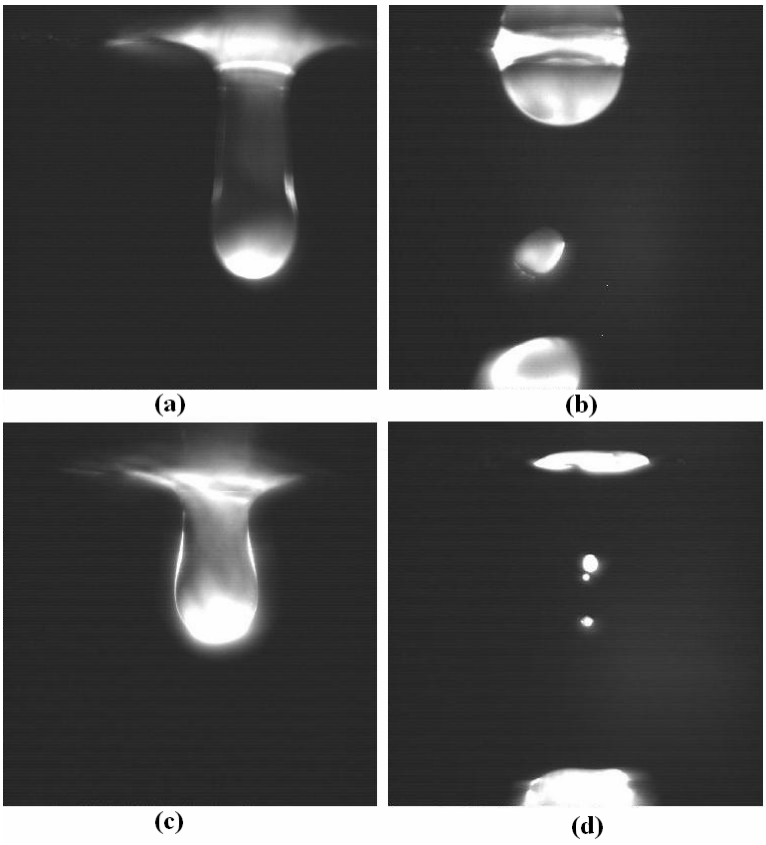


Figure 6.20
Nozzle performance comparison, t = 7 ms
(a) waveform A, stiff nozzle (b) waveform A, flexible nozzle
(c) waveform B, stiff nozzle (d) waveform B, flexible nozzle

Figures 6.21 and 6.22 compare the position of the leading edges for droplets produced by waveform A and waveform B respectively. These plots reinforce the observations seen in Figure 6.20 – that for a specific time after break-off, the distance of the leading edge of a droplet is much greater for the flexible nozzle case. This is particularly evident for the waveform B plot, where a flexible nozzle droplet covers more than three times the distance of a stiff nozzle droplet in the same time interval. In these plots, the time axis has been non-dimensionalized with the capillary time $t_c$, which is defined as $\mu D/\sigma$. This capillary time comes from the capillary number, Ca, which is given as

$$Ca = \frac{\mu V}{\sigma} \tag{16}$$

The capillary number describes the ratio between the viscous forces and surface tension forces in a droplet. V is the characteristic velocity, which can also be described as $D_c/t$ where $D_c$ is the characteristic length of a droplet. Both of these versions are used during this project to non-dimensionalize the data used to compare the stiff nozzle case to the flexible nozzle case.

The position data has been non-dimensionalized with the nozzle diameter $d_{nozzle}$ so that the position of the leading edge d is now displayed as the number of nozzle diameters away from the nozzle plate. However, in this case the nozzle diameter happened to be 1 mm, so the y-axis has effectively not changed from the raw, dimensional data.

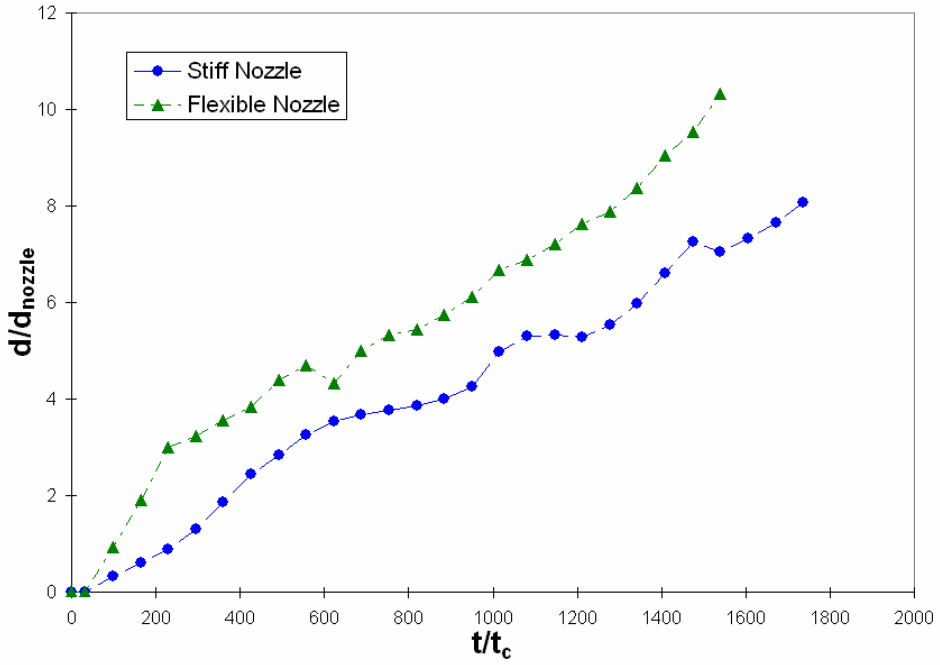


Figure 6.21
Leading edge position comparison for waveform A

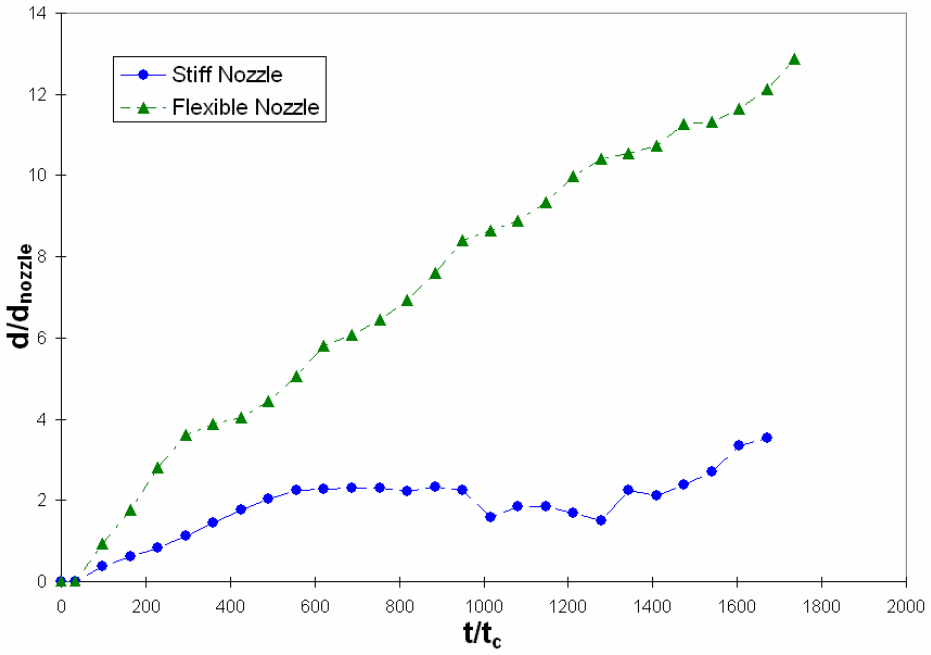


Figure 6.22
Leading edge position comparison for waveform B

Comparing the velocity plots for the different nozzles reinforces the conclusions drawn from the leading edge position plots and provides some insight into why the different behavior at the nozzle exit occurs. Figure 6.23 shows the significant differences in leading and trailing edge velocities for droplets produced by waveform A. The velocity of the droplets has been non-dimensionalized with $V_c = \sigma/\mu$ which has units of m/s and is the ratio found in the expression for the capillary number.

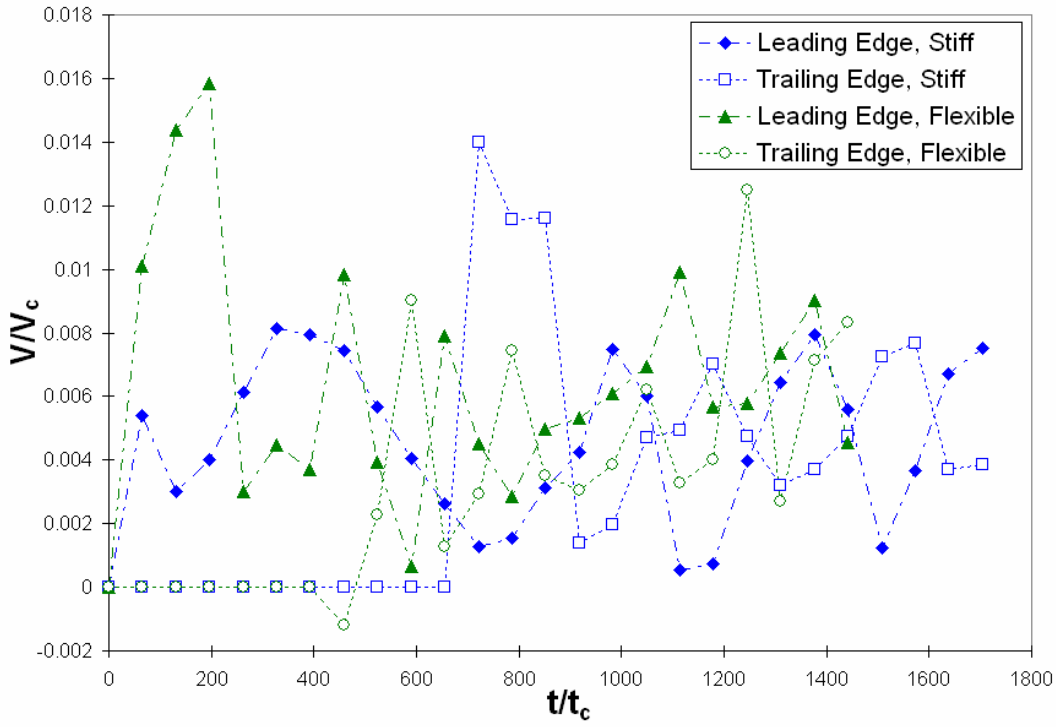


Figure 6.23
Velocity comparison for waveform A

The most obvious difference from looking at the plot is that the $V/V_c$ ratio of a droplet is more than twice as large for the flexible nozzle. It is also clear from the plot that the flexible nozzle droplets have an earlier break-off time than the stiff nozzle case (4 ms earlier) – a direct result of the larger exit velocity. Finally, the average

velocity is larger for the flexible nozzle case, as the flexible nozzle data are nearly always above the stiff case. This is supported by the impingement velocities, where the flexible nozzle resulted in a velocity 33% larger than the stiff nozzle.

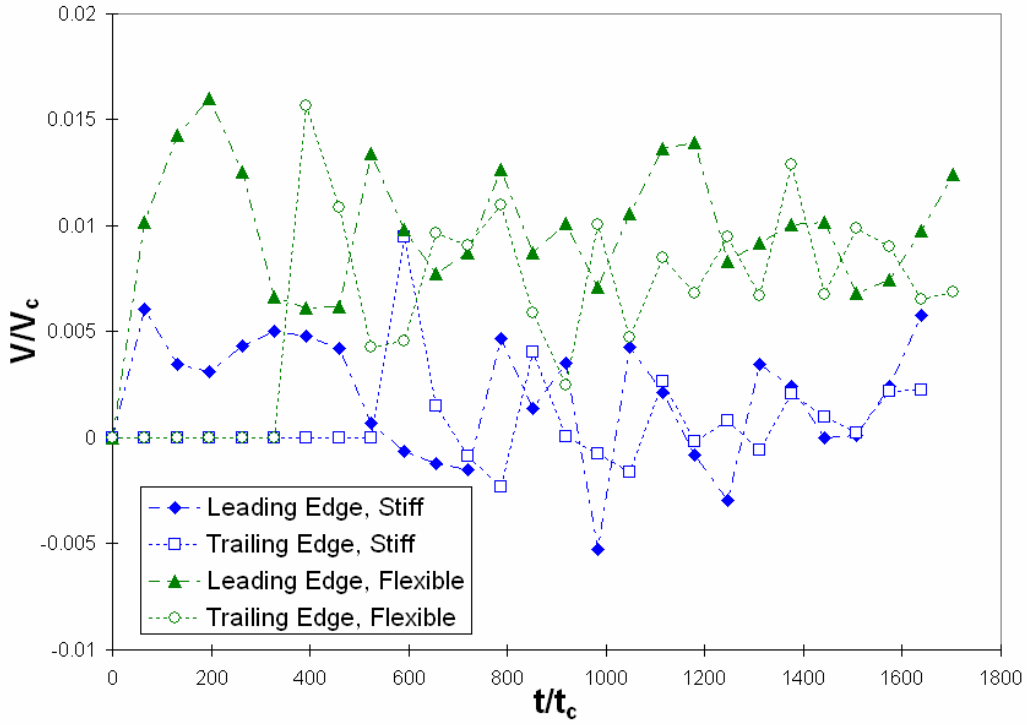


Figure 6.24
Velocity comparison for waveform B

Figure 6.24 compares the leading and trailing edge velocities when waveform B, the 5 ms pulse, is used to produce droplets, with the same non-dimensionalization as in Figure 6.23. The same trends are present in this plot as in the square wave plot. The exit velocity of the droplets is much higher in the case of the flexible nozzle, and break-off time occurs earlier as well (3 ms earlier in this case). In addition, there is a wide gap between the two velocities away from the nozzle surface. This is because droplets produced with a stiff nozzle were thrown back towards the nozzle before

falling back down, as has been previously discussed. This is evident by the negative velocities that are present. The increased exit velocity, and therefore increased momentum, is likely the reason the flexible nozzle droplets were able to break-off from the nozzle without being drawn back upwards.

Since the flexible nozzle droplets have such a high exit velocity, they are able to break free of the nozzle sooner and achieve higher velocities away from the nozzle. This is offset by the fact that satellite droplets form in the flexible nozzle cases. However, when using the droplet generator for the impingement applications under consideration in this paper, these satellite droplets rarely matter since they are thrown away from the main drop and are out of the frame by the time impingement actually occurs (however, these satellite droplets would definitely matter if inkjet printing was being studied). Therefore, it is recommended that for any future impingement studies using this droplet generator, the flexible nozzle should be used instead of the stiff nozzle.

### *6.3.2 Droplet Impingement Comparisons*

Recall that the velocity immediately before impingement was 0.79 m/s for the stiff nozzle case and 1.04 m/s for the flexible nozzle case. The diameters were roughly the same, with the stiff nozzle droplets having an average diameter of 1.13 mm and the flexible nozzle droplets having an average diameter of 1.16 mm. Due to the significant difference in velocities, it is expected that the spread rates for the two cases would be different. Figure 6.25 shows that this is the case.

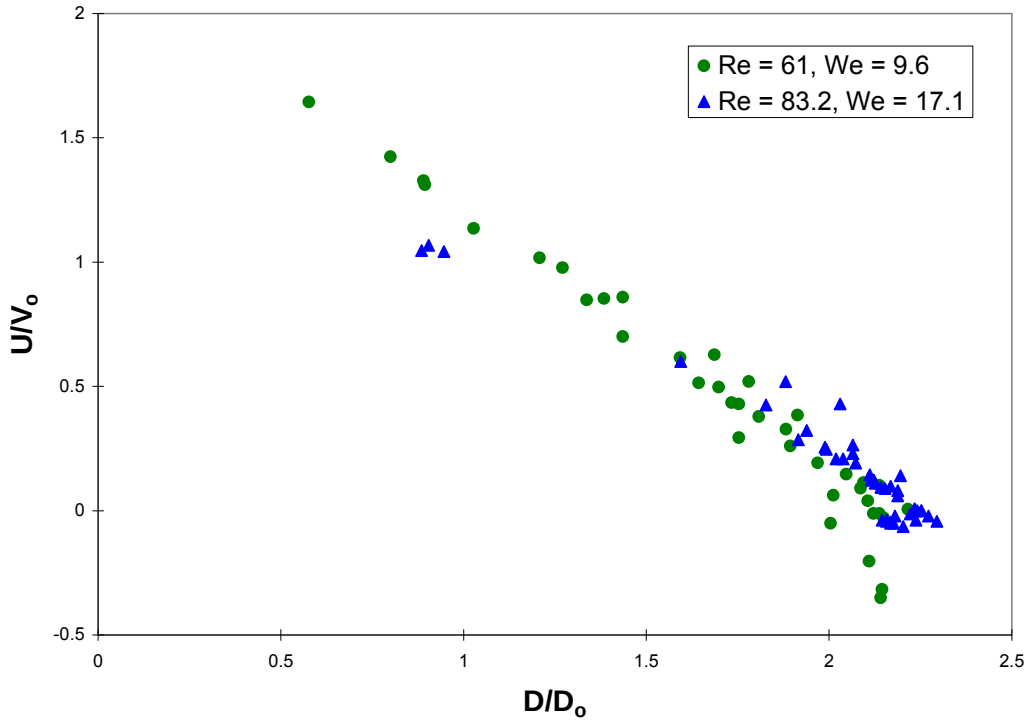


Figure 6.25
Spread rate comparison

In the previous sections, linear fits were applied to these data sets. It was shown that the slope for the flexible nozzle linear fit was -0.78, while for the stiff nozzle case the linear fit had a slope of -1.02. This indicates as the drop spreads out on the impingement surface, the spread rate decelerates more for the stiff nozzle cases. This is because the impinging velocity is less for the stiff nozzle case. However, in both cases the rebound effect was observed, which results in the negative $U/V_o$ ratios near the maximum spread diameter of the droplets. This rebound effect was less noticeable in the case of the flexible nozzle.

Finally, different contact angle behavior was also observed between the two impingement cases. One difference between Figures 6.10 and 6.19 is that the static

contact angle for a droplet at rest is different. This is illustrated in Figure 6.26. Frame (a) shows a drop at rest for the stiff nozzle case, while frame (b) is a drop at rest for the flexible nozzle case.

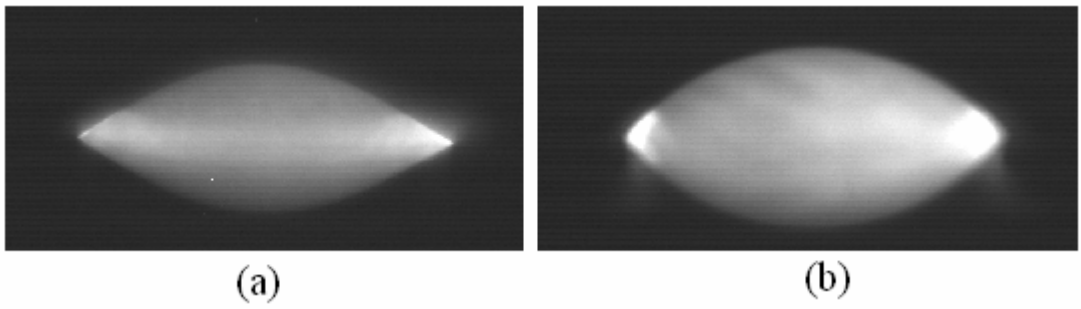


Figure 6.26
Static contact angle comparison
(a) Stiff nozzle case (b) Flexible nozzle case

The flexible nozzle image depicts a larger static contact angle, which corresponds to the results of Figure 6.19. This could be due to the larger volume of fluid impinging onto the surface in the flexible nozzle case, as well as the larger impingement velocity.

Figures 6.27 and 6.28 are plots containing both sets of contact angle data. Since the spread velocity requires two images 0.5 ms apart, there are two distinct contact angles associated with each spread velocity. Therefore, two plots were created.

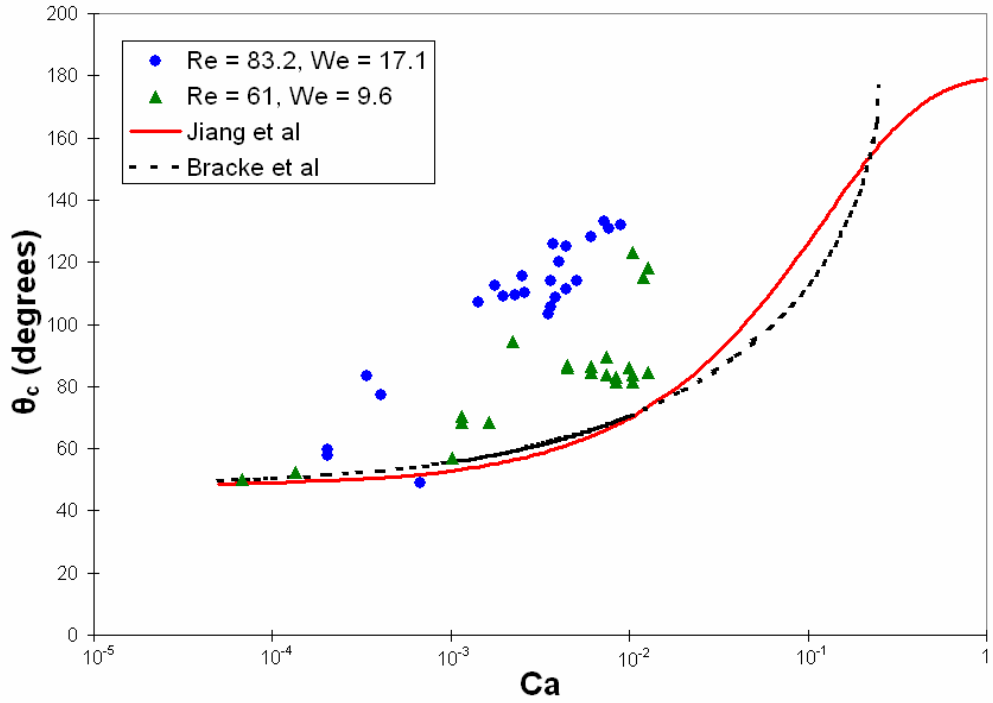


Figure 6.27
Contact angle comparison using frame 1

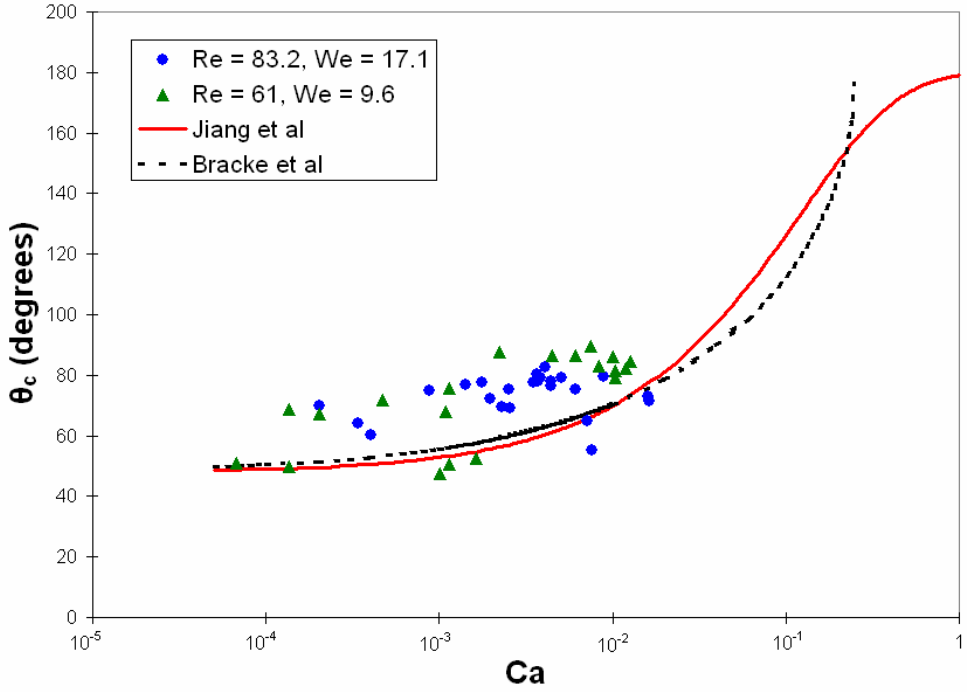


Figure 6.28
Contact angle comparison using frame 2

Figure 6.27 contains the contact angles from the first frame of the image. Figure 6.28 contains information from the second frame. Unlike the previous plots, the x-axis has a logarithmic scale where the capillary number is calculated using the spread velocity. This is the standard format for plotting dynamic contact angles, and allows the results of this experiment to be compared to previous models that have been derived from experimental data. Two of the models are shown in Fig. 26 and 27. The solid line is the model provided by Jiang *et al*. [30], and is given as

$$\theta_c = \cos^{-1}\left[\cos\theta_o - \left(1+\cos\theta_o\right)\tanh\left(4.69Ca^{0.702}\right)\right] \qquad (17)$$

The dashed line is provided by Bracke *et al.* [31], and is given as

$$\theta_c = \cos^{-1}\left[\cos\theta_o - 2\left(1+\cos\theta_o\right)Ca^{0.5}\right] \qquad (18)$$

Although the forward-difference approach in Fig. 6.28 agrees closely with the models, and a time-weighted average would favor this second frame approach since the velocity is slowing down, it is not fair to ignore frame 1 and base an analysis solely on Fig. 6.28. Since instantaneous velocities were not able to be measured so that a velocity measurement is only associated with one contact angle measurement, Fig. 6.29 shows the averaged dynamic contact angle between frame 1 and frame 2. It should be noted that if it was not possible to determine the contact angle in one of the frames, then both the frame 1 and frame 2 points were omitted from the averaged plot. However, this was a rare occurrence.

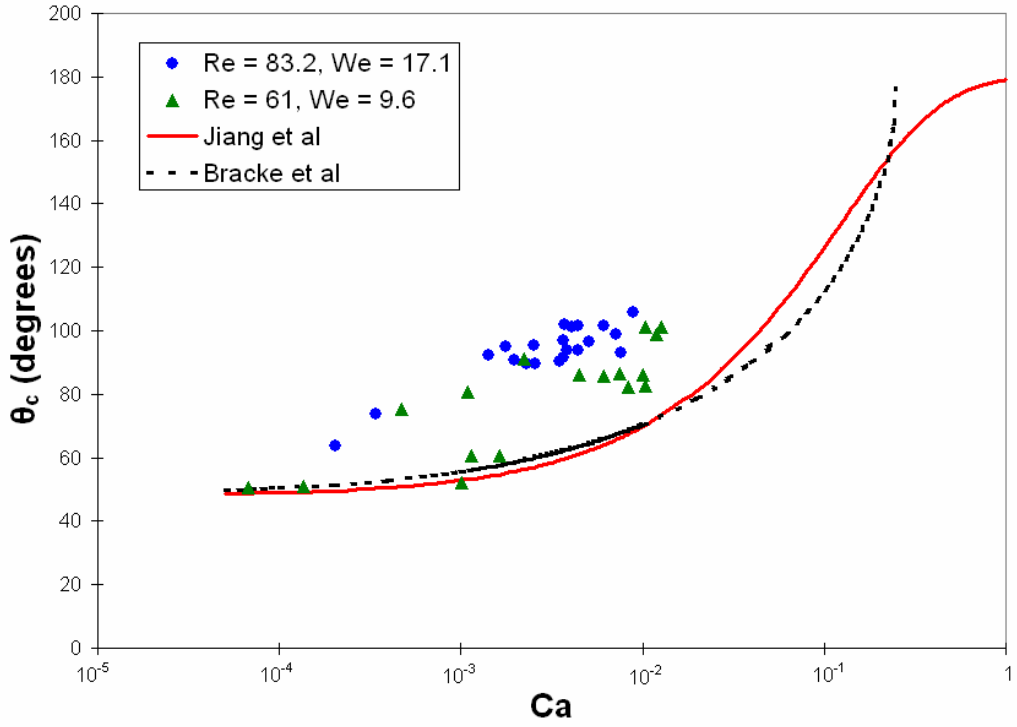


Figure 6.29
Averaged contact angle comparison

It appears that the stiff nozzle impingement results (lower Reynolds and Weber numbers) follow the general trend of the Jiang and Bracke models. The data points below $\theta_c = 60^o$ match closely with the Bracke model. Although the data begins to curve upward sooner than the models, the shape of the Bracke model appears to be preserved. Unfortunately, the contact angle data for the flexible nozzle case (the larger Reynolds and Weber numbers) does not appear to follow either model, and even differs from the stiff nozzle case. The impingement conditions were the same in both cases, so the difference must be due to the increased impingement velocity and larger droplet diameter. The data indicates that for a given spread rate (measured at the liquid-solid interface), the contact angle is larger for the flexible case. Intuitively, this makes sense. Due to viscous forces, the liquid near the upper surface of the drop will

move much faster than the liquid near the impingement surface, which is slowed due to friction. So if the liquid near the surface is slowed to the same speed in each case, then the droplet with the higher impact velocity will result in farther spread of the upper surface of the drop. This increased spread will result in larger contact angles.

It should be noted that the deviation of the experimental data from the Jiang and Bracke models should not be unexpected. In the paper by Jiang *et al.*, specifically states that the provided equation "may be applicable to any macroscopic geometry so long as the effects of gravity, of inertia, and of adsorption all appear to be absent." [30] This is not the case with this experiment, where the Weber numbers – the ratio of inertial to viscous forces – were 9.6 and 17.1 immediately before impingement. When Jian *et al*. compared their model to experimental data, the Weber numbers were less than $10^{-3}$. Since inertial forces cannot be neglected in the current experiment, deviation from the model comes as no surprise. This explanation is also supported by the fact that the receding contact angles (less than 90 degrees) more closely match the models than the advancing contact angles, since the droplet has slowed significantly by this point and inertial forces are not as dominant.

Deviation from the Bracke model is also not surprising. The model was initially developed by observing the dynamic contact angle as a solid strip was drawn through a liquid pool. After the model was derived, it was then compared to published impingement data. The model loosely agreed with the experimental observations. However, the experimental conditions under consideration were the spreading of molten glass droplets at $1000^{o}$C, and polyethylene drops on alumina and teflon

surfaces – not water droplets onto a glass surface at room temperature. Because of the droplet material property and temperature differences in the first case, and the impingement surface wettability differences in the second case, the dynamic contact angle results from this research should not match exactly.

Overall, it appears that as the Weber number increases, the contact angle plots shift upward – although this is not certain since only two experimental cases were plotted. This is due to the increasing influence of inertial forces that result from the increased velocity. However, eventually this trend will cease as splashing will occur when the Weber number becomes large enough. When splashing occurs, there is no longer a stable liquid-solid interface at the impingement surface, and contact angles are no longer valid.

# 7. CONCLUSIONS AND RECOMMENDATIONS

The goal of this study was to investigate what effects occur when replacing a thick, stiff nozzle with a thin, flexible nozzle has on droplets during the formation process and during impingement. It was discovered that changing the nozzle characteristics has a significant effect on both the velocity of droplets during the formation process, and on their general behavior as well.

Switching from a stiff nozzle to a flexible nozzle resulted in far greater exit velocities in the latter case. The increased exit velocities resulted in break-off times several milliseconds sooner than their stiff nozzle counterparts. They also caused the flexible nozzle droplets to have a larger average velocity throughout the path of the droplet – from the vicinity of the nozzle, all the way to the impingement surface.

In the case of waveform B, the increased exit velocity permitted the droplets to break off from the nozzle without being thrown back upwards by the retracting meniscus. Because of this, the quality and repeatability of the droplets were improved in the flexible nozzle case. The droplets were able to travel straight, instead of being given a horizontal velocity immediately after break-off.

The volumes of the droplets were roughly the same between the stiff and flexible nozzle cases, with the flexible nozzle drops being slightly larger. However, it appears that overall, much more liquid is ejected from the fluid reservoir when a flexible nozzle is used. But because of the large fluid meniscus that beads up at the nozzle surface, and because of the formation of satellite droplets (a drawback to using a flexible nozzle), the volumes are approximately even.

Finally, the spread rate and contact angles of the droplets were observed after the drops impinged on a flat glass surface. It was observed that the spread rate and advancing contact angles were larger for the droplets produced with a flexible nozzle, while there was no change when looking at receding contact angles. However, this is not due to the flexible nozzle directly, but rather the difference in impingement velocities. If a second stiff nozzle had produced droplets at the same velocity as the flexible nozzle used in this research, the comparison results would likely be the same.

The numerical study by Yang and Liburdy [12] discussed in the literature review was similar in nature to this experimental research. The results from that study indicate that when compared to a stiff nozzle, a flexible nozzle should affect droplet shape and satellite formation, and have much less influence over droplet size and break-off time. The experimental results from this research support these observations. The droplet shape and general formation behavior were much different in the flexible nozzle case, and one or more satellite droplets were formed, whereas none were observed in the stiff nozzle case. Although there was a 2-3 ms difference in break-off times between the two cases, there was only a 3% increase in the droplet diameter.

If future work is done on this project, there are three areas of interest that are recommended for research. Clearly, there are significant changes in the droplet formation process for the two nozzle cases. There are two potential reasons for this. One is that the flexible nozzle will flex more than a stiff nozzle. The second reason is that the flexible nozzle is much thinner than the stiff nozzle, meaning that the nozzle orifice is not as deep, so the total amount of surface area the fluid comes into contact

with as it is ejected from the nozzle is reduced. It would be worthwhile to conduct further experiments to see how much change in droplet behavior is due to flexing, and how much is due the difference in nozzle thicknesses.

Also, it is recommended to observe droplet impingement over a larger range of Weber numbers to confirm that the contact angle trends seen in Fig. 26 do shift upwards as the Weber number increases. However, the Weber number cannot be increased too high, or eventually the dominant inertial forces will cause splashing to occur.

And finally, it is recommended that future studies use even thinner and more flexible nozzle plates than the current study. This study served to compare a slightly flexible nozzle to a completely stiff nozzle. Observing droplet behavior changes while using nozzle plates that deflect approximately on the order of the nozzle radius would be a worthwhile extension of this project, as this more closely mimics the operating conditions in applications such as inkjet printing where flexible nozzles may be used.

# BIBLIOGRAPHY

1. Lee, H.C., 1974, "Drop Formation in a Liquid Jet," *IBM Journal of Research and Development*, Vol. 18, No. 4, pp. 364-369.

2. Pimbley, W.T., Lee, H.C., 1977, "Satellite Droplet Formation in a Liquid Jet," *IBM Journal of Research and Development*, Vol. 21, No. 1, pp. 21-30.

3. Zhang, Xiaoguang, 1999, "Dynamics of Drop Formation in Viscous Flows," *Chemical Engineering Science*, Vol. 54, No. 12, pp. 1759-1774.

4. Wilkes, E.D., Basaran, O.A., 2001, "Drop Ejection from an Oscillating Rod," *Journal of Colloid and Interface Science*, Vol. 242, No. 1, pp. 180-201.

5. Meacham, J.M., Varady, M.J., Degertekin, F.L., Fedorov, A.G., 2005, "Droplet Formation and Ejection from a Micromachined Ultrasonic Droplet Generator: Visualization and Scaling," *Physics of Fluids*, Vol. 17, No. 100605.

6. Shield, T.W., Bogy, D.B., Talke, F.E., 1987, "Drop Formation by DOD Ink-Jet Nozzles: A Comparison of Experiment and Numerical Simulation," *IBM Journal of Research and Development*, Vol. 31, No. 1, pp. 96-110.

7. Mutoh, Masayuki, 2002, "A Study on the Drop Formation of Continuous Liquid Jet by an Electrical Method," *Physics of Fluids*, Vol. 14, No. 4, pp. 1380-1388.

8. Lee, C-H., Lal, A., 2004, "Single Microdroplet Ejection Using an Ultrasonic Longitudinal Mode with a PZT/Tapered Glass Capillary," *IEEE Transactions on Ultrasonics, Ferroelectrics, and Frequency Control*, Vol. 51, No. 11, pp. 1514-1522.

9. Ambravaneswaran, B., Wilkes, E.D., Osman, B., 2002, "Drop Formation from a Capillary Tube: Comparison of One-Dimensional and Two-Dimensional Analyses and Occurrence of Satellite Drops," *Physics of Fluids*, Vol. 14, No. 8, pp. 2606-2621.

10. Percin, G., Khuri-Yakub, B., 2003, "Piezoelectric Droplet Ejector for Ink-Jet Printing of Fluids and Solid Particles," *Review of Scientific Instruments*, Vol. 74, No. 2, pp. 1120-1127.

11. Percin, G., Yaralioglu, G., Khuri-Yakub, B., 2002, "Micromachined Droplet Ejector Arrays," *Review of Scientific Instruments*, Vol. 73, No. 12, pp. 4385-4389.

12. Yang, G., Liburdy, J., 2004, "Droplet formation from a pulsed vibrating nozzle," *Proceedings of the ASME Heat Transfer/Fluids Engineering Summer Conference 2004, HT/FED 2004*, Vol. 1, pp. 269-276.

13. Bechtel, S.E., Bogy, D.B., Talke, F.E., 1981, "Impact of a Liquid Drop Against a Flat Surface," *IBM Journal of Research and Development*, Vol. 25, No. 6, pp. 963-971.

14. Park, H., Carr, W., 2003, "Single Drop Impaction on a Solid Surface," *Fluid Mechanics and Transport Phenomena*, Vol. 49, No. 10, pp. 2461-2471.

15. Fedorchenko, A., Wang, A-B., 2004, "The Formation and Dynamics of a Blob on Free and Wall Sheets Induced by a Drop Impact on Surfaces," *Physics of Fluids*, Vol. 16, No. 11, pp. 3911-3920.

16. Kamnis, S., Gu, S., 2005, "Numerical Modelling of Droplet Impingement," *Journal of Physics D: Applied Physics*, Vol. 38, pp. 3664-3673.

17. Sikalo, S., Marengo, M., Tropea, C., Ganic, E.N., 2002, "Analysis of Impact of Droplets on Horizontal Surfaces," *Experimental Thermal and Fluid Science*, Vol. 25, pp. 503-510.

18. Moita, A.S., Moreira, A.L., 2002, "The Dynamic Behavior of Single Droplets Impacting Onto a Flat Surface," *ILASS-Europe*, Zaragoza 9-11 September 2002.

19. Sivakumar, D., Katagiri, K., Sato, T., Nishiyama, H., 2005, "Spreading Behavior of an Impacting Drop on a Structured Rough Surface," *Physics of Fluids*, Vol. 17, No. 100608.

20. Mehdizadeh, N., Chadra, S., Mostaghimi, J., 2004, "Formation of Fingers Around the Edges of a Drop Hitting a Metal Plate with High Velocity," *Journal of Fluid Mechanics*, Vol. 510, pp. 353-373.

21. Thoroddsen, S.T., Sakakibara, J., 1998, "Evolution of the Fingering Pattern of an Impacting Drop," *Physics of Fluids*, Vol. 10, No. 6, pp. 1359-1374.

22. Zable, J.L., 1977, "Splatter During Ink Jet Printing," *IBM Journal of Research and Development*, Vol. 21, No. 4, pp. 315-320.

23. Amada, S., Ohyagi, T., Haruyama, M., 1999, "Evaluation of Splat Profile for Droplet Impingement," *Surface & Coatings Technology*, Vol. 115, pp. 184-192.

24. Fujimoto, H., Ogino, T., Takuda, H., Hatta, N., 2001, "Collision of a Droplet with a Hemispherical Static Droplet on a Solid," *International Journal of Multiphase Flow*, Vol. 27, pp. 1227-1245.

25. Fujimoto, H., Tong, A., Kasliwal, S., Takuda, H., 2004, "A Numerical Study on the Successive Impingement of Droplets onto a Substrate," *Proceedings of IMECE04*, No. IMECE2004-60183.

26. Fujimoto, H., Tong, A., Shiotani, Y., Takuda, H., 2004, "Interaction Phenomena of Two Water Droplets Successively Impacting onto a Solid Surface," *Proceedings of IMECE04*, No. IMECE2004-60815.

27. Timoshenko, Stephen, Theory of Elastic Stability, 2nd ed., McGraw-Hill, 1961.

28. Yang, J.C., Chien, W., King, M., Grosshandler, W. L., 1997, "A Simple Piezoelectric Droplet Generator," *Experiments in Fluids*, Vol. 23, pp. 445-447.

29. Quanta-Ray PIV Series Pulsed Nd:YAG Lasers Product Webpage; http://www.newport.com/store; Accessed October 2006.

30. Jiang, T.S., Oh, S.G., Slattery, J.C., 1979, "Correlation for dynamic contact angle," *Journal of Colloid & Interface Science*, Vol. 69, pp. 74-77.

31. Bracke, M., De Voeght, F., Joos, P., 1989, "The kinetics of wetting: the dynamic contact angle," *Progress in Colloid & Polymer Science*, Vol. 79, pp. 142-149.

# APPENDICES

# APPENDIX A

## Solidworks Drawings of Droplet Generator

The Solidworks drawings of the droplet generator, described in detail in Section 4.1, are provided in this appendix. Drawings are available for every component of the droplet generator with the exception of the American Piezo Ceramics, Inc. unimorph disk bender, which was purchased from an outside vendor.

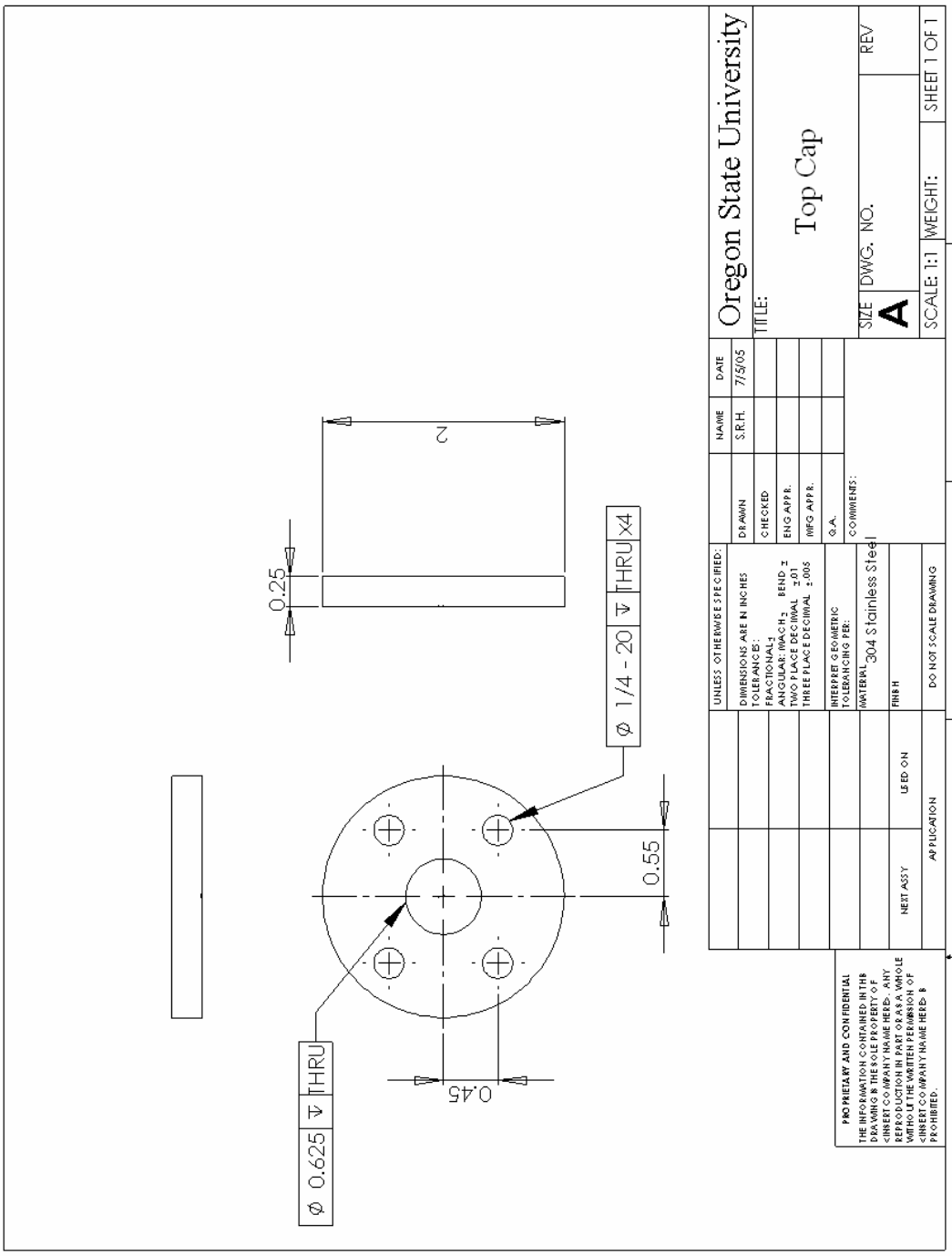


Figure A.1
Top cap SolidWorks drawing

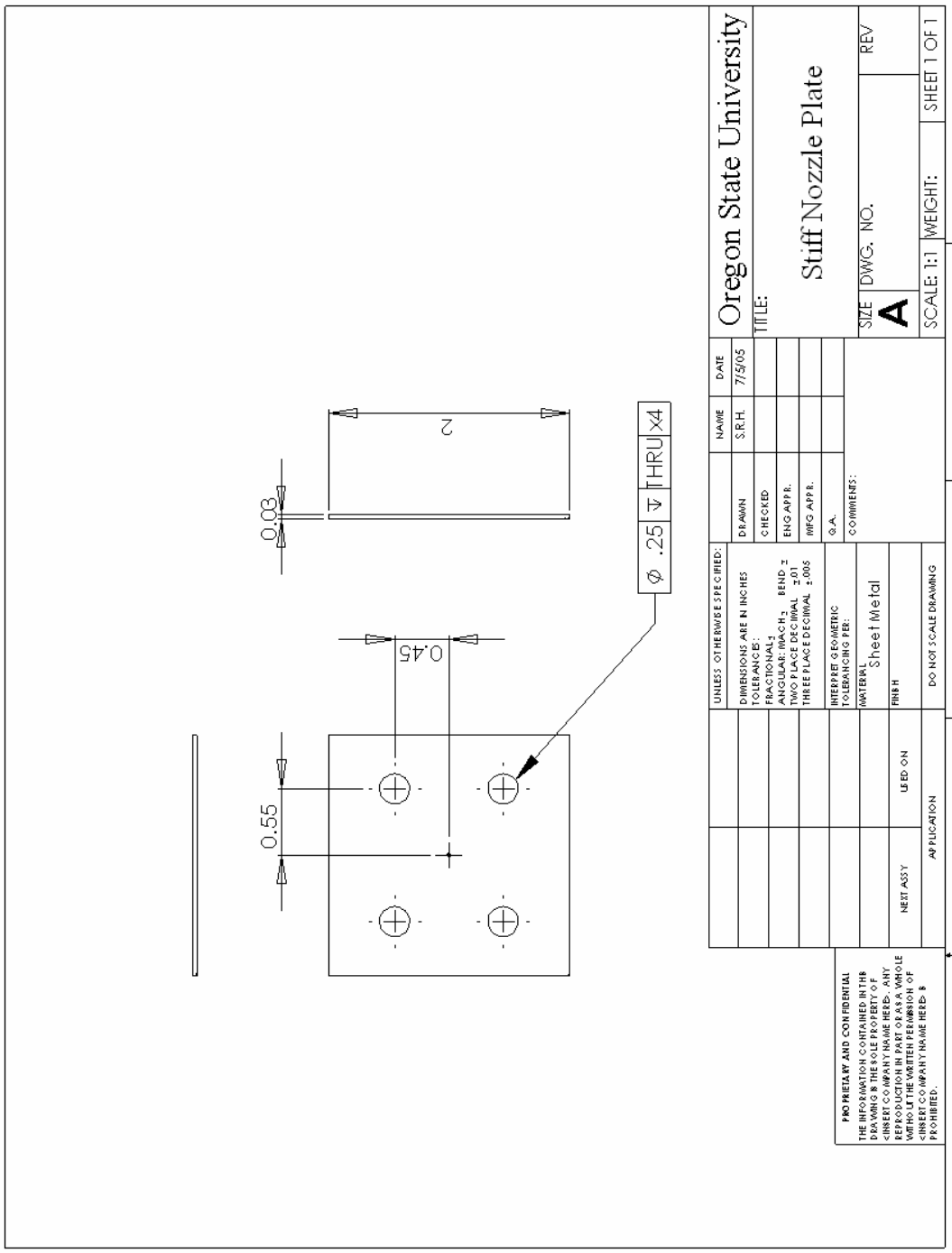


Figure A.2
Nozzle plate SolidWorks drawing

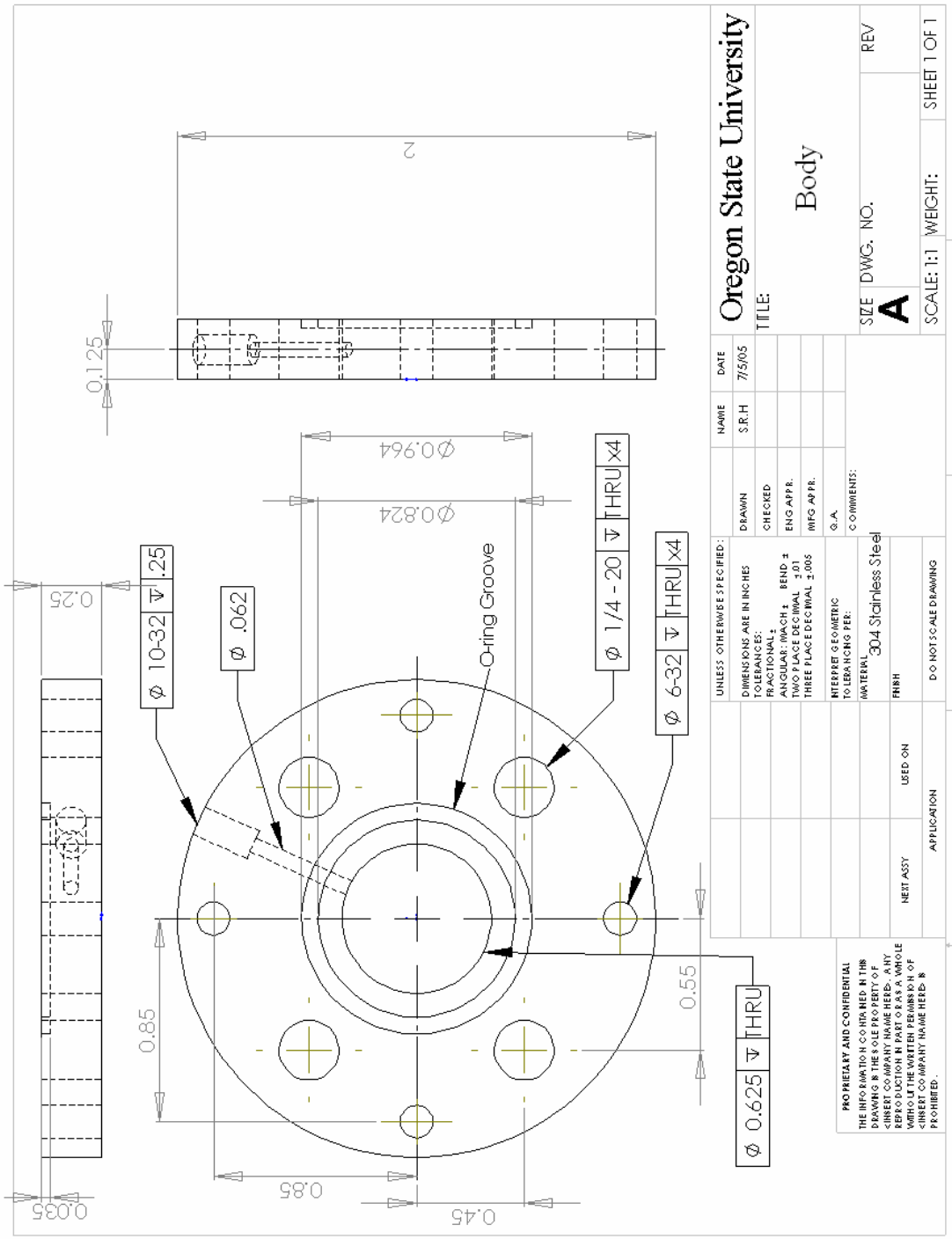


Figure A.3
Droplet generator body SolidWorks drawing

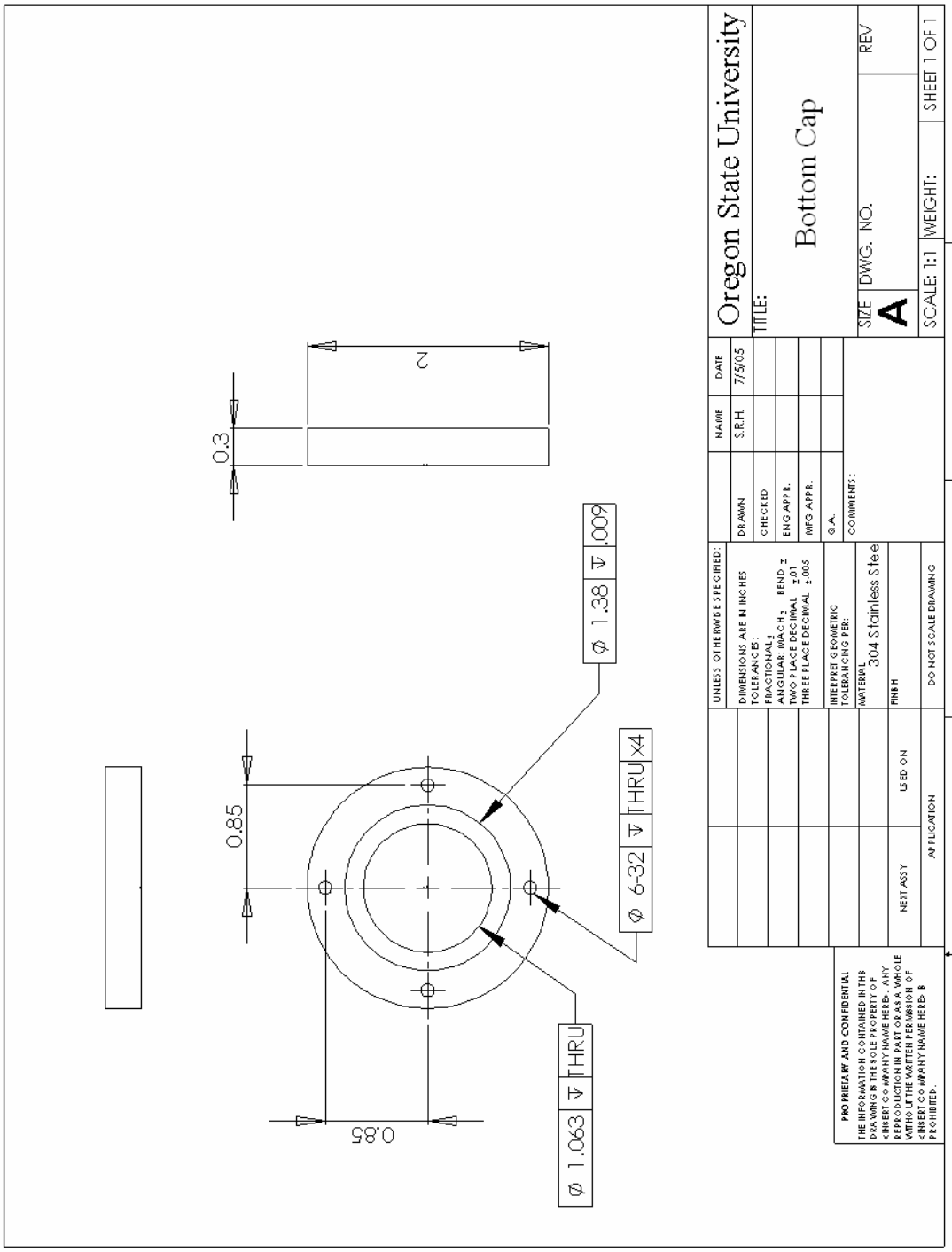


Figure A.4
Bottom cap SolidWorks drawing

# APPENDIX B

## Uncertainty Analysis

This section explains the uncertainty calculations that were used when analyzing the results. Uncertainty was calculated for the droplet velocity and leading edge position measurements, as well as for the spread rate and dynamic contact angle at the impingement surface. The standard deviation of the collected experimental data is also listed, when appropriate.

## *B.1 Experimental Coefficient Uncertainty*

The experimental coefficients $C_f$ and $C_i$ were determined by capturing images of an object of known width ($\Delta l$), and then determining the width in pixels ($\Delta P_{2\text{-}1}$). Therefore, the equation for the experimental coefficient is given as

$$C_f = \frac{\Delta l}{\Delta P_{2-1}} \tag{B1}$$

Therefore, the uncertainty is calculated as

$$u_{C_f} = \sqrt{\left(\frac{\partial C_f}{\partial \Delta l} u_{\Delta l}\right)^2 + \left(\frac{\partial C_f}{\partial \Delta P_{2-1}} u_{\Delta P_{2-1}}\right)^2} \tag{B2}$$

where

$$\frac{\partial C_f}{\partial \Delta l} = \frac{1}{\Delta P_{2-1}} \tag{B3}$$

and

$$\frac{\partial C_f}{\partial \Delta P_{2-1}} = -\frac{\Delta l}{\left(\Delta P_{2-1}\right)^2} \tag{B4}$$

This gives the formation coefficient value as $C_f = 4.31 \times 10^{-6}$ +/- $2 \times 10^{-7}$ m/pixel. At the impingement surface, the coefficient is $C_i = 4.44 \times 10^{-6}$ +/- $1 \times 10^{-7}$ m/pixel.

Although different, these values do overlap when the error range is taken into account. However, slight focus adjustments required to get clear pictures at the impingement surface also contributed to this difference.

## *B.2 Droplet Velocity Uncertainty*

The equation used to determine the velocity of a droplet was given in Section 5 as the following:

$$v = \frac{P1 - P2}{\Delta t} C_f \tag{B5}$$

Combining the two pixel values into one change in pixel term ($\Delta P_{2\text{-}1}$) results in

$$v = \frac{\Delta P_{2-1}}{\Delta t} C_f \tag{B6}$$

The uncertainty for the velocity can now be calculated as

$$u_v = \sqrt{\left( \frac{\partial v}{\partial \Delta P_{2-1}} u_{\Delta P_{2-1}} \right)^2 + \left( \frac{\partial v}{\partial \Delta t} u_{\Delta t} \right)^2 + \left( \frac{\partial v}{\partial C_f} u_{C_f} \right)^2} \tag{B7}$$

where

$$\frac{\partial v}{\partial \Delta P_{2-1}} = \frac{C_f}{\Delta t} \tag{B8}$$

$$\frac{\partial v}{\partial \Delta t} = -\frac{\Delta P_{2-1}}{\Delta t^2} C_f \tag{B9}$$

and

$$\frac{\partial v}{\partial C_f} = \frac{\Delta P_{2-1}}{\Delta t} \tag{B10}$$

The experimental coefficient uncertainty was determined in the previous section. The change in pixel term was assigned an uncertainty of $u_{\Delta P} = 1$ pixel. $u_{\Delta t}$ is assigned a value of $4 \times 10^{-9}$ s, which is half the length of the laser pulse that is used to illuminate the droplets.

The uncertainty and standard deviation values, for both nozzle cases and both waveforms A & B, are listed in the following tables. The maximum, minimum, and average uncertainty values are listed for each case.

Table B.1 Velocity uncertainties – stiff nozzle, waveform A

| t (ms) | $V_{leading}$ (m/s) | StDev (m/s) | $u_v$ (m/s) | $V_{trailing}$ (m/s) | StDev (m/s) | $u_v$ (m/s) |
|---|---|---|---|---|---|---|
| 0 | 0 | 0 | 0 | | | |
| 1 | 0.354 | 0.007 | 0.018 | | | |
| 2 | 0.198 | 0.007 | 0.013 | | | |
| 3 | 0.263 | 0.011 | 0.015 | | | |
| 4 | 0.401 | 0.023 | 0.020 | | | |
| 5 | 0.533 | 0.028 | 0.026 | | | |
| 6 | 0.520 | 0.015 | 0.025 | | | |
| 7 | 0.487 | 0.039 | 0.024 | | | |
| 8 | 0.371 | 0.025 | 0.019 | | | |
| 9 | 0.265 | 0.022 | 0.015 | | | |
| 10 | 0.173 | 0.019 | 0.012 | | | |
| 11 | 0.084 | 0.011 | 0.009 | 0.917 | 0.004 | 0.043 |
| 12 | 0.101 | 0.016 | 0.010 | 0.757 | 0.019 | 0.036 |
| 13 | 0.205 | 0.038 | 0.013 | 0.759 | 0.367 | 0.029 |
| 14 | 0.278 | 0.057 | 0.015 | 0.091 | 0.022 | 0.010 |
| 15 | 0.490 | 0.054 | 0.024 | 0.129 | 0.014 | 0.010 |
| 16 | 0.395 | 0.091 | 0.020 | 0.308 | 0.024 | 0.017 |
| 17 | 0.035 | 0.007 | 0.009 | 0.324 | 0.011 | 0.017 |
| 18 | 0.047 | 0.009 | 0.009 | 0.459 | 0.071 | 0.023 |
| 19 | 0.261 | 0.008 | 0.015 | 0.311 | 0.012 | 0.017 |
| 20 | 0.423 | 0.048 | 0.021 | 0.209 | 0.055 | 0.013 |
| 21 | 0.521 | 0.013 | 0.025 | 0.243 | 0.004 | 0.014 |
| 22 | 0.366 | 0.022 | 0.019 | 0.311 | 0.070 | 0.017 |
| 23 | 0.081 | 0.028 | 0.009 | 0.475 | 0.067 | 0.023 |
| 24 | 0.240 | 0.007 | 0.014 | 0.502 | 0.014 | 0.024 |
| 25 | 0.440 | 0.012 | 0.022 | 0.243 | 0.093 | 0.014 |
| 26 | 0.492 | 0.012 | 0.024 | 0.254 | 0.036 | 0.014 |

Average: $u_v = 0.018$ m/s

Maximum: $u_v = 0.043$ m/s

Minimum: $u_v = 0.009$ m/s

Table B.2 Velocity uncertainties – stiff nozzle, waveform B

| t (ms) | $V_{leading}$ (m/s) | StDev (m/s) | $u_v$ (m/s) | $V_{trailing}$ (m/s) | StDev (m/s) | $u_v$ (m/s) |
|---|---|---|---|---|---|---|
| 0 | 0 | 0 | 0 | | | |
| 1 | 0.399 | 0.009 | 0.020 | | | |
| 2 | 0.228 | 0.014 | 0.014 | | | |
| 3 | 0.205 | 0.019 | 0.013 | | | |
| 4 | 0.285 | 0.014 | 0.016 | | | |
| 5 | 0.328 | 0.019 | 0.017 | | | |
| 6 | 0.316 | 0.029 | 0.017 | | | |
| 7 | 0.276 | 0.022 | 0.015 | | | |
| 8 | 0.045 | 0.014 | 0.009 | | | |
| 9 | -0.041 | 0.030 | 0.009 | | | |
| 10 | -0.081 | 0.010 | 0.009 | 0.619 | 0.030 | 0.030 |
| 11 | -0.098 | 0.092 | 0.010 | 0.097 | 0.062 | 0.010 |
| 12 | 0.305 | 0.075 | 0.016 | -0.057 | 0.008 | 0.009 |
| 13 | 0.091 | 0.027 | 0.010 | -0.152 | 0.020 | 0.011 |
| 14 | 0.229 | 0.035 | 0.014 | 0.264 | 0.018 | 0.015 |
| 15 | -0.343 | 0.023 | 0.018 | 0.003 | 0.017 | 0.009 |
| 16 | 0.281 | 0.051 | 0.016 | -0.050 | 0.004 | 0.009 |
| 17 | 0.140 | 0.013 | 0.011 | -0.105 | 0.013 | 0.010 |
| 18 | -0.052 | 0.016 | 0.009 | 0.176 | 0.019 | 0.012 |
| 19 | -0.192 | 0.014 | 0.012 | -0.010 | 0.017 | 0.009 |
| 20 | 0.228 | 0.033 | 0.014 | 0.053 | 0.009 | 0.009 |
| 21 | 0.159 | 0.022 | 0.011 | -0.040 | 0.005 | 0.009 |
| 22 | 0.002 | 0.023 | 0.009 | 0.138 | 0.015 | 0.011 |
| 23 | 0.007 | 0.063 | 0.009 | 0.066 | 0.357 | 0.016 |
| 24 | 0.159 | 0.096 | 0.012 | 0.016 | 0.026 | 0.009 |
| 25 | 0.380 | 0.035 | 0.019 | 0.145 | 0.004 | 0.011 |
| 26 | | | | 0.148 | 0.011 | 0.011 |

Average: $u_v = 0.012$ m/s

Maximum: $u_v = 0.030$ m/s

Minimum: $u_v = 0.009$ m/s

Table B.3 Velocity uncertainties – flexible nozzle, waveform A

| t (ms) | $V_{leading}$ (m/s) | StDev (m/s) | $u_v$ (m/s) | $V_{trailing}$ (m/s) | StDev (m/s) | $u_v$ (m/s) |
|---|---|---|---|---|---|---|
| 0 | 0 | 0 | 0 | | | |
| 1 | 0.663 | 0.004 | 0.031 | | | |
| 2 | 0.942 | 0.007 | 0.044 | | | |
| 3 | 1.039 | 0.033 | 0.048 | | | |
| 4 | 0.198 | 0.088 | 0.013 | | | |
| 5 | 0.293 | 0.040 | 0.016 | | | |
| 6 | 0.243 | 0.062 | 0.014 | | | |
| 7 | 0.644 | 0.051 | 0.031 | -0.078 | 0.115 | 0.010 |
| 8 | 0.257 | 0.033 | 0.015 | 0.148 | 0.084 | 0.011 |
| 9 | 0.043 | 0.059 | 0.009 | 0.592 | 0.057 | 0.028 |
| 10 | 0.518 | 0.058 | 0.025 | 0.083 | 0.039 | 0.010 |
| 11 | 0.295 | 0.055 | 0.016 | 0.193 | 0.101 | 0.013 |
| 12 | 0.186 | 0.090 | 0.012 | 0.487 | 0.117 | 0.024 |
| 13 | 0.326 | 0.150 | 0.018 | 0.229 | 0.109 | 0.014 |
| 14 | 0.349 | 0.029 | 0.018 | 0.200 | 0.086 | 0.013 |
| 15 | 0.399 | 0.097 | 0.020 | 0.252 | 0.059 | 0.014 |
| 16 | 0.454 | 0.042 | 0.022 | 0.407 | 0.075 | 0.021 |
| 17 | 0.651 | 0.158 | 0.031 | 0.214 | 0.028 | 0.013 |
| 18 | 0.371 | 0.070 | 0.019 | 0.262 | 0.028 | 0.015 |
| 19 | 0.380 | 0.257 | 0.020 | 0.818 | 0.150 | 0.038 |
| 20 | 0.483 | 0.083 | 0.024 | 0.178 | 0.201 | 0.013 |
| 21 | 0.590 | 0.111 | 0.028 | 0.468 | 0.066 | 0.023 |
| 22 | 0.299 | 0.092 | 0.016 | 0.547 | 0.171 | 0.027 |
| 23 | 0.867 | 0.165 | 0.041 | 0.548 | 0.080 | 0.026 |

Average: $u_v = 0.021$ m/s

Maximum: $u_v = 0.048$ m/s

Minimum: $u_v = 0.009$ m/s

Table B.4 Velocity uncertainties – flexible nozzle, waveform B

| t (ms) | $V_{leading}$ (m/s) | StDev (m/s) | $u_v$ (m/s) | $V_{trailing}$ (m/s) | StDev (m/s) | $u_v$ (m/s) |
|---|---|---|---|---|---|---|
| 0 | 0 | 0 | 0 | | | |
| 1 | 0.668 | 0.010 | 0.032 | | | |
| 2 | 0.935 | 0.012 | 0.044 | | | |
| 3 | 1.051 | 0.027 | 0.049 | | | |
| 4 | 0.823 | 0.041 | 0.039 | | | |
| 5 | 0.435 | 0.043 | 0.022 | | | |
| 6 | 0.402 | 0.013 | 0.020 | 1.025 | 0.504 | 0.048 |
| 7 | 0.404 | 0.038 | 0.020 | 0.710 | 0.013 | 0.034 |
| 8 | 0.878 | 0.086 | 0.041 | 0.281 | 0.119 | 0.016 |
| 9 | 0.645 | 0.070 | 0.031 | 0.299 | 0.061 | 0.016 |
| 10 | 0.507 | 0.025 | 0.025 | 0.633 | 0.043 | 0.030 |
| 11 | 0.573 | 0.052 | 0.028 | 0.595 | 0.055 | 0.029 |
| 12 | 0.830 | 0.195 | 0.039 | 0.720 | 0.092 | 0.034 |
| 13 | 0.573 | 0.033 | 0.028 | 0.388 | 0.017 | 0.020 |
| 14 | 0.664 | 0.006 | 0.032 | 0.164 | 0.052 | 0.012 |
| 15 | 0.464 | 0.068 | 0.023 | 0.661 | 0.119 | 0.031 |
| 16 | 0.692 | 0.070 | 0.033 | 0.311 | 0.238 | 0.017 |
| 17 | 0.896 | 0.125 | 0.042 | 0.557 | 0.185 | 0.027 |
| 18 | 0.915 | 0.144 | 0.043 | 0.447 | 0.093 | 0.022 |
| 19 | 0.545 | 0.198 | 0.026 | 0.619 | 0.076 | 0.030 |
| 20 | 0.604 | 0.045 | 0.029 | 0.438 | 0.054 | 0.022 |
| 21 | 0.659 | 0.042 | 0.031 | 0.844 | 0.366 | 0.040 |
| 22 | 0.668 | 0.075 | 0.032 | 0.443 | 0.045 | 0.022 |
| 23 | 0.447 | 0.021 | 0.022 | 0.649 | 0.031 | 0.031 |
| 24 | 0.490 | 0.020 | 0.024 | 0.592 | 0.180 | 0.028 |
| 25 | 0.640 | 0.011 | 0.030 | 0.428 | 0.018 | 0.021 |
| 26 | 0.814 | 0.104 | 0.038 | 0.452 | 0.021 | 0.022 |

Average: $u_v = 0.029$ m/s

Maximum: $u_v = 0.049$ m/s

Minimum: $u_v = 0.012$ m/s

## *B.3 Droplet Position Uncertainty*

The process of determining the position of the leading edge involved simply involved converting a distance in pixels to a distance in millimeters. The equation to do this is

$$d = C_f P2 \tag{B11}$$

Therefore the uncertainty is

$$u_d = \sqrt{\left(\frac{\partial d}{\partial C_f} u_{C_f}\right)^2 + \left(\frac{\partial d}{\partial P2} u_{P2}\right)^2} \tag{B12}$$

where

$$\frac{\partial d}{\partial C_f} = P2 \tag{B13}$$

and

$$\frac{\partial d}{\partial P2} = C_f \tag{B14}$$

The uncertainty and standard deviation values for both nozzle cases and both waveforms appear in the following tables.

Table B.5 Position uncertainties – stiff nozzle, waveform A

| t (ms) | d (mm) | StDev (mm) | $u_d$ (mm) |
|---|---|---|---|
| 0 | 0 | 0 | 0 |
| 1 | 0.33 | 0.00 | 0.02 |
| 2 | 0.61 | 0.01 | 0.03 |
| 3 | 0.89 | 0.01 | 0.04 |
| 4 | 1.31 | 0.04 | 0.06 |
| 5 | 1.86 | 0.05 | 0.08 |
| 6 | 2.44 | 0.08 | 0.11 |
| 7 | 2.84 | 0.15 | 0.13 |
| 8 | 3.25 | 0.12 | 0.15 |
| 9 | 3.53 | 0.15 | 0.16 |
| 10 | 3.68 | 0.13 | 0.17 |
| 11 | 3.78 | 0.16 | 0.17 |
| 12 | 3.85 | 0.19 | 0.18 |
| 13 | 3.99 | 0.21 | 0.18 |
| 14 | 4.27 | 0.19 | 0.19 |
| 15 | 4.97 | 0.01 | 0.23 |
| 16 | 5.30 | 0.10 | 0.24 |
| 17 | 5.33 | 0.09 | 0.24 |
| 18 | 5.28 | 0.10 | 0.24 |
| 19 | 5.55 | 0.08 | 0.25 |
| 20 | 5.97 | 0.11 | 0.27 |
| 21 | 6.60 | 0.04 | 0.30 |
| 22 | 7.26 | 0.06 | 0.33 |
| 23 | 7.04 | 0.25 | 0.32 |
| 24 | 7.33 | 0.13 | 0.33 |
| 25 | 7.65 | 0.25 | 0.35 |
| 26 | 8.07 | 0.01 | 0.37 |

Average: $u_d = 0.20$ mm

Maximum: $u_d = 0.37$ mm

Minimum: $u_d = 0.02$ mm

Table B.6 Position uncertainties – stiff nozzle, waveform B

| t (ms) | d (mm) | StDev (mm) | $u_d$ (mm) |
|---|---|---|---|
| 0 | 0 | 0 | 0 |
| 1 | 0.37 | 0.01 | 0.02 |
| 2 | 0.62 | 0.01 | 0.03 |
| 3 | 0.82 | 0.00 | 0.04 |
| 4 | 1.12 | 0.01 | 0.05 |
| 5 | 1.46 | 0.01 | 0.07 |
| 6 | 1.78 | 0.01 | 0.08 |
| 7 | 2.03 | 0.04 | 0.09 |
| 8 | 2.25 | 0.05 | 0.10 |
| 9 | 2.29 | 0.03 | 0.10 |
| 10 | 2.30 | 0.02 | 0.10 |
| 11 | 2.29 | 0.17 | 0.10 |
| 12 | 2.21 | 0.09 | 0.10 |
| 13 | 2.34 | 0.07 | 0.11 |
| 14 | 2.25 | 0.08 | 0.10 |
| 15 | 1.59 | 0.08 | 0.07 |
| 16 | 1.85 | 0.10 | 0.08 |
| 17 | 1.86 | 0.03 | 0.08 |
| 18 | 1.69 | 0.14 | 0.08 |
| 19 | 1.51 | 0.09 | 0.07 |
| 20 | 2.24 | 0.12 | 0.10 |
| 21 | 2.13 | 0.12 | 0.10 |
| 22 | 2.37 | 0.21 | 0.11 |
| 23 | 2.71 | 0.14 | 0.12 |
| 24 | 3.34 | 0.20 | 0.15 |
| 25 | 3.53 | 0.20 | 0.16 |

Average: $u_d = 0.09$ mm

Maximum: $u_d = 0.16$ mm

Minimum: $u_d = 0.02$ mm

Table B.7 Position uncertainties – flexible nozzle, waveform A

| t (ms) | d (mm) | StDev (mm) | $u_d$ (mm) |
|---|---|---|---|
| 0 | 0 | 0 | 0 |
| 1 | 0.92 | 0.00 | 0.04 |
| 2 | 1.91 | 0.00 | 0.09 |
| 3 | 3.00 | 0.01 | 0.14 |
| 4 | 3.22 | 0.03 | 0.15 |
| 5 | 3.56 | 0.04 | 0.16 |
| 6 | 3.85 | 0.02 | 0.18 |
| 7 | 4.40 | 0.05 | 0.20 |
| 8 | 4.69 | 0.05 | 0.21 |
| 9 | 4.32 | 0.04 | 0.20 |
| 10 | 5.00 | 0.11 | 0.23 |
| 11 | 5.33 | 0.04 | 0.24 |
| 12 | 5.44 | 0.09 | 0.25 |
| 13 | 5.74 | 0.13 | 0.26 |
| 14 | 6.12 | 0.21 | 0.28 |
| 15 | 6.68 | 0.16 | 0.30 |
| 16 | 6.89 | 0.05 | 0.31 |
| 17 | 7.22 | 0.08 | 0.33 |
| 18 | 7.62 | 0.08 | 0.35 |
| 19 | 7.89 | 0.04 | 0.36 |
| 20 | 8.36 | 0.09 | 0.38 |
| 21 | 9.04 | 0.04 | 0.41 |
| 22 | 9.55 | 0.01 | 0.44 |
| 23 | 10.32 | 0.03 | 0.47 |

Average: $u_d = 0.26$ mm

Maximum: $u_d = 0.47$ mm

Minimum: $u_d = 0.04$ mm

Table B.8 Position uncertainties – flexible nozzle, waveform B

| t (ms) | d (mm) | StDev (mm) | $u_d$ (mm) |
|---|---|---|---|
| 0 | 0 | 0 | 0 |
| 1 | 0.92 | 0.00 | 0.04 |
| 2 | 1.75 | 0.01 | 0.08 |
| 3 | 2.80 | 0.01 | 0.13 |
| 4 | 3.60 | 0.02 | 0.16 |
| 5 | 3.88 | 0.08 | 0.18 |
| 6 | 4.04 | 0.04 | 0.18 |
| 7 | 4.44 | 0.04 | 0.20 |
| 8 | 5.05 | 0.03 | 0.23 |
| 9 | 5.82 | 0.11 | 0.27 |
| 10 | 6.07 | 0.07 | 0.28 |
| 11 | 6.45 | 0.09 | 0.29 |
| 12 | 6.94 | 0.14 | 0.32 |
| 13 | 7.59 | 0.27 | 0.35 |
| 14 | 8.40 | 0.04 | 0.38 |
| 15 | 8.66 | 0.32 | 0.39 |
| 16 | 8.88 | 0.18 | 0.40 |
| 17 | 9.35 | 0.16 | 0.43 |
| 18 | 9.98 | 0.08 | 0.46 |
| 19 | 10.41 | 0.16 | 0.47 |
| 20 | 10.53 | 0.08 | 0.48 |
| 21 | 10.72 | 0.29 | 0.49 |
| 22 | 11.27 | 0.48 | 0.51 |
| 23 | 11.31 | 0.10 | 0.52 |
| 24 | 11.63 | 0.14 | 0.53 |
| 25 | 12.12 | 0.07 | 0.55 |
| 26 | 12.87 | 0.13 | 0.59 |

Average: $u_d = 0.34$ mm

Maximum: $u_d = 0.59$ mm

Minimum: $u_d = 0.04$ mm

## *B.4 Spread Rate Uncertainty*

Calculating the velocity of the edge of a spreading droplet is the same process outlined in section B.2. It is identical to calculating the velocity of the leading or trailing edge of the droplet during the formation process. Therefore, the derivation does not need to be repeated here. Only the results will be given. It should be noted that because the timing of each impinging drop was different, the trials could not be considered repeatable. Therefore, no standard deviation data is provided.

Table B.9 Spread rate uncertainties – stiff nozzle

| U (m/s) | $u_U$ (m/s) | U (m/s) | $u_U$ (m/s) |
|---|---|---|---|
| -0.275 | 0.015 | 0.080 | 0.009 |
| -0.249 | 0.014 | 0.089 | 0.010 |
| -0.160 | 0.011 | 0.115 | 0.010 |
| -0.098 | 0.011 | 0.151 | 0.011 |
| -0.093 | 0.011 | 0.204 | 0.013 |
| -0.084 | 0.010 | 0.231 | 0.013 |
| -0.080 | 0.011 | 0.257 | 0.014 |
| -0.058 | 0.010 | 0.297 | 0.016 |
| -0.040 | 0.009 | 0.302 | 0.016 |
| -0.040 | 0.009 | 0.337 | 0.017 |
| -0.022 | 0.009 | 0.342 | 0.017 |
| -0.018 | 0.009 | 0.391 | 0.019 |
| -0.009 | 0.009 | 0.404 | 0.020 |
| -0.009 | 0.009 | 0.408 | 0.020 |
| -0.009 | 0.009 | 0.484 | 0.023 |
| -0.004 | 0.009 | 0.493 | 0.023 |
| -0.004 | 0.009 | 0.550 | 0.026 |
| 0.000 | 0.009 | 0.666 | 0.031 |
| 0.000 | 0.009 | 0.670 | 0.031 |
| 0.004 | 0.009 | 0.675 | 0.031 |
| 0.004 | 0.009 | 0.768 | 0.035 |
| 0.004 | 0.009 | 0.799 | 0.036 |
| 0.013 | 0.009 | 0.892 | 0.040 |
| 0.031 | 0.009 | 1.030 | 0.046 |
| 0.049 | 0.009 | 1.043 | 0.047 |
| 0.071 | 0.009 | 1.118 | 0.050 |
| 0.075 | 0.009 | 1.291 | 0.058 |

Average: $u_U = 0.010$ m/s

Maximum: $u_U = 0.015$ m/s

Minimum: $u_U = 0.009$ m/s

Table B.10 Spread rate uncertainties – flexible nozzle

| U (m/s) | $u_U$ (m/s) | U (m/s) | $u_U$ (m/s) |
|---|---|---|---|
| -0.067 | 0.009 | 0.115 | 0.010 |
| -0.053 | 0.009 | 0.129 | 0.010 |
| -0.053 | 0.009 | 0.129 | 0.010 |
| -0.049 | 0.009 | 0.146 | 0.011 |
| -0.044 | 0.009 | 0.151 | 0.011 |
| -0.044 | 0.009 | 0.200 | 0.012 |
| -0.040 | 0.009 | 0.217 | 0.013 |
| -0.040 | 0.009 | 0.217 | 0.013 |
| -0.040 | 0.009 | 0.240 | 0.014 |
| -0.022 | 0.009 | 0.257 | 0.014 |
| -0.022 | 0.009 | 0.266 | 0.015 |
| -0.013 | 0.009 | 0.275 | 0.015 |
| 0.000 | 0.009 | 0.297 | 0.016 |
| 0.000 | 0.009 | 0.337 | 0.017 |
| 0.000 | 0.009 | 0.444 | 0.021 |
| 0.000 | 0.009 | 0.448 | 0.022 |
| 0.009 | 0.009 | 0.541 | 0.026 |
| 0.062 | 0.009 | 0.626 | 0.029 |
| 0.084 | 0.009 | 1.087 | 0.049 |
| 0.093 | 0.010 | 1.092 | 0.049 |
| 0.098 | 0.010 | 1.114 | 0.050 |
| 0.102 | 0.010 | | |

Average: $u_U = 0.015$ m/s

Maximum: $u_U = 0.050$ m/s

Minimum: $u_U = 0.009$ m/s

## *B.5 Contact Angle Uncertainty*

Calculating the contact angle did not require knowledge of the time interval between frames or the experimental coefficients. A line was drawn along the liquid surface in contact with the solid glass plate, and two points from this line were used to determine the contact angle using the following equation.

$$\theta_c = 90 + \tan^{-1}\left(\frac{\Delta x}{\Delta y}\right) \tag{B15}$$

The uncertainty is

$$u_{\theta_c} = \sqrt{\left(\frac{\partial \theta_c}{\partial \Delta x} u_{\Delta x}\right)^2 + \left(\frac{\partial \theta_c}{\partial \Delta y} u_{\Delta y}\right)^2} \tag{B16}$$

where

$$\frac{\partial \theta_c}{\partial \Delta x} = \frac{1}{\left(1 + \Delta x^2\right)\Delta y} \tag{B17}$$

and

$$\frac{\partial \theta_c}{\partial \Delta y} = -\frac{\Delta x}{\left(1 + \Delta y^2\right)\Delta y^2} \tag{B18}$$

$u_{\Delta x}$ and $u_{\Delta y}$ were determined to be 2 pixels. This is greater than the previous error values because there is some uncertainty introduced when the line along the liquid surface is constructed. This human error cannot be specifically calculated, so it should be noted that the following uncertainty values listed in the following tables are likely underestimations of the actual error present. Again, as the timing among droplets was not repeatable, no standard deviation data is given.

Table B.11 Contact angle uncertainties – stiff nozzle

| $\theta_c$ (degrees) | $u_\theta$ (degrees) |
|---|---|
| 31.218 | 0.003 |
| 32.179 | 0.001 |
| 38.027 | 0.001 |
| 38.351 | 0.000 |
| 50.268 | 0.000 |
| 52.507 | 0.001 |
| 56.802 | 0.001 |
| 64.398 | 0.001 |
| 68.484 | 0.001 |
| 68.532 | 0.001 |
| 70.484 | 0.002 |
| 73.610 | 0.001 |
| 78.811 | 0.004 |
| 81.347 | 0.006 |
| 82.539 | 0.011 |
| 83.723 | 0.009 |
| 83.863 | 0.012 |
| 84.644 | 0.015 |
| 85.872 | 0.024 |
| 86.055 | 0.036 |
| 87.510 | 0.073 |
| 93.289 | 0.051 |
| 94.574 | 0.018 |
| 115.201 | 0.001 |
| 118.217 | 0.001 |
| 123.232 | 0.000 |

Average: $u_\theta = 0.010$ degrees

Maximum: $u_\theta = 0.073$ degrees

Minimum: $u_\theta = 0.000$ degrees

Table B.12 Contact angle uncertainties – flexible nozzle

| $\theta_c$ (degrees) | $u_\theta$ (degrees) | $\theta_c$ (degrees) | $u_\theta$ (degrees) |
|---|---|---|---|
| 21.801 | 0.013 | 103.349 | 0.010 |
| 27.929 | 0.003 | 105.396 | 0.005 |
| 30.500 | 0.002 | 107.241 | 0.006 |
| 33.179 | 0.001 | 108.435 | 0.004 |
| 36.444 | 0.002 | 109.058 | 0.006 |
| 37.461 | 0.001 | 109.290 | 0.004 |
| 38.928 | 0.002 | 109.537 | 0.004 |
| 42.474 | 0.001 | 110.266 | 0.003 |
| 44.045 | 0.001 | 111.297 | 0.004 |
| 44.465 | 0.001 | 112.329 | 0.004 |
| 47.010 | 0.001 | 113.875 | 0.003 |
| 48.991 | 0.001 | 114.102 | 0.001 |
| 49.145 | 0.000 | 115.641 | 0.004 |
| 49.485 | 0.001 | 119.954 | 0.002 |
| 55.146 | 0.001 | 124.992 | 0.002 |
| 57.907 | 0.001 | 125.870 | 0.001 |
| 58.610 | 0.002 | 128.157 | 0.003 |
| 59.744 | 0.002 | 130.696 | 0.001 |
| 77.255 | 0.004 | 132.089 | 0.006 |
| 83.333 | 0.018 | 133.069 | 0.002 |
| 85.914 | 0.063 | | |

Average: $u_\theta = 0.005$ degrees

Maximum: $u_\theta = 0.063$ degrees

Minimum: $u_\theta = 0.000$ degrees

# APPENDIX C

## Droplet Formation Images

This appendix provides a series of sequential images 0.5 ms apart that show the drop formation process from the instant a drop begins to emerge from the nozzle, until the drop moves out of the camera frame. Sequences for both nozzle cases and both waveforms are provided. The sequences are presented in the order they are discussed in the main body of this document. First the stiff nozzle cases are presented, then the flexible nozzle cases. The waveform A sequences always precede waveform B sequences.

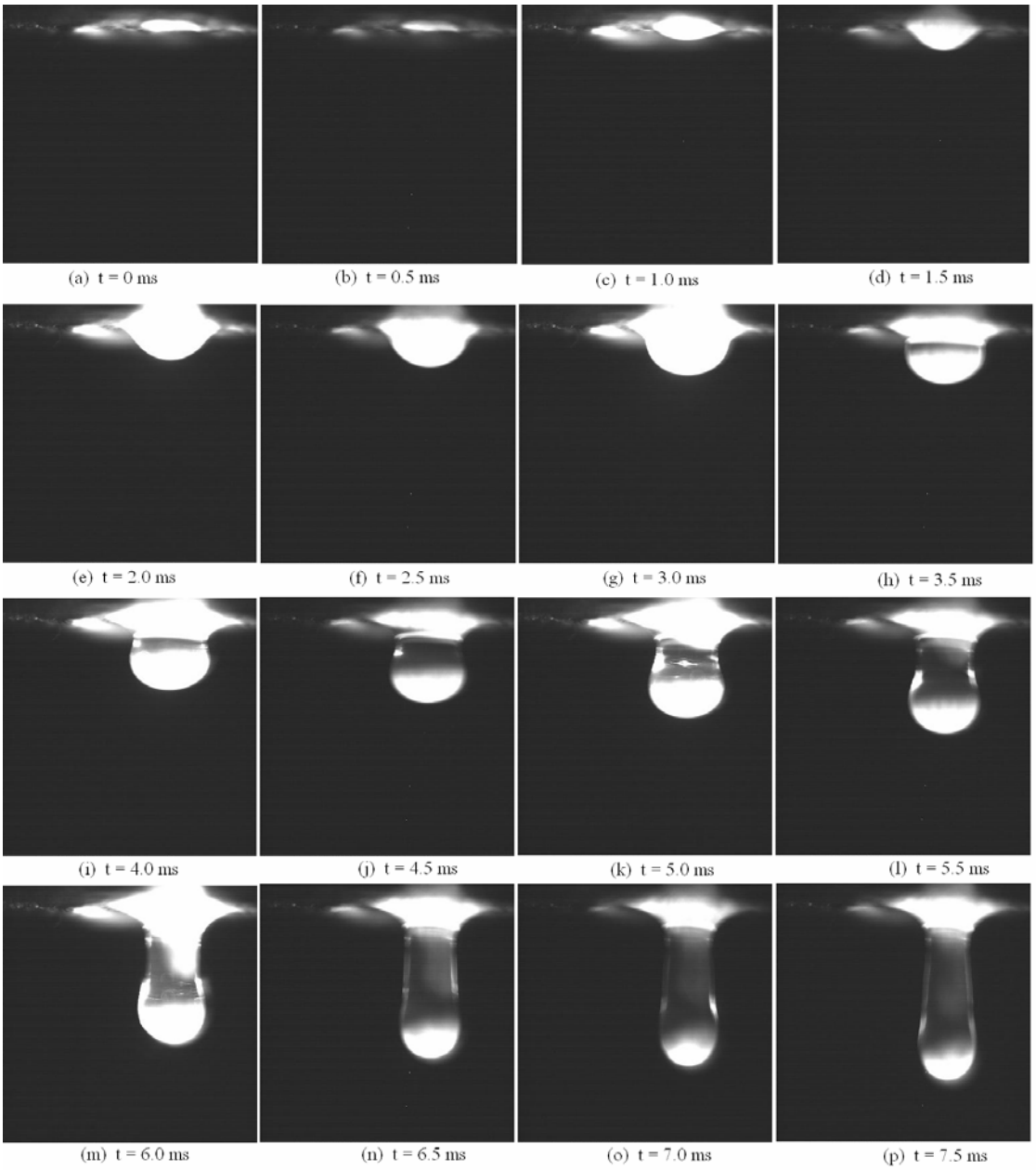


Figure C.1
Droplet formation for the stiff nozzle, waveform A (0 - 7.5 ms)

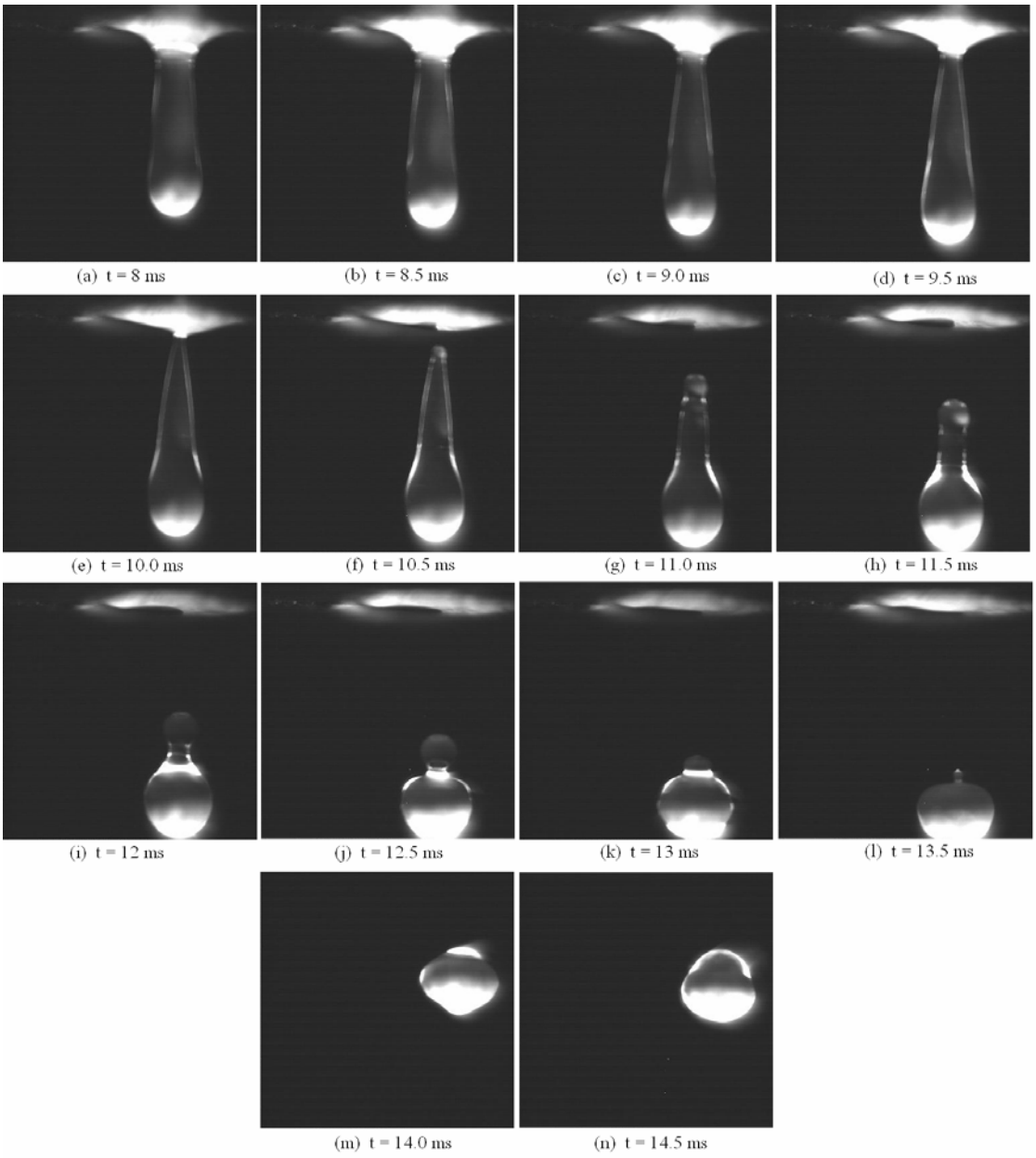


Figure C.2
Droplet formation for the stiff nozzle, waveform A (8 - 14.5 ms)
Break-off occurs in panel (f). The camera has been shifted down from the nozzle in panels (m) and (n) to track the leading edge.

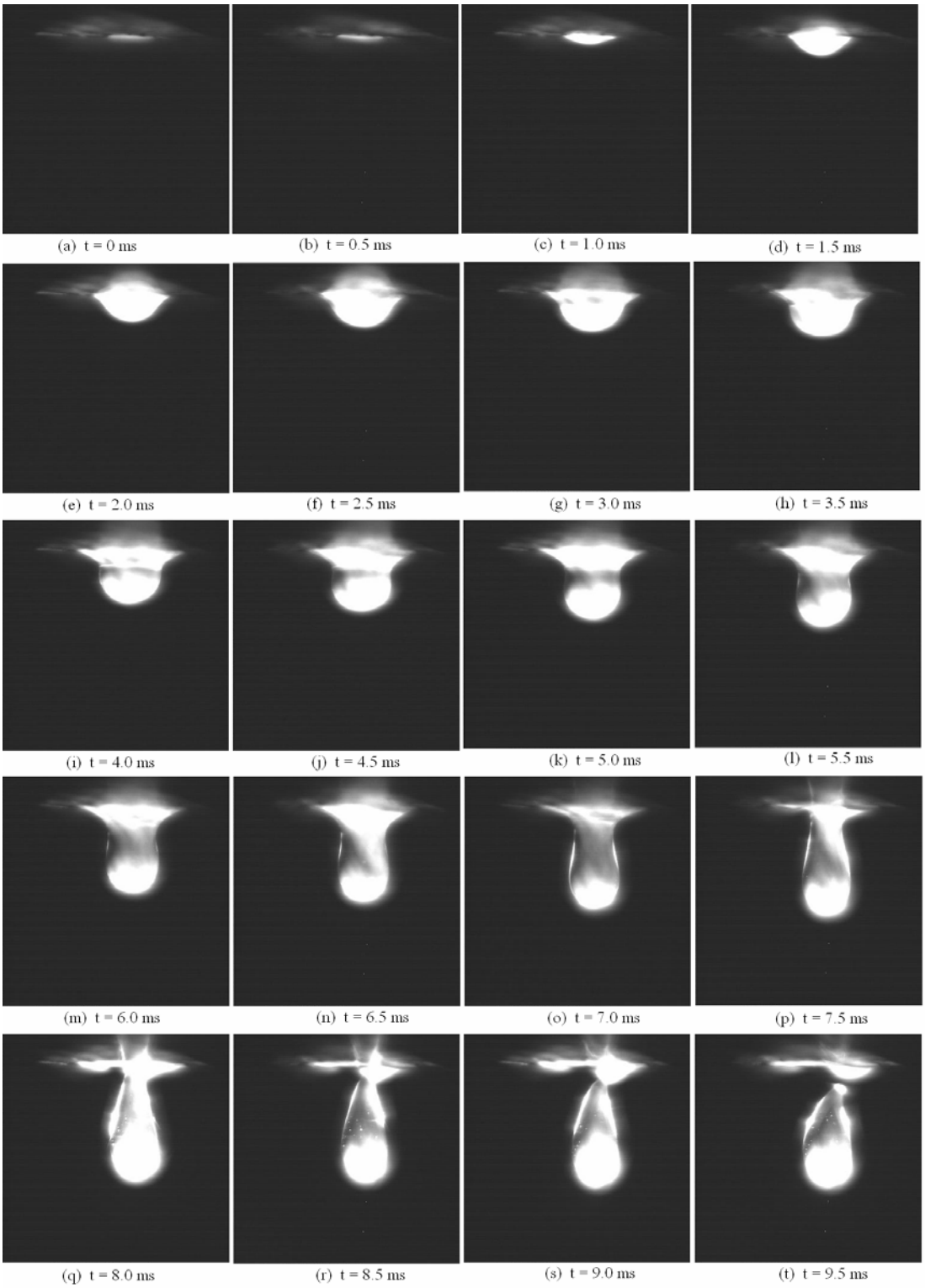


Figure C.3
Droplet formation for the stiff nozzle, waveform B (0 – 9.5 ms)
Break-off occurs in panel (t).

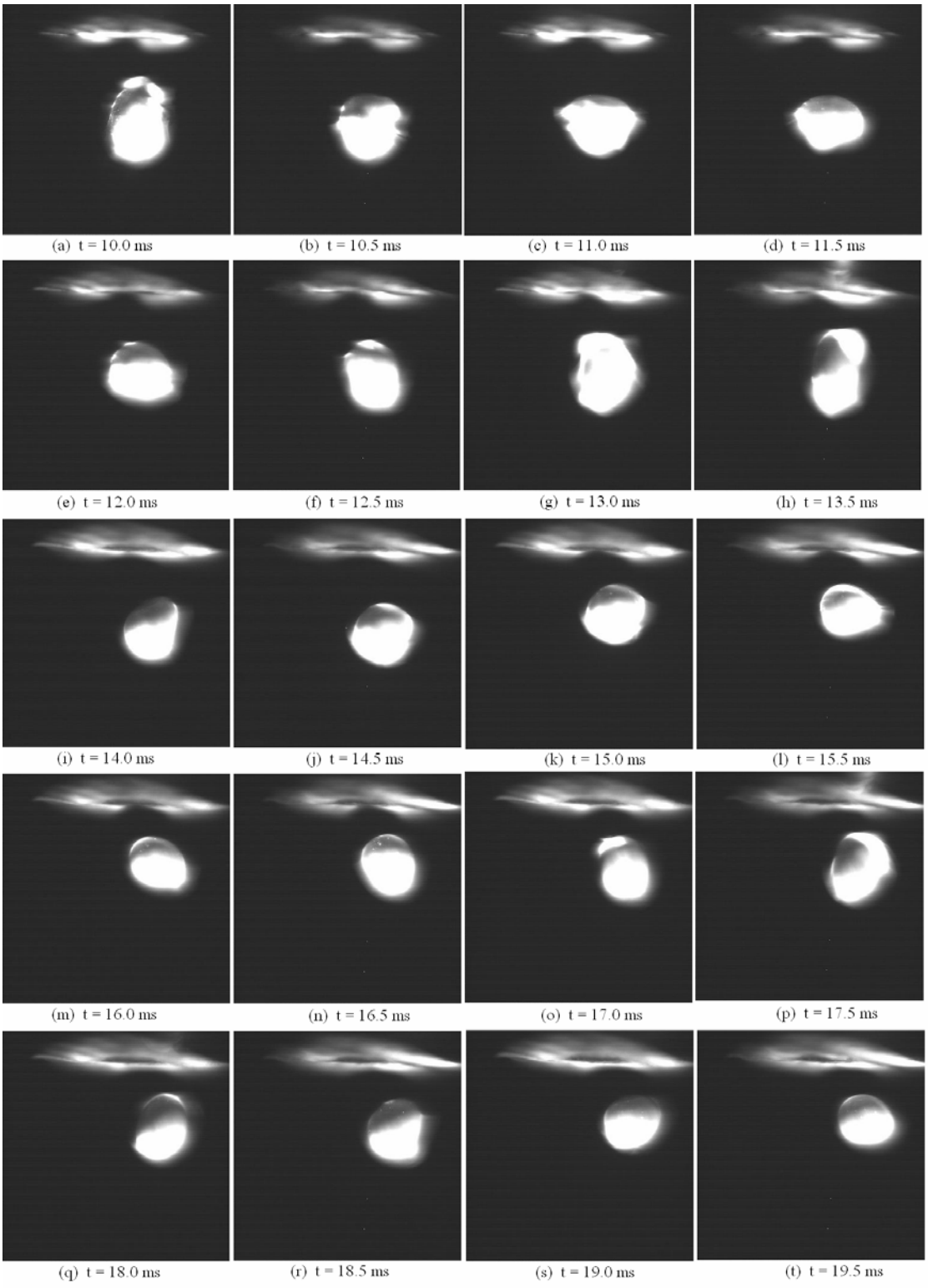


Figure C.4
Droplet formation for the stiff nozzle, waveform B (10 – 19.5 ms)

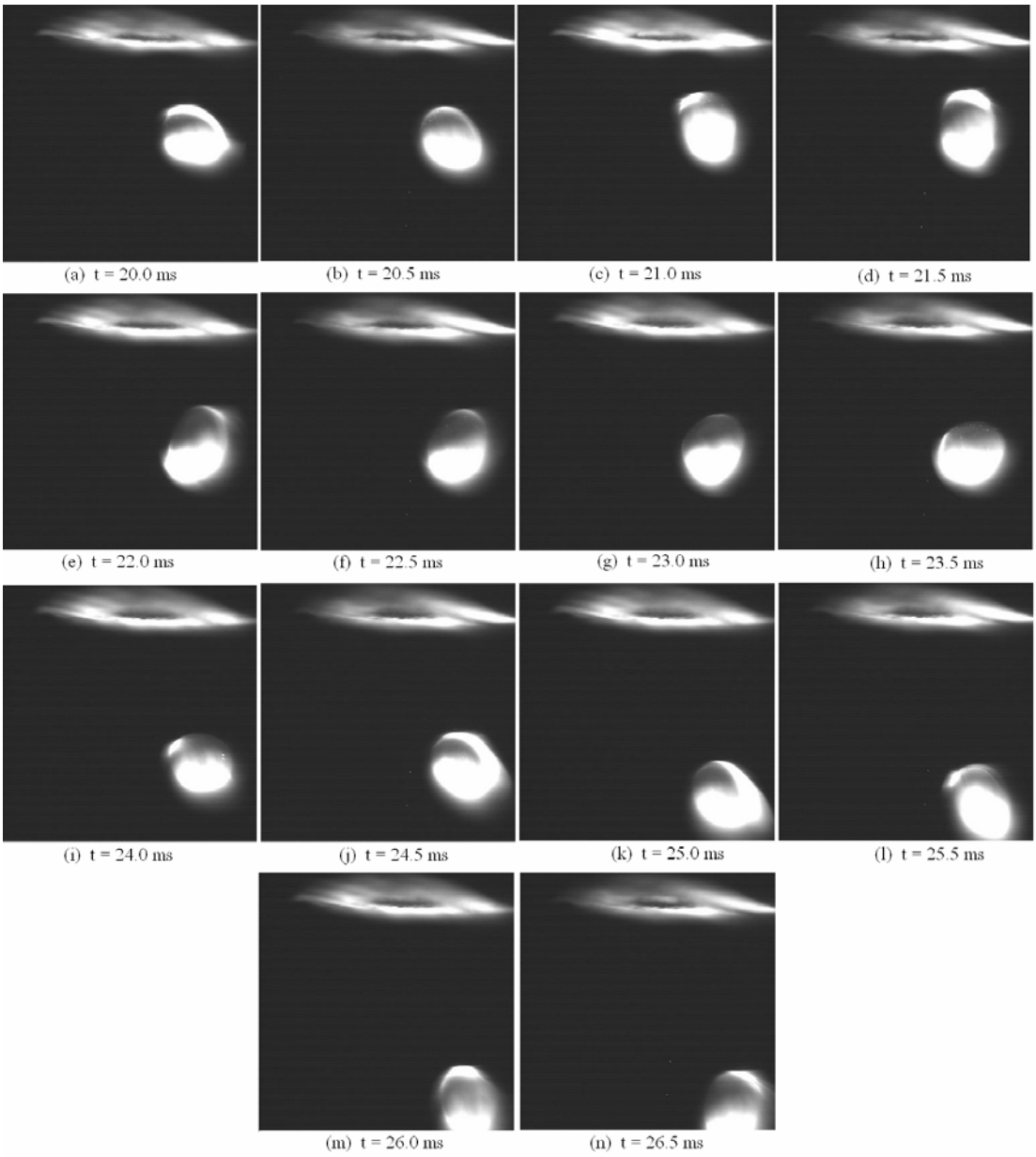


Figure C.5
Droplet formation for the stiff nozzle, waveform B (20 – 26.5 ms)

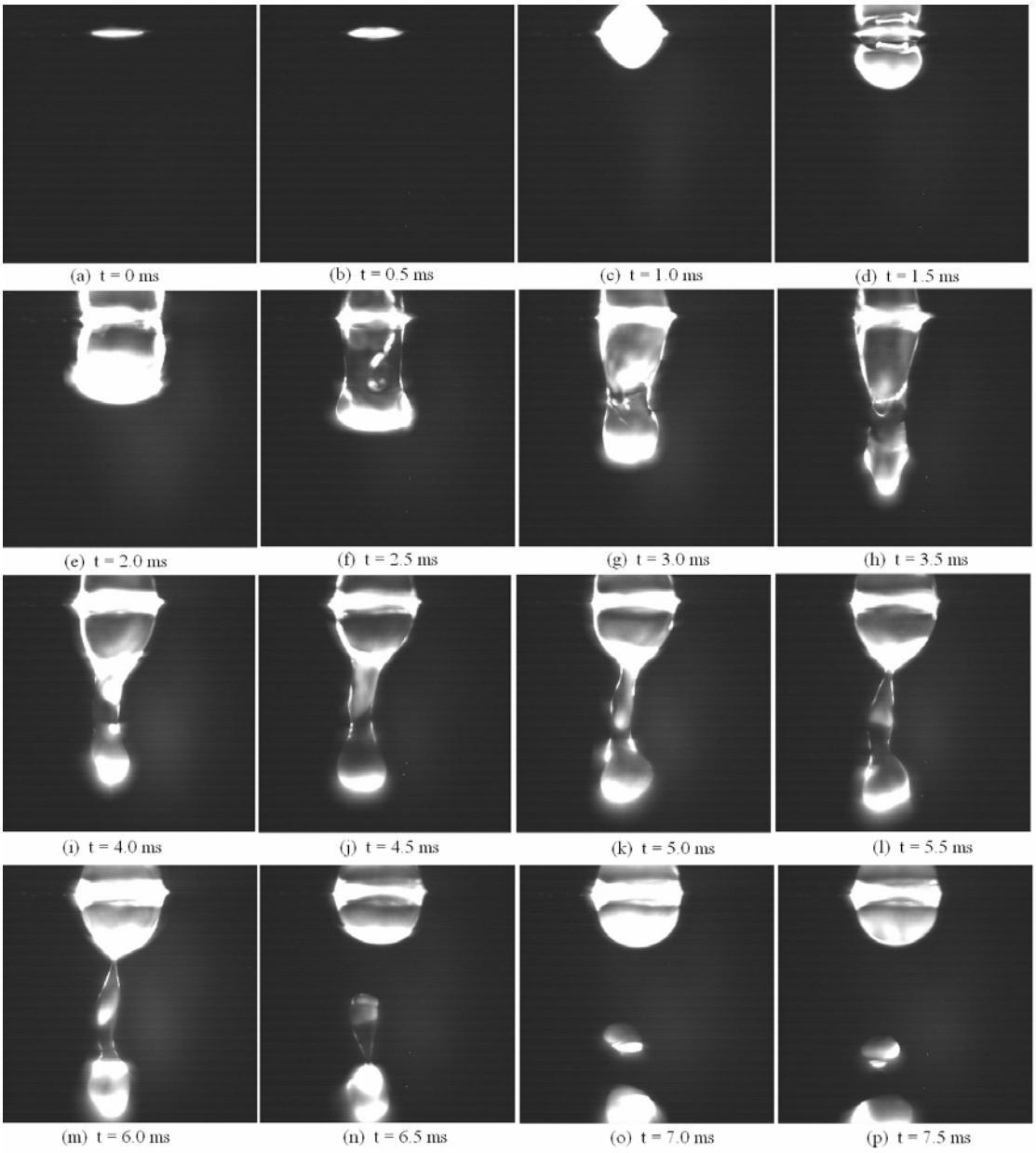


Figure C.6
Droplet formation for the flexible nozzle, waveform A (0 – 7.5 ms)
Break-off occurs in panel (n)

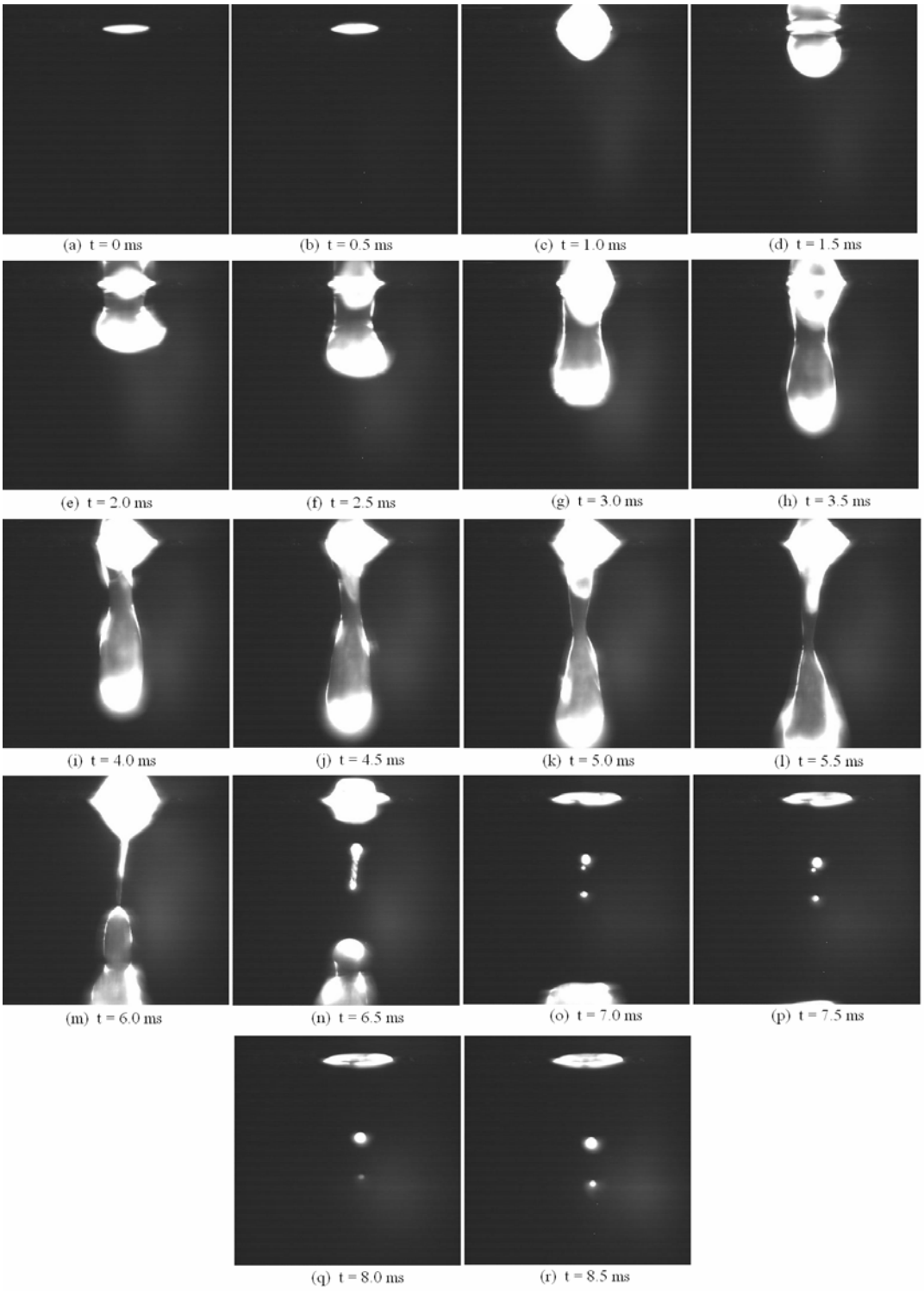


Figure C.7
Droplet formation for the flexible nozzle, waveform B (0 – 8.5 ms)
Break-off occurs in panel (n). However, under these conditions the very beginning of break-off often occurred in panel (m).